Title

Platinum group metal oxides for heterogeneous catalysis: Novel synthesis and advanced characterization

Author
Misch, Lauren

Publication Date
2014

Peer reviewed|Thesis/dissertation

UNIVERSITY of CALIFORNIA

Santa Barbara

Platinum group metal oxides for heterogeneous catalysis: Novel synthesis and advanced characterization

A Dissertation submitted in partial satisfaction of the

requirements for the degree

Doctor of Philosophy

in

Chemistry

by

Lauren M. Misch

Committee in charge:

Professor Galen D. Stucky, Chair
Professor Ram Seshadri
Professor Eric W. McFarland
Professor Horia Metiu
Professor Steven K. Buratto

June 2014

The dissertation of Lauren M. Misch is approved.

Professor Ram Seshadri

Professor Eric W. McFarland

Professor Horia Metiu

Professor Steven K. Buratto

Professor Galen D. Stucky, Committee Chair

December 2013

Platinum group metal oxides for heterogeneous catalysis: Novel synthesis and advanced characterization

by

Lauren M. Misch

for my family

Acknowledgements

The work presented here would not have been possible without the guidance, assistance, and encouragement of my advisors, colleagues, family, and friends. I am extremely grateful to those who contributed directly to the research, including Drs. Josh Kurzman, Alex Birkel, Brett Fors, Jakoah Brgoch, Tom Mates, and Alan Derk, Bathylle Héry, and Ina Sørensen. Their involvement in the work presented here is very much appreciated. I thank the NSF ConvEne IGERT program for fellowship support and the Department of Energy for funding this work.

I thank my advisors Professors Galen Stucky and Ram Seshadri. Galen's enthusiasm and zest for life is infectious and I'm lucky to have been encouraged to pursue my passions. It is without exaggeration to say that I am exceptionally lucky to have had the guidance and advocacy of Ram Seshadri. Ram is devoted to his students' research and development and scientists. He provides us with fantastic cultural experiences, and his humorous nature keeps the rigors of graduate school light-hearted and joyful. His generosity and kindness cannot be overemphasized. He is truly an artist in everything from the beautiful ways he represents scientific data to his own personal style. Ram's personality is reflected in the extraordinary group of people he has brought together in his research group.

It has been a tremendous pleasure to be part of the Seshadri group. In this group I have made some lifelong friends. Not only have I been surrounded by exceptional scientists, but I have been able to interact with some of the most hilarious, creative, and altruistic humans I could have ever asked for. I thank Dr. Josh Kurzman for being an fantastic mentor and friend. Josh's patience and kindness while teaching me the basics of being a scientist will never be forgotten. Along with being a major influence on my research, Josh continues to be a generous and dependable friend. I hope we'll continue to connect from wherever our lives take us. I thank Drs. Alex and Christina Birkel for helping me produce great work and letting me be part of their family.

My office mates Moureen and Jason have been some of the most supportive and entertaining colleagues and friends I've ever had. I'm so lucky to have spent some time in their company. Moureen's optimism and and gentleness make her truly a delight to be around. Jason's humor and decency are unparalleled. I will look back on our time together in that office with such fondness. I thank Jakoah, Nate, Phil, Kristin, Kim, Mike, Jaye, Megan, and Leo for being great colleagues and friends. All the members of the Seshadri group have had a significant impact on my career at UCSB. Because of my involvement in the Seshadri group, I have had the privilege of mentoring international students. I am so very grateful for this opportunity, and specifically for my friendship with Bathylle Héry.

I thank my committee members Professors Horia Metiu, Eric McFarland, and Steve Buratto. Horia helped me find my place in Galen's group and working with Eric. He has always encouraged and praised me when I really needed it. Horia's reassurance gave me the confidence to be keep moving forward. Together, Eric and Horia taught me to be both meticulous and open-minded. Their enthusiasm for their research and passion for discovery made me ambitious. My experience with Eric and Horia's research group was often challenging and demanding; it made me a better scientist and for this I am grateful. I also thank Steve for recognizing my potential in the classroom and encouraging me achieve.

I thank the Materials Research lab staff, especially Sara Bard, Sylvia Vogel, Maureen Evans, Janet Shalhoob, Joe Doyle, and Amanda Strom. All the MRL staff members have contributed to a truly delightful and functional work environment. I thank my undergraduate advisors Professors Bogdan Dragnea and David Clemmer for giving me the confidence to apply to graduate school, and the encouragement to be free and open to new possibilities.

I thank Alan Derk for being a brilliant colleague and a devoted friend. Conversations with Alan have enhanced my understanding of scientific phenomena, human emotion, and a multitude of other topics. Interaction with Alan has made my life full and vibrant. I am grateful for our numerous adventures, past, present, and those to come. I thank Gesine and Bethany for being sweet and supportive roommates. The stress and and frustration of a graduate program can really only be understood by those in similar situations. Thanks for being my sisters. I thank Dr. Matt Santana for unfailing support and encouragement. I thank the yogis of Santa Barbara for teaching me mindfulness and meditation. I thank Linus for the grudging affection.

Most importantly I thank my Mom, Dad, and sister Kelly. Your constant support and love has brought me so far. Thank you for giving me so much affection and instilling in me confidence. Thank you for always encouraging me to pursue my dreams. Thank you for giving me courage and strength. Thank you for life and celebrating it with me.

Curriculum Vitæ

Lauren M. Misch

Education

2009-2013	Ph.D Chemistry, Department of Chemistry and Biochemistry, University of California, Santa Barbara.
2005-2009	B.S. Chemistry, Indiana University, Bloomington, IN

Publications

5. L. M. Misch, J. Brgoch, A. Birkel, T. Mates, G. D. Stucky, and R. Seshadri La_2BaPdO_5 and La_2BaPtO_5: Rapid microwave preparation and stability studies, *Inorg. Chem.* **53** (2014) 2628-2634.

4. L. M. Misch, A. Birkel, C. A. Figg, B. P. Fors, G. D. Stucky, C. J. Hawker, and R. Seshadri, Rapid microwave-assisted sol-gel preparation of Pd-substituted LnFeO$_3$ (Ln = Y, La): Phase formation and catalytic activity, *Dalton Trans.* **43** (2014) 2079-2087.

3. J. A. Kurzman, L. M. Misch, and R. Seshadri, Chemistry of precious metal oxides relevant to heterogeneous catalysis, *Dalton Trans.* **42** (2013) 14653-14667.

2. M. W. Gaultois, P. T. Barton, C. S. Birkel, L. M. Misch, E. E. Rodriguez, G. D. Stucky and R. Seshadri, Structural disorder, magnetism, and electrical and thermoelectric properties of pyrochlore $Nd_2Ru_2O_7$, *J. Phys.: Condens. Matter* **25** (2013) 186004(1-10)

1. L. M. Misch, J. A. Kurzman, A. R. Derk, Y.-I. Kim, R. Seshadri, H. Metiu, E. W. McFarland, and G. D. Stucky, C-H bond activation by Pd-substituted CeO_2: Substituted ions *versus* reduced species, *Chem. Mater.* **23** (2011) 5432-5439.

Abstract

Platinum group metal oxides for heterogeneous catalysis: Novel synthesis and advanced characterization

by

Lauren M. Misch

Platinum group metals (PGMs) are well established and widely used for catalytic processes. It has been demonstrated that PGMs can be superior catalysts for hydrocarbon conversion reactions compared to the industry standard. However, the findings in academic labs cannot always translate directly to industrial usage. One limitation to using PGMs for large scale processes is sometimes cost. Access to an inexpensive and highly efficient catalyst could be a step towards using recovered hydrocarbons, in the form of natural gas and shale gas, more widely for energy production.

While platinum group metal species have been intensively examined, less is know about reactivity associated with ionic PGMs in oxides. Using ionic species could be a route to achieving more efficient conversion of mixed hydrocarbon feedstocks to fuels and commodity chemicals. The work presented in this dis-

sertation focuses on Pd–substitution in binary and complex oxides along with model compounds containing noble metals, with the aim of preparing an inexpensive and robust C–H bond activation catalyst. With an emphasis on preparation methods and careful characterization, it has been a goal of this work to establish structure–property relationships in oxide catalysts.

Initial work on Pd–substitution in CeO_2 has lead to the development of ultrasonic spray pyrolysis (USP) as a method for preparing substituted oxides having relatively high surface area. Phase pure Pd–substituted perovskites were also prepared using this technique. Methane partial oxidation reactions on Pd–substituted CeO_2 provided some understanding of Pd substitution in oxides. It was determined that ionic Pd when substituted in CeO_2 is readily reduced to *fcc*-Pd. Investigation of more complex oxides that could stabilize ionic Pd under reducing conditions through inductive effects became the target of subsequent research.

Pd–substituted LnFeO$_3$ (Ln = Y, La) showed promising results for increased stabilization of Pd ions under methane partial oxidation conditions. Microwave-assisted heating methods were employed to to prepare these materials very rapidly. With just several minutes of microwave-assisted heating, Pd–substituted perovskite materials were prepared for characterization and testing. With the help of our collaborators, Pd–substituted $LaFeO_3$ was applied as a catalyst precursor material for aryl chloride coupling under mild conditions.

The focus was shifted to model compounds, noble metal complex oxides, La_2BaPdO_5 and La_2BaPtO_5, already having unique noble metal sites. The thermal stability of these complex oxides compared to binary oxides was both an attractive property for probing ionic PGM catalysis and a fascinating feature, worthy of further investigation. Using density functional theory, the electronic structures of La_2BaPdO_5 and La_2BaPtO_5 were compared to those of the binary PdO and PtO oxides. It was determined that a shift in the O 2p band is responsible for the increased stability in complex oxides.

Through this study of Pd ions, we have developed two novel methods for preparation of substituted and stiochiometric oxide materials. A combination of characterization methods, including X-ray diffraction and X-ray photoelectron spectroscopy, are required to understand the structure of these complicated materials. Often times, more advanced characterization, such as neutron diffraction and extended X-ray absorption fine structure measurements, provide the necessary insights to understanding the structures and properties of oxide catalysts. In this dissertation, preparation and characterization are emphasized for ionic PGM and oxide catalysts.

Contents

List of Figures

List of Tables

Chapter 1

Introduction to catalysis by noble metal oxide catalysts

1.1 Overview

Catalysis plays a crucial role in nearly every aspect of our daily lives. It is estimated that almost half of the nitrogen in our bodies was originally fixed through the Haber-Bosch process for ammonia production. That same process generates enough fertilizer for agriculture to feed a third of our world population.[1] Many major processes in the body are catalyzed by enzymes,[2] and catalytic converters for vehicular emissions are crucial for mitigating the release of toxic gases to the atmosphere.[3] Alwin Mittasch, who discovered the Fe-based catalyst for the Haber-Bosch process, highlighted the utility and necessity of catalysis when he said “Chemistry without catalysis, would be a sword without a handle, a light without brilliance, a bell without sound.”

Both homogeneous and heterogenous catalytic reactions are important to study and understand. Homogeneous catalysis refers to reactions in which the catalyst and the reactants are of the same phase. Most commonly this occurs with solution based catalysts and reactions. Homogeneous catalysis is hugely important for organometallic chemistry. One notable example is the Wacker process, in which ethylene is oxidized to acetaldehyde in the presence of a tetrachloropalladate catalyst. In many cases, both homogeneous and heterogenous, noble metals are essential for a multitude of catalytic processes. In this case, Pd is an important component of this homogeneous catalyst.

Heterogeneous catalysis refers to reactions in which the catalyst and reactants are of different phases. In this work, I will discuss solid catalysts in both solution reactions and gas phase reactions. Of paramount importance for organic chemistry and the pharmaceutical industry is the Suzuki–Miyaura reaction, in which Pd metal catalyzes C–C cross coupling in solution.[4] Coupling reactions play a critical role in the streamlining of synthetic routes for the production of specialty chemicals and pharmaceuticals. This type of coupling was originally catalyzed homogeneously by Pd. However, a heterogeneous Pd catalyst has many advantages, such as ease of catalyst separation from the product and recyclability. There has been debate about whether this process is truly homogeneously or heterogeneously catalyzed; there is evidence to suggest that solid Pd may undergo leaching into solution, thereby acting like a homogeneous rather than heterogeneous catalyst.[5] Regardless, Pd-catalyzed coupling reactions continue to be the subject of much investigation.

Gas phase reactions that occur over solid catalysts constitute a considerable portion of large–scale industrial processes for energy conversion.[6] These types of reactions also occur in automotive emissions catalysis, which continues to be an enormous area of both academic and industrial research. Noble metals exhibit very good behavior for a number of these processes, but usage can sometimes be cost prohibitive. For example, catalytic converters are sometimes the target of theft due to the high cost of precious metals. It would be ideal to harness the excellent reactivity associated with noble metals in robust and recyclable catalyst formulations with substantially reduced noble metal loadings.

One method for reducing the amount of noble metals required for a reaction is substitutional doping. However, this raises questions about the active species for catalysis: Conventionally, metallic species are known to be reactive for a variety of processes, but noble metal ion substitution into oxides brings to light the possibility of catalysis by ionic species. It has been demonstrated that Pd ions substituted into oxides display interesting redox cycling performance, between metallic and ionic states.[7] As-prepared materials contain ionic Pd, and reducing conditions convert Pd ions to Pd metal. Subsequent reoxidation brings Pd back into the oxide lattice as an ionic species. Li *et al.* have shown with Pd-substituted $YFeO_3$ that metallic Pd particles can be detected using transmission electron microscopy after reduction, but images of the as-prepared and re-oxidized materials show no Pd metal regions (Figure 1.1). It has been further shown that ionic Pd can be, in fact, more active than metallic Pd for certain reactions, such as CO oxidation. Singh *et al.* demonstrated that as-prepared, ionic Pd-substituted $BaCeO_3$ is active at lower temperatures for CO oxidation than reduced, metallic Pd supported on $BaCeO_3$, shown in Figure 1.2. Exploration in the area of ionic noble metals and oxides as heterogeneous catalysts is relatively novel, and suggests a potential solution to the problem of noble metal abundance and use for industrial processes. Keeping costs low and maximizing the efficiency of energy conversion processes through the use of ionic noble metal catalysts could be a major contribution to the imminent clean energy demands of our society.

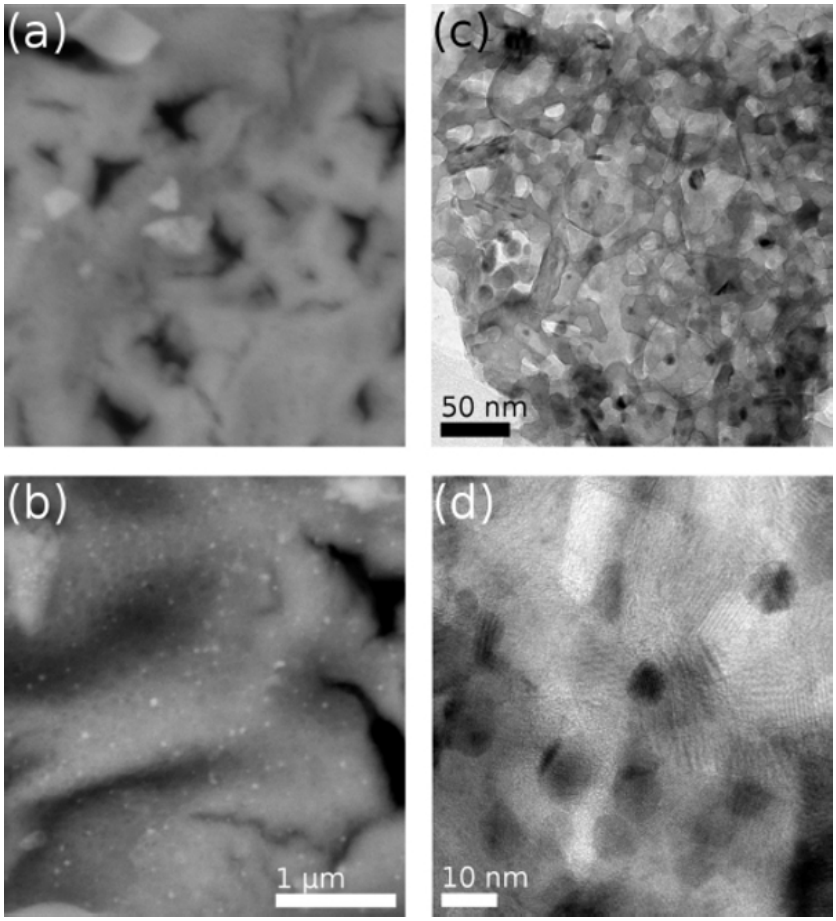

Figure 1.1: (a) Backscattered electron image of as-prepared $YFe_{1-x}Pd_xO_{3-\delta}$, $x = 0.10$). (b) Same sample after reduction, at the same magnification, showing Pd nanoparticles observed as light spots in the backscattered electron image. (c and d) Transmission electron microscope images of the reduced $YFe_{1-x}APd_xO_{3-\delta}$, $x = 0.10$) sample acquired at two different magnifications. The fcc-Pd nanoparticles appear as dark, roughly 10 nm-sized spheres. Graph reproduced with permission from Li *et al.*, *Chem. Mater.*, reference [8], © 2008 American Chemical Society.

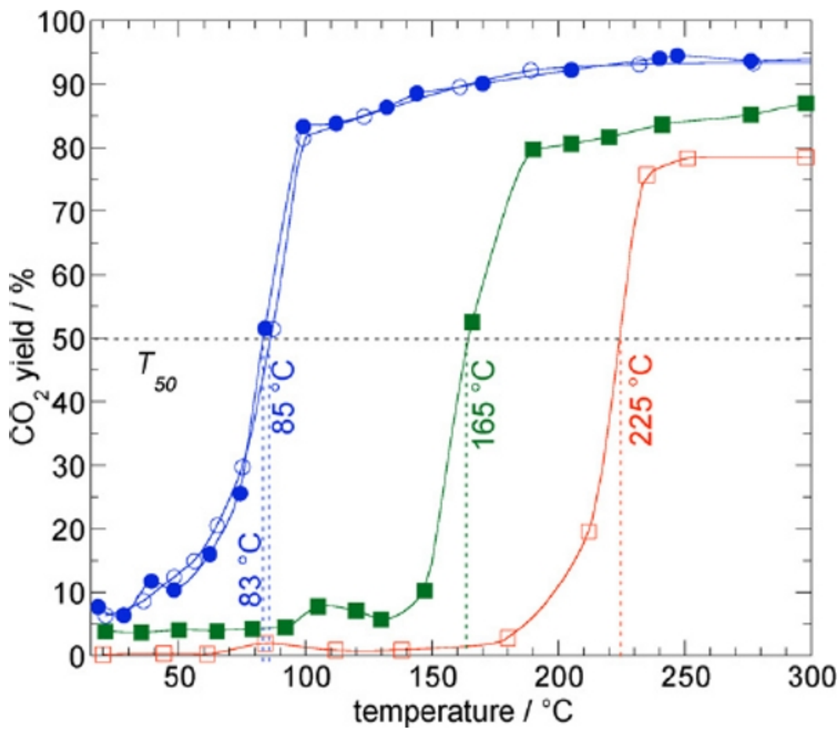

Figure 1.2: Temperature-programmed reaction profiles for the oxidation of CO (1000 ppm) by excess O_2 (10% in N2, total flow rate 50 sccm) over 100 mg $BaCe_{0.90}Pd_{0.10}O_{3-\delta}$:as-prepared (solid blue circles), reduced (solid green squares), and reoxidized forms (open blue circles), as well as $BaCeO_3$ (open red squares). Lines are drawn only to guide the eye. Graph reproduced with permission from Singh *et al.*, *J. Catal.*, reference [9], © 2007 Elsevier Inc.

1.2 C–H bond activation and oxide catalysts

Methane, in the form of natural gas or shale gas, is frequently recovered in places where infrastructure for its transport does not already exist. This recovered methane, often mixed with other hydrocarbons and even CO_2, is sometimes burned when no transport pipelines are available.[10] Because the greenhouse effect of methane is nearly 20X more potent than CO_2, flaring is a far better alternative than simply releasing recovered hydrocarbons to the atmosphere. Methane is so energy rich, however, that it seems a tremendous waste to underutilize this resource. If there existed a catalyst that could easily convert mixed hydrocarbon feedstocks containing methane into useful fuels and commodity chemicals or even compounds that are easily transported, it would have a significant impact on our society's impending energy crisis.[11] The initial motivation for the work presented here was to prepare new, inexpensive and robust catalysts for methane conversion. In an even more general sense, we aim to activate C–X bonds, where X = C, O, or H.

$$\mathrm{CH_4} + \frac{1}{2}\mathrm{O_2} \rightarrow \mathrm{CO_2} + 2\mathrm{H_2} \tag{1.1}$$

There are many large-scale industrial processes that involve hydrocarbon conversion in the presence of various other gases. Methane conversion to synthesis gas (Equation 1.1), for example, is employed by companies worldwide, and this process is a major contributor to energy production in some countries. Many of these industrial processes make use of proprietary catalysts whose structures may not even be precisely known. However, it is relatively well-established that Ni/Al_2O_3 is a methane activation catalyst, and commonly used for reactions like methane conversion to synthesis gas.[6] Although this Ni catalyst is inexpensive and servicable, it is only moderately efficient. Improving the efficiency of hydrocarbon conversion with the implementation of an inexpensive catalyst is an area of exciting potential that could reshape energy production for our society. Many labs have identified platinum group metals (PGMs) as being superior methane activation catalysts to Ni-based catalysts.[12] However, high PGM loadings tend to be required to combat sintering and to maintain catalyst lifetime, which sometimes makes PGMs an unrealistic choice for industrial-scale processes due to the high cost and limited availability. Thus it would be hugely beneficial to design a catalyst displaying reactivity comparable to PGMs without the high cost or hassle.

There is a wealth of knowledge surrounding catalysis by metal nanoparticles on various supports; reaction mechanisms are well-established for a variety of transformations facilitated by this conventional type of catalyst.[13] In contrast to their metallic counterparts, much less is known about possible catalytic reactivity associated with ionic species. It has been demonstrated that the oxide support chosen for metal nanoparticle catalysts has a significant effect on reactivity.[14] This effect may result from interactions between the metal nanoparticles and oxide support. Through these studies, it became apparent that oxide supports may themselves play an important role in reaction dynamics. Ceria, for example, is commonly used in the catalytic converter for vehicular emissions because of its high oxygen storage capacity. Ceria contributes to the efficacy of the catalytic converter just as the noble metals do for three-way catalysis.[15] Additionally, bulk oxides alone have been suggested as three-way catalysts for CO oxidation, NOx reduction and CH_4 combustion. It is known, for example, that PdO is a catalyst for CH_4 combustion. Similarly, $CuO\text{-}ZnO\text{-}Al_2O_3$ and $Fe_2O_3\text{-}Cr_2O_3\text{-}MgO$ are the known low and high temperature Water-Gas shift reaction (Equation 1.2) catalysts, respectively.[6]

$$\mathrm{CO} + \mathrm{H_2O} \rightarrow \mathrm{CO_2} + \mathrm{H_2} \tag{1.2}$$

Recently, substitutional doping of noble metal cations in oxide hosts, such as ceria, became an exciting way to further consider metal support interactions in a more intimate mixture, and specifically effects on the oxide became of interest. It has been shown that size effects are pronounced for metal nanoparticle catalysts;[16] introducing a single atom as a dopant into an oxide host lattice is at one end of the spectrum of the ongoing size-effects investigation. Identifying active sites on substituted oxide catalysts has been the subject of much research. In some substituted oxide materials, it is not unexpected that oxygen vacancies will form for charge compensation when dopant ions are introduced into the lattice. Extensive theoretical work has been done in the area of oxygen vacancy formation energies, as these sites have been suggested as potential active sites for various reactions.[17] The Hegde group has done considerable experimetal work in the area of noble metal substitution in binary oxides for catalysis.[18] Specifically they have demonstrated that noble metals substituted into CeO_2 are superior CO oxidation catalysts to the independent oxides alone or the metallic species. Some examples of the effects of substitution in CeO_2 on CO oxidation performance are shown in Figure 1.3.

For the most part, it is still not known where active sites reside for many catalytic processes on oxides. Instead of attempting to identify active sites, our strategy was to look directly at ionic noble metal species and probe their catalytic reactivity. We considered both noble metal substituted oxides, and model compounds – complex oxides containing a crystallographically well-defined site for the noble metal cation. The challenge with these materials is preparing stable noble metal ions in oxides. PdO readily reduces to Pd metal under even slightly

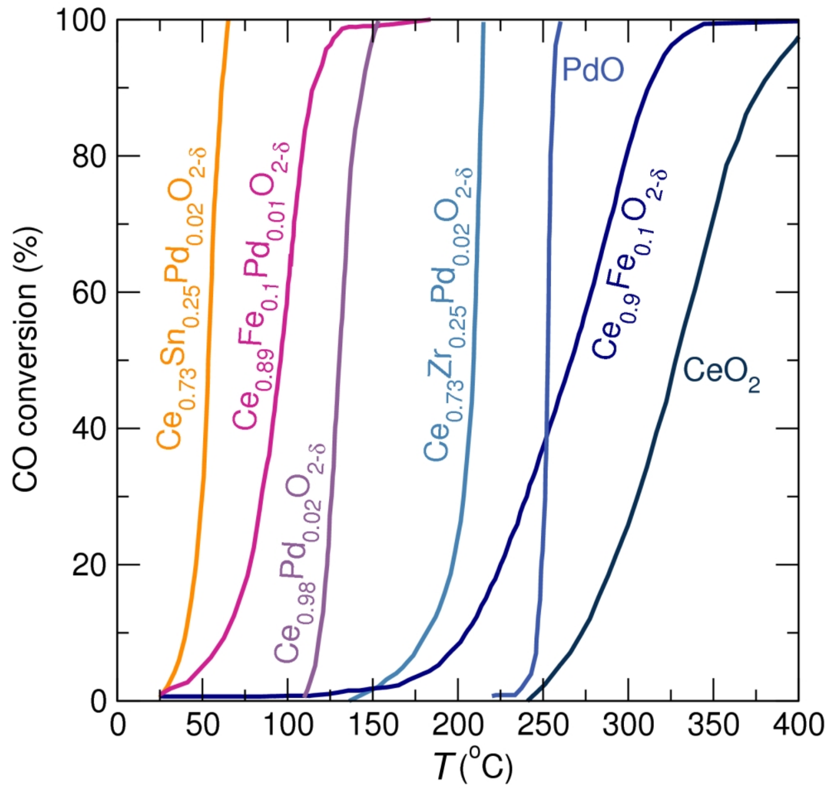

Figure 1.3: CO oxidation light-off curves under stoichiometric CO:O_2 conditions (1%:1%, inert balance) for ceria, a variety of substituted ceria catalysts, and PdO. The activity of CeO_2 is significantly promoted by the substitution of Pd^{2+}, and can be further promoted by concurrent substitution by other transition metal or main group elements. Data adapted from Gupta *et al.*, *Chem. Mater.* 2009,[19, 20] and Baidya *et al.*, *Dalton Trans.* 2008.[21]. Reproduced with permission from reference [22] © 2013, RSC Publishing.

reducing atmosphere, therefore careful consideration must be given to host oxides that will adequately stabilize a noble metal ion, like Pd, under strongly reducing conditions. Much work has been done on noble metal substitution in various oxides. The following chapters will discuss Pd-substitution in a binary and complex oxide hosts, CeO_2 and $Ln$$FeO_3$ (Ln = Y, La), and two model compounds containing noble metals, La_2BaPdO_5 and La_2BaPtO_5.

1.3 Preparation methods

A few conventional methods of preparation for oxide catalysts include sol-gel, combustion, and solid-state methods. These methods have many strengths, and various aspects of these techniques have been incorporated into the new methods I have contributed to developing. Sol-gel synthesis allows for very good mixing of ions in solution. The guaranteed intimate contact that ions can achieve in solution compared to grinding powders together, for example, may allow materials prepared with sol-gel methods to be more resistant to phase separation. Additionally, the use of a gelation agent, such as citric acid or urea, may contribute to higher surface area materials, which is always desirable for catalytic materials. Combustion synthesis, or self-propagating high temperature synthesis (SHS), makes use of rapid heating. Precursor powders and an oxidizing agent (usually oxalyldihydrazide, or ODH) are dissolved in a minimal amount of solvent, usually water with some acid, and placed into a furnace at elevated temperature. The mixture combusts quickly and the resulting powder is then annealed. This very rapid heating can force ions to be kinetically trapped in certain positions rather than allowing additional time for ions to segregate. [18] Solid state methods generally begin with grinding precursor powders together, followed by very long heatings at high temperatures. The advantage of a solid-state method is that ions with limited mobility have sufficient time and energy from the high temperatures (in excess of 1000°C) to move to the desired positions. In some cases, these conventional preparation methods have not been sufficient to stabilize noble metal ions in oxide hosts. Thus it has been one of my goals to optimize preparation methods to achieve noble metal-substituted oxides in order to probe catalytic reactivity associated with platinum group ions.

Preparing substituted oxides can be more challenging than stoichiometric oxides and sometimes requires more specialized techniques. Pyrolysis methods have been used previously to prepare oxide materials, but not necessarily to prepare substituted metal oxides. The particular method that was adapted for our purposes was originally intended to prepare mesoporous carbon materials.[23] I have developed ultrasonic spray pyrolysis (USP) for preparing substituted metal oxides.

USP for substituted oxides requires precursors that are soluble in aqueous solutions. Usually nitrates in millipore water work well. Precursors need to be well solubilized or dispersed in solution. The precursor solution is held inside a custom glass vessel with a thin plastic membrane at the bottom. The vessel sits inside a water bath with a vibrating ultrasonic disc below the membrane. A domestic humidifier can be modified to accommodate the precursor vessel. Ultrasonic waves travel through the water bath, past the plastic membrane, and into the precursor solution, generating a fine mist. The mist is then carried by flowing compressed air into a tube furnace at variable temperature. A schematic of this reaction setup is shown in Figure 1.5. The reaction takes place inside the tube furnace and the carrier gas deposits oxide products in water bubblers connected by Tygon(TM) tubing at the end of the furnace. Materials prepared with this method have a micron-sized hollow-sphere morphology. Droplets of precursor mist are carried through the furnace, liquid evaporates out of the droplet, and a shell is left behind. It has been demostrated that these shells are maintained even after heating to 600° in flowing methane and oxygen. Although attractive for imaging, the morphology of these materials has not yet proved to be significant for any catalytic properties.

USP is a highly tunable method. Nearly every parameter can be adjusted to suit the conditions required to achieve a certain product. The concentration of

Figure 1.4: Photograph of the USP setup in action. On the right, mist is formed in the precursor vessel and carried into the tube furnace. Products are collected in the bubblers on the far left in this image.

ions in solution can be varied, but must remain sufficiently dilute. Generally, a total molarity of 0.05 M was best for nebulizing the solution; a concentration much greater than this made it impossible for the ultrasonic humidifier to create a mist. The addition of a surfactant may decrease the surface tension and allow for a more concentrated precursor solution. The density of the mist generated by ultrasonic vibrations can be adjusted slightly with a dial on the humidifier. It's possible that attaching a variac (variable alternating current) device to the humidifer could allow for more significant tuning of the mist density. The composition and flow of the carrier gas can be easily modified as well. Compressed air was readily available and because oxide preparation was desired, there was no need for an inert or reducing atmosphere. A flow meter set at 5 scfm was used to control the flow of mist into the tube furnace. The mist created from the aqueous solution was heavy enough that a flow much less than 5 scfm was not sufficient to carry the mist to the furnace. However, a slower flow rate may be desirable as the mist spends a very short time in the tube furnace, and the reaction to form oxide products occurs very rapidly. Some unreacted precursors may be collected on the product side of the furnace.

The temperature of the furnace can also be easily modified. The tube furnace used will dictate the allowed temperature range. We found that materials could be prepared as low as 500°C and as high as 1000°C with our system. It was

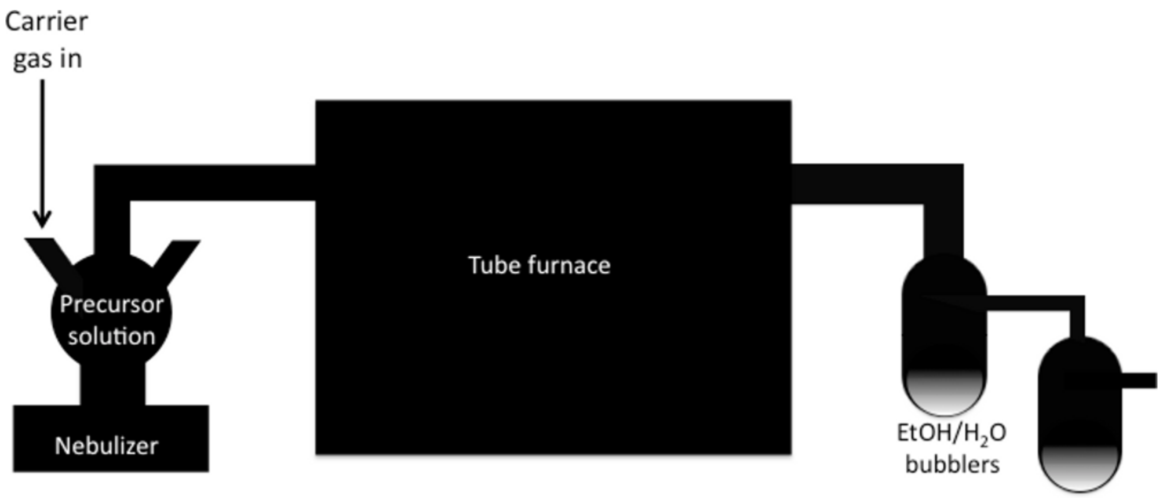

Figure 1.5: A schematic of the USP setup. The introduction of carrier gas move the mist generated by the neublizer in the precursor vessel into the tube furance. Oxide products are collected in the bubblers.

always our goal to decrease the maximum temperature required for materials preparation in the event that any of our catalyst materials became of interest for industrial applications. Materials prepared closer to ambient temperatures are less expensive and more attractive at the industrial level. Additionally, materials prepared with lower temperatures are less likely to sinter than materials prepared at high temperatures and therefore could have relatively higher surface areas. It was our goal to obtain phase pure and crystalline materials, with the potential for having high surface area. We were able to successfully prepare Pd–substituted CeO_2 and Pd–substituted LnFeO$_3$ (Ln = Y, La) with USP. This method was also used to prepare $Nd_2Ru_2O_7$, for which we studied its structural disorder, magnetism, electrical and thermoelectric properties.[24]

Another very rapid preparation method recently developed is microwave-assisted heating. Conventional solid-state reactions can be completed with microwave-assisted heating in several minutes compared to several days or weeks in a high temperature furnace. This method has been used to prepare a myriad of oxide materials for various applications.[25–28] Materials can be prepared using sol-gel microwave-assisted methods or solid-state microwave assisted methods. In a sol-gel synthesis, precursors soluble in aqueous solutions (sometimes containing alcohol) are well mixed along with a gelation agent, usually citric acic. The solution is heated at 65°C on a stir plate for about 12 h or until a dried gel has formed. This is then transfered in to a small box furnace at 125°C for another 12 h. A powder is then collected and heating in the microwave. The precursor powder is placed inside a small alumina crucible, which is then settled into a larger crucible containing carbon microwave susceptor material. Microwaves do not directly heat the precursors. Instead, the carbon susceptor is heated and heat is transferred to the inner crucible. The crucibles are placed in an alumina fiber board housing and then inside the microwave on the turntable. Alternatively, precursor powders can be ground together in a mortar and pestle, just like a conventional solid-state preparation, and then placed inside the inner alumina crucible for microwave-assisted heat-

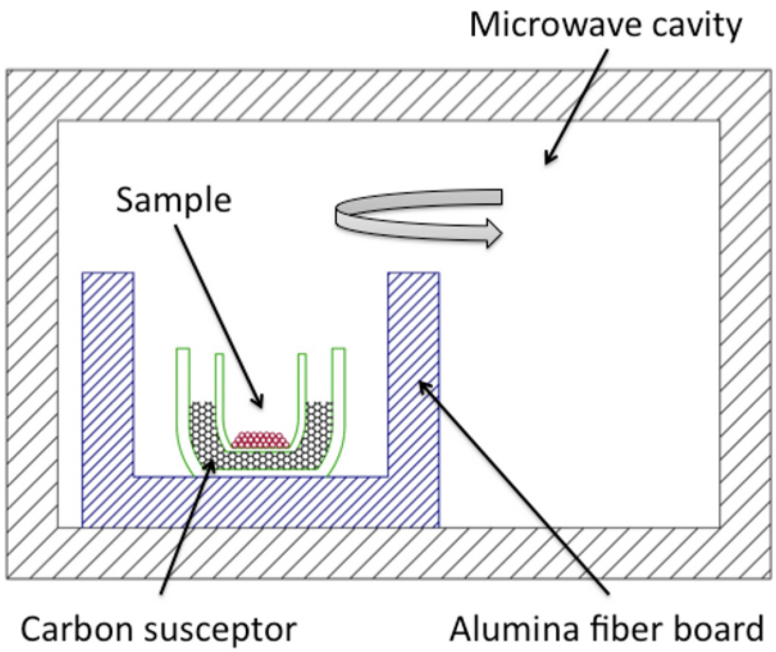

Figure 1.6: A schematic of the microwave reaction setup. Indicated is the inner crucible, containing the precursor materials; the outer crucible, containing the carbon susceptor material and the inner crucible; and the alumina housing, which contains both crucibles.

ing. Both methods have been very successful. The sol-gel microwave-assisted heating method was optimized for Pd-substituted LnFeO$_3$ (Ln = Y, La), and the solid-state microwave-assisted heating method for La$_2$BaPdO$_5$ and La$_2$BaPtO$_5$.

The major advantage of USP was the high surface area obtained. For microwave-assisted heating, the most significant advantage is the amount of time saved by this extremely rapid heating method. Both methods are highly tunable and amenable to modification for the desired products. The specific conditions for the materials discussed in this work are described in detail in the following chapters.

Chapter 2

Pd–substituted oxides for heterogeneous catalysis

2.1 C-H bond activation by Pd-substituted CeO_2

2.1.1 Introduction

Heterogeneous catalysis on the surfaces of platinum group metals (PGMs) has long been studied, and the fundamental processes are now understood in

[1] Substantial portions of this chapter have been reproduced with permission from: L. M. Misch, J. A. Kurzman, A. R. Derk, Y.-I. Kim, R. Seshadri, H. Metiu, E. W. McFarland, and G. D. Stucky, C-H bond activation by Pd-substituted CeO_2: Substituted ions *versus* reduced species, *Chem. Mater.* **23** (2011) 5432-5439, reference [29] © 2011 American Chemical Society.

extraordinary detail from both experimental and theoretical bases. Much less is known about the surface chemistry of PGM species when they exist as ions in solid-state materials such as simple and complex oxides.[30]

In a recent review, Thomas[31] promotes the idea of catalysis on single active sites, well-separated from one another, in a manner that mimics homogeneous catalysis. This important design principle for novel approaches to element-efficient heterogeneous catalysis has been demonstrated through the use of ionic species substituted on cation sites in metal oxides, including the use of Pd^{2+}-substituted metal oxides. Hegde and co-workers[18] have shown conclusively that substituted PGM ions are active for CO removal from gas streams,[32] and as automotive threeway catalysts.[33] Pfefferle and co-workers[34] have found that in CH_4 combustion, the role of PdO and related species is crucial. It has been further suggested that the oxidized state of Pd^{2+} (as opposed to metallic Pd^0) may be the most active species when using substituted complex oxides for catalysis.[8, 9, 35] Perhaps the most compelling evidence for using Pd-substituted oxides for heterogeneous catalysis comes from the successful application of intelligent catalysts for automotive emissions control.[7]

In this contribution, we use ultrasonic spray pyrolysis (USP) as a simple and clean method to prepare Pd-substituted CeO_2 catalysts with particle sizes in the sub-10 nm range. We have characterized these materials using electron microscopy, X-ray photoelectron spectroscopy, and synchrotron X-ray diffraction (XRD) and observe that Pd substitutes in the lattice at least up to $x = 0.10$ in $Ce_{1-x}Pd_xO_{2-\delta}$.

In this work, $Ce_{1-x}Pd_xO_{2-\delta}$ was tested for CH bond activation reactions. While there are reports of complete and partial CH_4 oxidation over Pd,[36–40] a wealth of literature has been published on Pd and CeO_2 containing catalysts for CH_4 combustion,[41–48] CO oxidation,[21, 32, 33, 49–51] and NOx abatement.[52] The oxygen storage capacity of CeO_2 is enhanced when substituted with Pd,[20, 53–55] and doping promotes the formation of oxygen vacancies in catalysis.[33, 56, 57] It has also been demonstrated that CeO_2 supported catalysts and Pd supported on CeO_2 are active for the water-gas shift reaction.[58–60] Additionally, it was also shown that a Pd-containing catalyst effectively converted CH_4 to a methanol derivative in solution.[61]

The study of CH_4 activation reactions has important energy applications. While large reserves of CH_4 exist and considerable portions of these reserves are currently used to heat homes and generate hydrogen for other synthetic processes, it is widely accepted that the conversion of CH_4 to liquid hydrocarbon fuels efficiently with an inexpensive and robust catalyst would be a substantial contribution to alternative energy research.[62] The usual FischerTropsch strategy requires oxidation to mixtures of CO and H_2, which are then converted to higher hydrocarbons. Alternate partial oxidation strategies could be a more direct route to valuable products. For example, dry reforming of CH_4 is of value because recovered CH_4 is often found in the presence of CO_2. As large-scale separations are expensive, it would be convenient to identify a catalyst that efficiently converts CH_4 to useful products in the presence of CO_2.[10]

We address the following questions in this work: (i) Does USP provide a useful route to single-phase Pd-substituted CeO_2 with high surface area? (ii) Can Pd-substituted CeO_2 be used as a catalyst for CH_4 activation in the presence of O_2 (partial oxidation) or CO_2 (dry reforming)? (iii) Can it be concluded that a substituted PGM ion is active for CH bond activation? We found that Pd-substituted CeO_2 behaves in a manner that is nearly indistinguishable from supported Pd on CeO_2 as a result of the reduction of Pd^{2+} ions to Pd nanoparticles on CeO_2. This study complements prior work on the use of Pt substituted CeO_2 as a catalyst for CH_4 activation.[63]

2.1.2 Experimental details

Preparation *via* Ultrasonic Spray Pyrolysis (USP) Pd-substituted CeO_2 was prepared using USP. The USP setup is based on the apparatus described by Skrabalak *et al.*[23] which they used for the preparation of nanoporous carbon. The precursor solution, containing $Ce(NO_3)_3 \times 6H_2O$ (99%, Aldrich) and $Pd(NO_3)_2 \times 2H_2O$ (99.999%, Aldrich) dissolved in the appropriate molar ratios in Millipore water, was nebulized in the custom reaction vessel over a Sunpenton humidifier.

This method can be applied to many oxide materials with the simple adjustment of precursors. Generally, nitrates in aqueous solution work quite well. If the desired material does not have readily available water-soluble precusors, the solution can be adjusted to contain some parts alcohol or acid with water to allow adequte solubility. For example, acetates and acetylacetonates can be used with a water/ethanol mixture or water/butanol. It was determined that 0.1M was an appropriate concentration for precursors solutions so that the humidifer could produce a mist.The Sunpenton humidifier can be easily modified to adjust the density of mist produced. The precursor mist was carried by compressed air through a vitreous silica tube in a Lindberg Blue/M tube furnace at 500°C. The temperature of the tube furnace can also be easily adjusted to suit the preparation of various materials.

Product powders were collected in bubblers containing 4:1 H_2O/EtOH. The suspensions were evaporated in crystallization dishes at 80°C overnight, and the dry powder was collected. We have found that bubblers containing water only for collection are sometimes preferable. Any alcohol contained in the collection bubblers destroyed the $BaCeO_3$ phase, for example. We found that evaporation was the best method for powder collection. Vacuum filtration would not allow for sufficient collection of oxide powders. It was later determined from microscopy that particles were much too small to be collected on standard filter paper. Centrifugation is acceptable, but more time consuming than simply allowing the liquid to evaporate overnight.

From start to finish, USP takes about 24 h to produce between 500 mg and 1 g of desired material. This method has been applied to other oxide materials, specifically ABO_x perovskites, and will be discussed later in this chapter.

Characterization techniques Room temperature XRD data was collected on a Philips XPERT diffractometer, and *in-situ* variable temperature diffraction experiments were performed with a Bruker D8 diffractometer equipped with an Anton Parr hot-stage. Synchrotron X-ray powder diffraction patterns were collected in transmission mode at room temperature on beamline 11-BM at the Advanced Photon Source, Argonne National Laboratory, with an X-ray energy of near 30 keV. No evidence for sample degradation or damage was observed. Rietveld refinements were performed using the XND code.[64] X-ray photoelectron spectra were obtained on a Kratos Axis Ultra Spectrometer with a monochromatic Al–Kα source (E = 1486.7 eV). Samples were mounted on a stainless steel sample holder using double-sided carbon tabs. The residual pressure inside the analysis chamber was below 7×10^{-9} Torr. Survey spectra over wide ranges of binding energy were acquired using an analyzer pass energy of 160 eV, and spectra of Pd 3d levels were acquired at a pass energy of 80 eV. Spectra were calibrated to the C 1s peak from adventitious hydrocarbons, expected at a binding energy of 285.0 eV. For peak fitting of the spinorbit doublets in high resolution scans, the $d_{3/2}$ to $d_{5/2}$ peak area was constrained to a ratio of 2/3.

Scanning electron micrographs (SEMs) were acquired on an FEI XL40 Sirion FEG digital scanning microscope. SEM sample stages were sputtered with Au plasma prior to imaging to reduce sample charging. Transmission electron micrographs (TEMs) were taken on an FEI Tecnai G2 Sphera Microscope. TEM copper-coated Cu grids were prepared by dropcasting a dilute suspension of product in ethanol onto grids. BrunauerEmmettTeller (BET) surface area measurements were made on a MicroMetrics TriStar 3000 porosimeter using N2 as probe gas.

Catalytic testing Catalytic testing was carried out in a home-built packed bed reactor, equipped with MKS mass flow controllers and mass spectrometer (SRS) for data acquisition. Quartz tubes (inner-diameter = 4 mm) were packed with 25 mg of catalyst and 50 mg of HPLC grade aluminum oxide (Aldrich) to prevent hotspots, with quartz wool plugs on both ends of the powder. The loosely packed powder occupies a length of 1 cm to maintain a space-time of 0.18 s with a total flow rate of 30 sccm. Reactions were ramped from room temperature to 600°C at a rate of 10°C/min. Catalysts were pretreated with Ar, 20% H_2/Ar balance, or 20% O_2/Ar balance. During partial oxidation of CH_4, a 2:1 ratio of CH_4/O_2 was set to flow over the catalyst. This ratio is the stiochiometric amount to produce synthesis gas (Reaction **??**. All gases had a stated purity of better than 99.99%.

$$\mathrm{CH_4} + \frac{1}{2}\mathrm{O_2} \rightarrow \mathrm{CO_2} + 2\mathrm{H_2} \qquad (2.1)$$

Anticipated products for partial oxidation reactions (2:1 CH_4/O_2) include combustion productions (CO_2 and H_2O), synthesis gas (various ratios of H_2 and CO), oxidative coupling products (C_2H_6, C_2H_4, C_2H_2), and methanol. The mass spectrometer was set to record the activity of the m/z ratios corresponding to these products. While heating any hydrocarbon in the presence of oxygen to high temperatures, combustion products are expected. It is possible for unreacted CH_4 to react with any CO_2 produced from combustion and proceed to do dry reforming of CH_4 to produce synthesis gas (CO + H_2). If CO and H_2 were produced during partial oxidation of CH_4, catalysts were tested for dry reforming of CH_4, in which CH_4 reacts with CO_2 produced from combustion. If CH_4 reacts with CO_2 to produce synthesis gas, then this is a possible mechanistic route for syngas production during partial oxidation reactions.

The anticipated products for dry reforming of CH_4 (1:1 CH_4/CO_2) are synthesis gas (H_2 and CO). The mass spectrometer was set to record the m/z ratios corresponding to all of the products listed for partial oxidation reactions. All subsequent reactions were chosen based on the materials behavior during partial oxidation conditions. Other reactions studied in this work include ethylene hydrogenation (1:1 C_2H_4/H_2) to 300°C heated at 10°C/min. Anticipated products of this reaction include ethane and water. The results of characterization of $Ce_{1-x}Pd_xO_{2-\delta}$ and catalytic testing follow.

2.1.3 Results and Discussion

Characterization of$Ce_{1-x}Pd_xO_{2-\delta}$. Pd-substituted CeO_2 ($Ce_{1-x}Pd_xO_{2-\delta}$) was prepared with x = 0.025, 0.05, 0.075, 0.1 via USP. Representative scanning electron micrographs for a sample with x = 0.05 of the as-prepared powders are shown in Figure 2.1(a). The hollow sphere morphology of the powders is evident in the higher magnification image presented in the inset. The morphology presumably results from evaporation of liquid as the mist traveled through the furnace, leaving behind polydispersed hollow spheres. Despite the relatively large size of the agglomerates, the crystallites of which the spheres are composed are rather fine, with grain sizes on the order of 5 nm, as seen in the transmission electron micrographs of Figure 2.1(b). The$Ce_{0.95}Pd_{0.05}O_{2-\delta}$ powder prepared by USP has BET surface area of about 32 m^2/g.

High-resolution synchrotron X-ray powder diffraction patterns and corresponding Rietveld refinements are shown in Figure 2.2 for the as-prepared samples and after calcination at 700°C for 16 h. Pure fluorite CeO_2 is the only phase observed, and no phase segregation occurs in any of the compositions. We did not attempt to prepare materials with Pd concentrations higher than 10 mol %. The diffraction profiles are broader in the substituted materials, relative to pure CeO_2, and this is especially pronounced in the calcined samples2.3. Refinements were performed with models fixed at the nominal stoichiometry of each sample ($\delta = x$) with Pd residing on the Ce site, and the atomic displacement parameters (ADP) of Pd and Ce were constrained to the same value. Because the Pd and O occupancies, ADPs, and global scale factor are strongly correlated, the occupancies cannot be refined. For this reason, it is not possible to directly demonstrate the solid solubility of Pd in CeO_2 from average structure (Rietveld) refinement techniques using XRD data.

Thermodiffraction data shows the evolution of the 111 and 200 reflections of

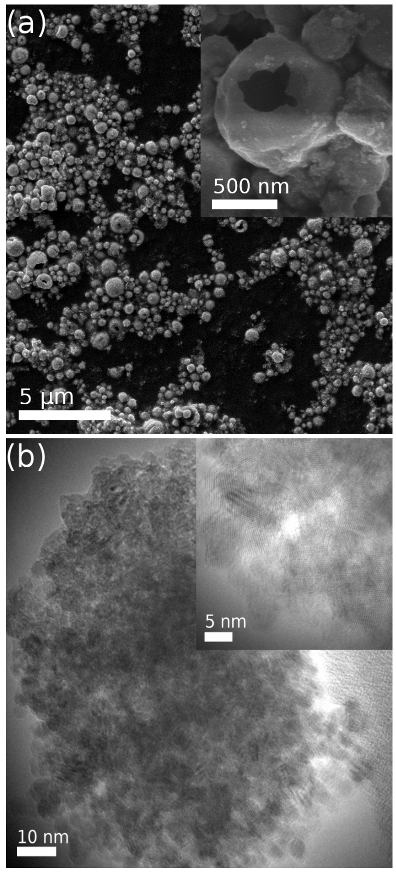

Figure 2.1: Representative scanning and transmissions electron micrographs for $Ce_{1-x}Pd_xO_{2-\delta}$](a) Scanning electron micrograph of $Ce_{0.95}Pd_{0.05}O_{2-\delta}$particles prepared by nebulized USP showing a hollow sphere morphology. (b) Transmission electron micrograph of the $Ce_{0.95}Pd_{0.05}O_{2-\delta}$particles showing that hollow spheres are composed of approximately 5 nm crystallites, confirming the correlation length obtained from line broadening from synchrotron XRD. Figure reproduced with permission from Misch *et al.*, *Chem. Mater.*, reference [29], © 2011 American Chemical Society.

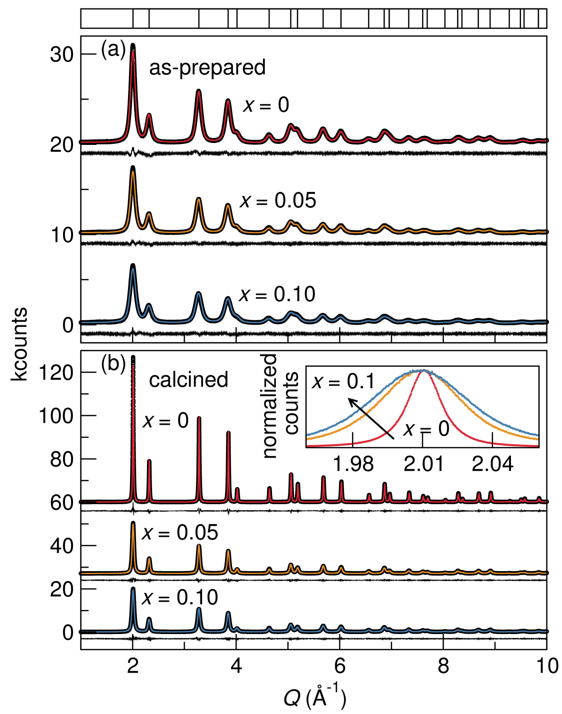

Figure 2.2: (a) Synchrotron XRD data for as-prepared$Ce_{1-x}Pd_xO_{2-\delta}$ with $x = 0$, 0.05, and 0.1. All samples are single-phase fluorite. Vertical bars in the topmost panel indicate expected fluorite CeO_2 reflection positions. (b) Diffraction from samples after calcining in air for 16 h at 700°C, with significant peak narrowing because of sintering. The inset shows the strongest reflection, with height normalized, for samples with increasing Pd^{2+} substitution, x. Samples with higher x values are seen to possess significantly broader peaks. Figure reproduced with permission from Misch *et al.*, *Chem. Mater.*, reference [29], © 2011 American Chemical Society.

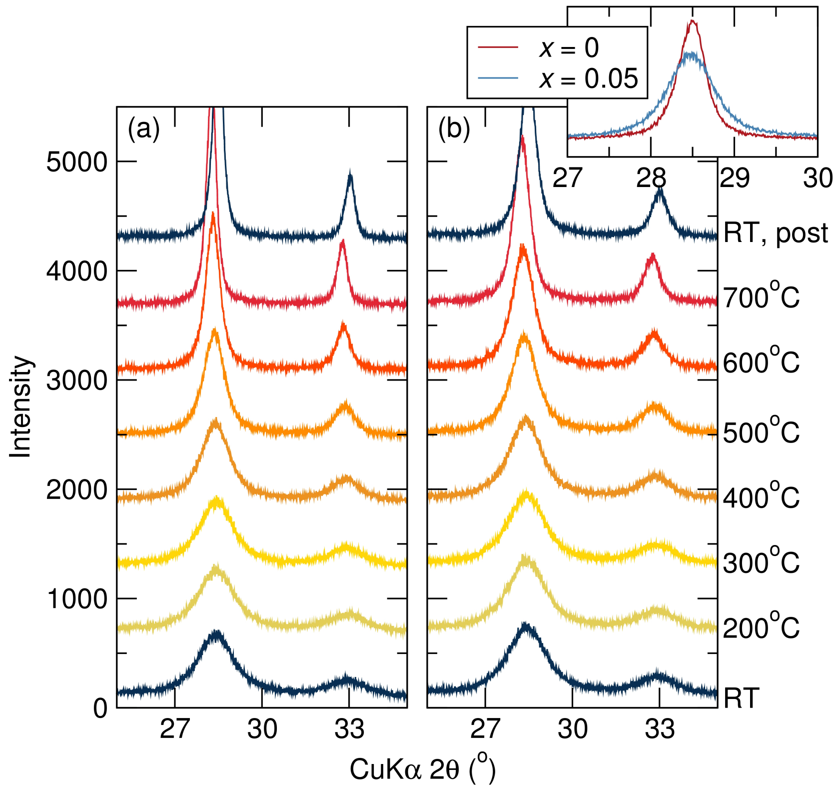

Figure 2.3: Thermal X-ray diffraction data for(a) CeO_2 and (b) $Ce_{0.95}Pd_{0.05}O_{2-\delta}$. Samples were heated in air on a Pt stage with a dwell time of 1 h at each temperature increment. $Ce_{0.95}Pd_{0.05}O_{2-\delta}$maintains a broad peak shape during heating and is more resistant to sintering than CeO_2. No phase separation (for example, of PdO) is observed in the substituted material. The inset compares the braod peak shape maintained by$Ce_{0.95}Pd_{0.05}O_{2-\delta}$relative to CeO_2 after the heating program. Figure reproduced with permission from Misch *et al.*, *Chem. Mater.*, reference [29], © 2011 American Chemical Society.

CeO_2 between room temperature and 700°C for unsubstituted CeO_2 (x = 0) and 5% Pd-substituted CeO_2 (x = 0.05). Diffraction profiles of pure CeO_2 narrow with increasing temperatures, while the peak widths of the substituted material remain significantly broader. The distinct behaviors are indirect evidence that Pd is substituted into the CeO_2 lattice, and suggests that sintering may be suppressed in the substituted material. These points are discussed in greater detail with respect to analysis of synchrotron X-ray powder diffraction studies of the $Ce_{1-x}Pd_xO_{2-\delta}$ series.

There are considerable challenges associated with structure determination and refinement of nanoscale materials from Bragg scattering-based diffraction analysis. While it is known that systematic errors arise in the determination of lattice parameters for nanocrystalline materials,[65] this is infrequently acknowledged. Using the Debye function, Palosz and coworkers simulated diffraction patterns for perfect SiC nanocrystallites with sizes ranging from 3 to 8 nm and refined the simulated data by the Rietveld method.[65] Interestingly, they found that in the approximation of a perfect experiment, that is, no sample-offset error, the refined lattice constant was systematically overestimated, increasingly as the crystallite size decreased. In refinements approximating an imperfect experiment in which the sample-offset error was allowed to float, the refined lattice constant was increasingly underestimated as the crystallite size decreased. Thus, even within the approximation that a nanomaterial is a small single-crystalline piece of the bulk material, Rietveld refinement fails to accurately extract the lattice parameters. In this light, it is clear that great care must be taken when establishing trends in the variation of lattice parameters determined by Rietveld analysis.[65–67]

The situation is further complicated by the fact that nanocrystallites are not simply small portions of a bulk material. Conventional crystallographic analysis operates on the assumption that the environment of each lattice point is identical. While this may be well approximated by atoms within the core of a nanoparticle, it certainly does not apply to the under-coordinated atoms at or near the surface. For this reason, a single group of lattice constants does not capture the complexity inherent to real nanocrystals. Palosz et al. have extensively discussed limitations of Rietveld analysis for structure determination in nanocrystalline materials.[65]

With these limitations in mind, we address the observed variation of the lattice constant as a function of substitution level with caution. It is clear from the thermodiffraction and synchrotron studies that Pd-substitution in CeO_2 reduces the XRD-coherent correlation length. In Figure 2.4, the refined lattice parameters of the as-prepared and calcined samples are plotted against the nominal Pd content x. One method for reducing the error associated with lattice parameter determination in nanoparticles is to refine only the high Q portion of a diffraction pattern, although this is only effective in the approximation of a perfect crystallite. Despite this known limitation, the lattice parameters from refining over the entire Q range (open symbols) and only the high Q portion of the patterns (shaded symbols, Q >8 $\mathring{A}^{-1}$) are compared in Figure 2.4. It is immediately clear that the as-prepared samples appear to have larger lattice constants than the calcined materials. The lattice constants of the as-prepared materials are reduced when only the high Q portions of the patterns are refined; the effect is less pronounced in the calcined materials.$Ce_{1-x}Pd_xO_{2-\delta}$ seems to exhibit Végard style behavior with a lengthening of a as the Pd concentration is increased. This would be consistent with increased cation–cation repulsion arising from the removal of oxygen because of the aliovalent substitution of Pd^{2+} for Ce^{4+}. However, the Shannon–Prewitt ionic radius of 4-coordinate Pd^{2+} (0.64 Å) is significantly smaller than the radius of 8- coordinate Ce^{4+} (0.97 Å), so it is difficult to know whether the observed expansion is an artifact of differences in crystalline correlation lengths, or accurately representative of differences in the lattice constants.

To address whether the variation in the lattice parameter across the series is due to systematic differences in the crystallite sizes, we performed a Williamson–Hall analysis[68] on each of the patterns. It is important to point out that neither Scherrer nor Williamson–Hall analyses are quantitatively accurate methods for extracting correlation lengths, though they do provide reasonable first-order estimates.[65] Additionally, in the case of nanocrystallites of relatively small sizes, <10 nm, the strain parameter extracted by the WH method carries little physical meaning.[67] We elected to do a Williamson–Hall analysis because it involves fitting over the entire observed Q range, but we note that similar estimates of the correlation lengths were obtained by Scherrer analysis of a single reflection. The refined lattice constants are plotted in Figure 2.4(b) as a function of the inverse correlation length estimated from the WH analysis; the volume weighted particle sizes and strains are given in Table 1. As a function of the inverse correlation length, the lattice parameters follow an approximately linear trend. It is not possible to conclude whether the observed differences result from systematic errors inherent to the Rietveld method, or whether they genuinely reflect differences between the samples. Within the associated error, the estimated strain is almost constant across the series of as-prepared samples. In the calcined materials, the estimated strain increases significantly in going from the $x = 0$ unsubstituted material to $x = 0.025$, and then gradually increases with the Pd concentration.

It is clear that Rietveld analysis cannot provide direct evidence that Pd substitution occurs in CeO_2, complicated by the many factors we have discussed.

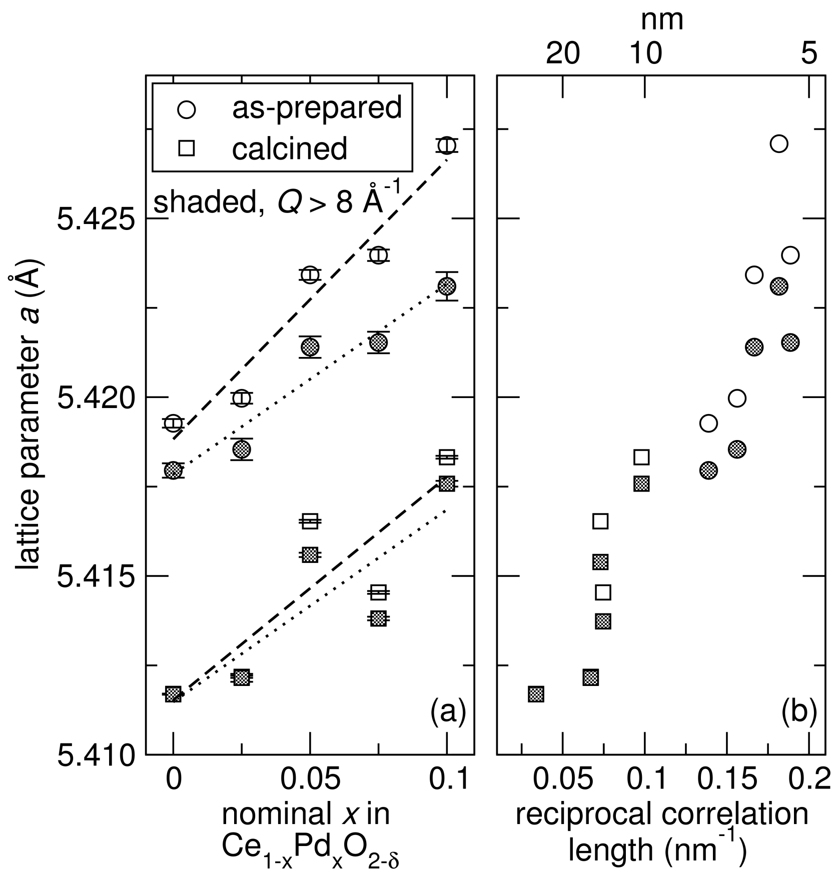

Figure 2.4: (a) Variation of the cubic cell parameter of$Ce_{1-x}Pd_xO_{2-\delta}$ as a function of nominal Pd substitution x. Data are displayed for as prepared and calcined samples separately, as described in the text. The cubic cell parameter was determined for the whole Q range of data, and separately for data with $Q >8$ $\mathring{A}^{-1}$, shown with shaded symbols. (b) Cell parameters displayed as a function of the reciprocal crystalline correlation length as obtained from Williamson–Hall analysis of synchrotron XRD data. Figure reproduced with permission from Misch *et al.*, *Chem. Mater.*, reference [29], © 2011 American Chemical Society.

Nonetheless, the fact that these are single-phase materials displaying significantly different behavior upon calcination compared to pure CeO_2, coupled with the observation that the XRD-coherent correlation length changes as a function of Pd concentration, are highly suggestive that Pd is dispersed in the CeO_2 lattice. Verification that the nominal Pd concentrations are indeed reflective of the actual compositions is obtained by fully reducing the samples to two phase mixtures of CeO_2 and *fcc*-Pd metal. A synchrotron XRD pattern and corresponding Rietveld refinement for one such sample ($x = 0.05$) are shown in Figure 2.5. The *fcc*-Pd contribution is estimated to be 4.7 mol % by quantitative phase analysis, in excellent agreement with the presumed Pd content.

Scanlon *et al.* recently described an ab initio study of Pd and Pt substitution in CeO_2 and demonstrated that because of crystal field stabilization effects, the PGM substitutents prefer to displace off the ideal Ce lattice position by about 1.2 Åto adopt square planar coordination, the most common coordination geometry for d^8 cations.[55] This result emphasizes the importance of applying structural probes that are sensitive to local environments. While EXAFS studies have been reported on the $Ce_{1-x}Pd_xO_{2-\delta}$ system,[54, 69] we are not aware of any attempts to fit models similar to the one proposed by Scanlon *et al.*

X-ray photoelectron spectroscopy (XPS) of the Pd 3d region was investigated to determine the charge state of substituted Pd in $Ce_{0.95}Pd_{0.05}O_{2-\delta}$. In-

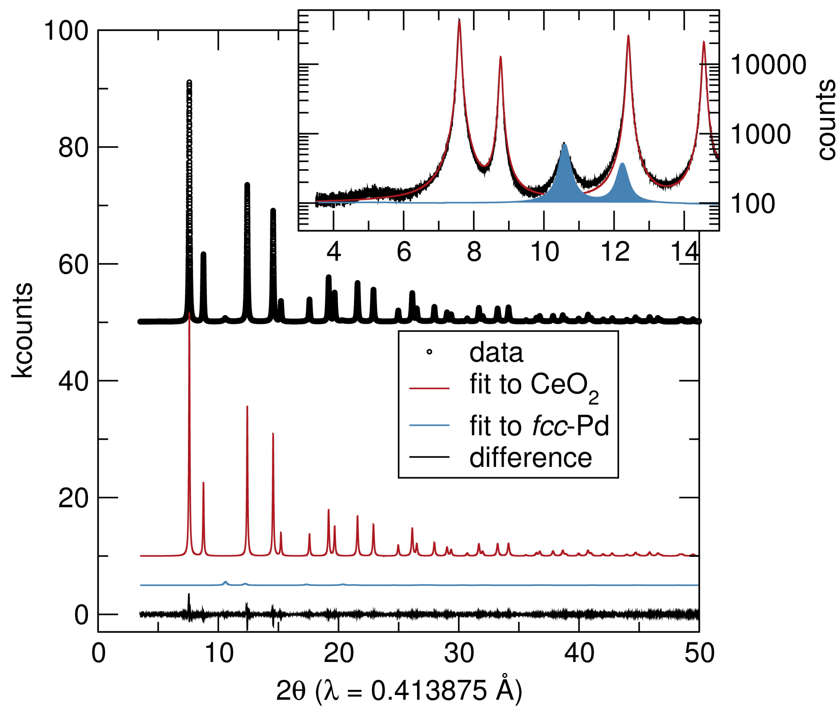

Figure 2.5: Synchrotron XRD data for$Ce_{0.95}Pd_{0.05}O_{2-\delta}$reduced in 5% H_2 in Ar at 700°C for 8 h. The Rietveld refinement shows *fcc*-Pd metal to be quantitatively present with a mole ratio of 0.05. Figure reproduced with permission from Misch *et al.*, *Chem. Mater.*, reference [29], © 2011 American Chemical Society.

dicated in Figure 2.6 are the binding energies for the Pd $3d_{5/2}$ signal in PdO (336.8 eV) and Pd metal (335.4 eV).[70] In Figure 2.6, the Pd $3d_{5/2}$ signal for $Ce_{0.95}Pd_{0.05}O_{2-\delta}$is seen at 337.4 eV, a slightly higher binding energy than that of PdO or Pd metal. The increased ionic character suggests Pd lattice substitution. This shift to higher binding energy is in agreement with the XPS of the Pd 3d region taken by Singh *et al.* for$Ce_{0.95}Pd_{0.05}O_{2-\delta}$prepared via solution combustion synthesis in which the $3d_{5/2}$ signal is seen at 337.4 eV.[71] Though this does not entirely rule out the possibility of PdO clusters on the surface, both bulk probes like diffraction and surface probes like XPS suggest ionic Pd is incorporated into the CeO_2 lattice. The purpose of this study was also to determine if amorphous PdO, undetectably by XRD, was present on the sample. Because of the low resolution of the XPS data, it would not be possible to deconvolute the two Pd^{2+} signals. However, if amorphous PdO were present, it would crystallize upon calcination.

Reactivity studies The $Ce_{1-x}Pd_xO_{2-\delta}$ series was tested for C–H bond activation in partial oxidation of CH_4 and dry reforming of CH_4. Partial oxidation was tested over pure CeO_2 as a control (Figure 2.7(a)). Even at 600°C there is no conversion of CH_4 to products of interest. Whereas the USP prepared CeO_2 was inactive, Figure 2.7 shows the Pd–substituted CeO_2 catalyst is active for CH_4 combustion.

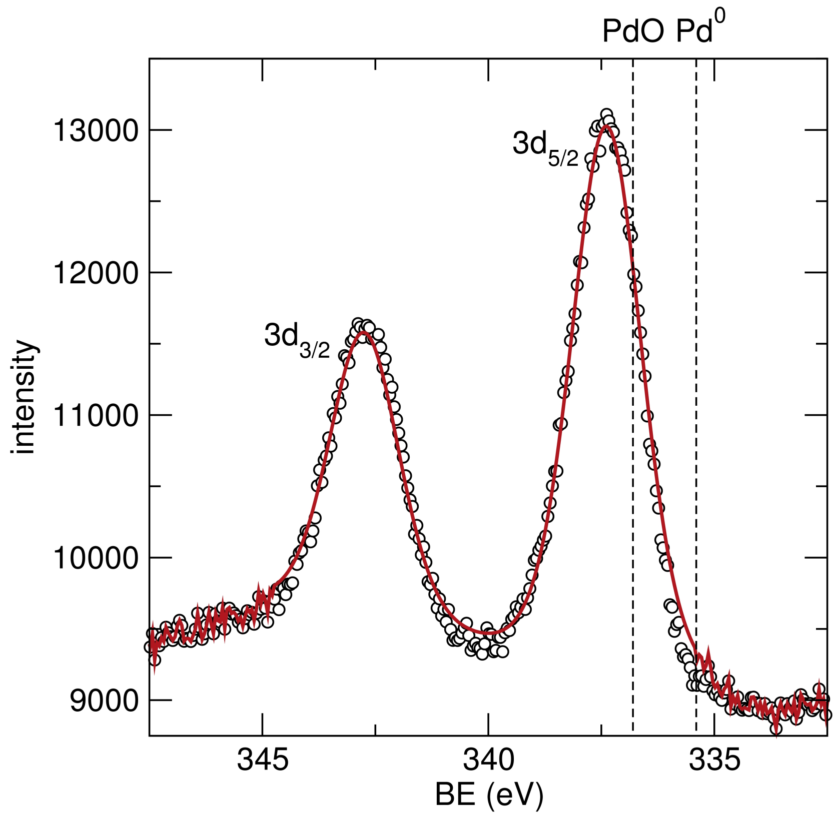

Figure 2.6: X-ray photoelectron spectrumof the Pd 3d region of as-prepared $Ce_{0.95}Pd_{0.05}O_{2-\delta}$acquired with a pass energy of 80 eV. The Pd 3d$_{5/2}$ peak is shifted to higher binding energy than found in PdO (dashed line indicates position) suggesting a more ionic charge state than that of PdO. No evidence for metallic Pd is seen. Figure reproduced with permission from Misch *et al.*, *Chem. Mater.*, reference [29], © 2011 American Chemical Society.

It was of interest to use a minimum amount of PGM while still achieving C–H bond activation. The quantitative work was performed primarily on $Ce_{0.95}Pd_{0.05}O_{2-\delta}$ which was found by us to be slightly more active than $Ce_{0.975}Pd_{0.025}O_{2\delta}$ and approximately the same as $Ce_{0.925}Pd_{0.075}O_{2\delta}$. For partial oxidation of CH_4, $Ce_{0.95}Pd_{0.05}O_{2-\delta}$ was subjected to either prereduction or preoxidation. In both pretreatment cases, the same reaction character is observed. The only difference the pretreatment yields is a slightly lower activation temperature for the prereduced sample. In partial oxidation over $Ce_{0.95}Pd_{0.05}O_{2-\delta}$(Figures 2.7(b,c)), combustion products (CO_2 and H_2O) were observed along with non-stoichiometric synthesis gas. Excess H_2 is produced from the partial oxidation of CH_4 over $Ce_{0.95}Pd_{0.05}O_{2-\delta}$.

To consider if CH_4 is reacting with CO_2 produced from combustion, dry reforming of CH_4 was tested separately. The same two pretreatments were performed individually. The pretreatment makes very little difference in the reaction character and the activation temperature of the catalyst. Very minimal synthesis gas was producing during dry reforming of CH_4 over $Ce_{0.95}Pd_{0.05}O_{2-\delta}$. Dry reforming is not the sole mechanism by which excess H_2 is produced.

To further probe the mechanism by which partial oxidation of CH_4 over $Ce_{0.95}Pd_{0.05}O_{2-\delta}$ produces excess H_2 a steady state reaction was performed. While the gas ratios for partial oxidation remained the same, the temperature

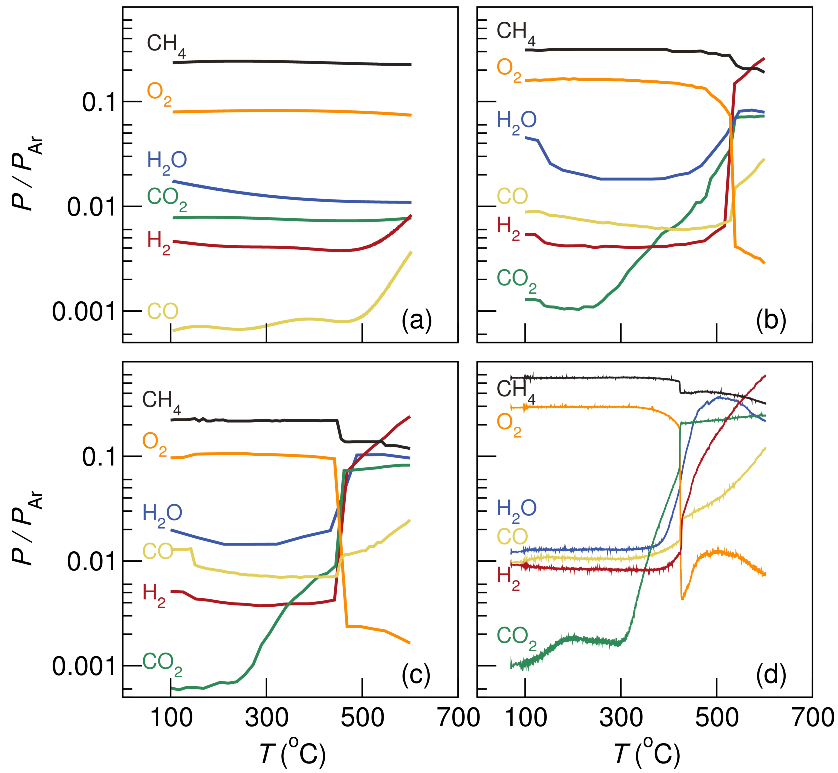

Figure 2.7: Partial oxidation of methane for (2:1 CH_4/O2) in Ar heated at 10°C/min to 600°C over (a) CeO_2, (b) preoxidized (20% O2 in Ar to 500°C 1 h) $Ce_{0.95}Pd_{0.05}O_{2-\delta}$, (c) prereduced (20% H_2 in Ar to 500°C 1 h) $Ce_{0.95}Pd_{0.05}O_{2-\delta}$, and (d) prereduced (20% H_2 in Ar to 500 C 1 h) PdO/CeO_2. Almost no reaction is observed over pure CeO_2. The substituted Pd catalyst produces combustion products and nonstoichiometric synthesis gas during partial oxidation and behaves similarly to the supported Pd catalyst under reaction conditions. Figure reproduced with permission from Misch *et al.*, *Chem. Mater.*, reference [29], © 2011 American Chemical Society.

ramp was changed to allow the catalyst to come to steady state at each temperature stage before continuing. The temperature ramping for the steady state reaction was 1 h dwells in 50°C increments starting at 400°C, increasing to 600°C, and back down again. As shown in Figure 2.8, the steady state reaction clearly shows consumption of water during partial oxidation of CH_4, suggesting steam reforming. Along with the consumption of water, more CO_2 is produced than expected. This is likely a result of the water-gas shift reaction. The excess H_2 observed during partial oxidation of CH_4 over$Ce_{0.95}Pd_{0.05}O_{2-\delta}$also likely results from a combination of some dry reforming, steam reforming, and water gas shift reactions. The long time steady state reaction for partial oxidation of methane over $Ce_{0.95}Pd_{0.05}O_{2-\delta}$was carried out for 24 h at 600°C. 2.9

To explain why prereduction causes this catalyst to become active at a slightly lower temperature than the preoxidized sample, we chose to further investigate how reducing conditions affected this material. Synchrotron powder XRD of the prereduced catalyst in Figure 2.5 distinctly shows *fcc*-Pd in addition to cubic CeO_2. It appears that Pd-substituted CeO_2 becomes Pd supported on CeO_2 under reducing conditions, and this is the catalytically active phase for CH bond activation. Pd-substituted CeO_2 is not active for CH bond activation. To confirm that the substituted material behaves like Pd metal under reaction conditions, partial oxidation was recorded for a prereduced sample of PdO sup-

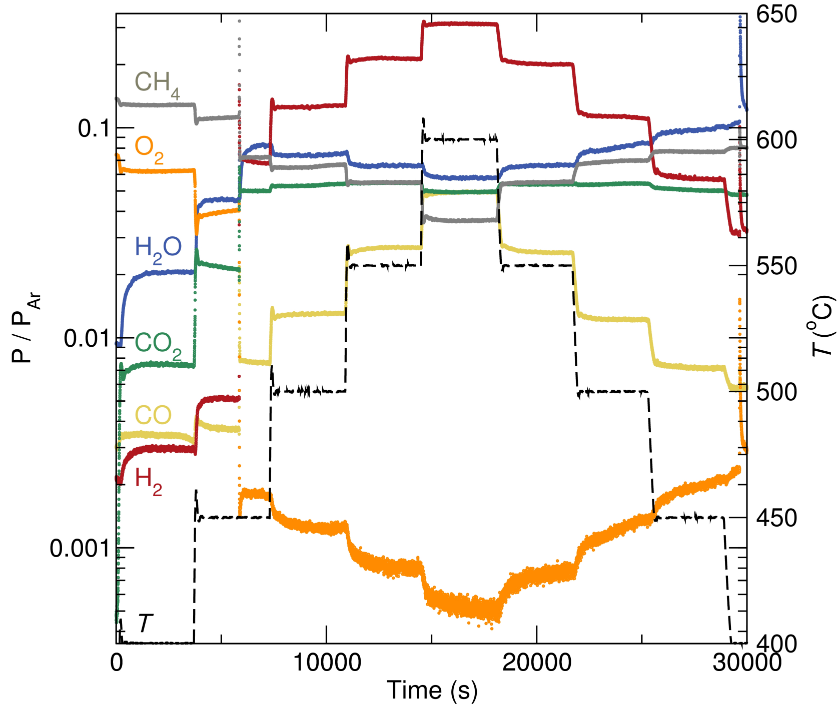

Figure 2.8: Steady state partial oxidation of methane (2:1 CH_4/O2) in Ar heated in 50°C increments from 450 to 600°C with a dwell time of 1 h at each temperature step over $Ce_{0.95}Pd_{0.05}O_{2-\delta}$. At 450°C sufficient Pd metal is present to produce nonstoichiometric synthesis gas, H_2 in excess. After combustion, several secondary reactions occur including steam reforming and water gas shift. Figure reproduced with permission from Misch *et al.*, *Chem. Mater.*, reference [29], © 2011 American Chemical Society.

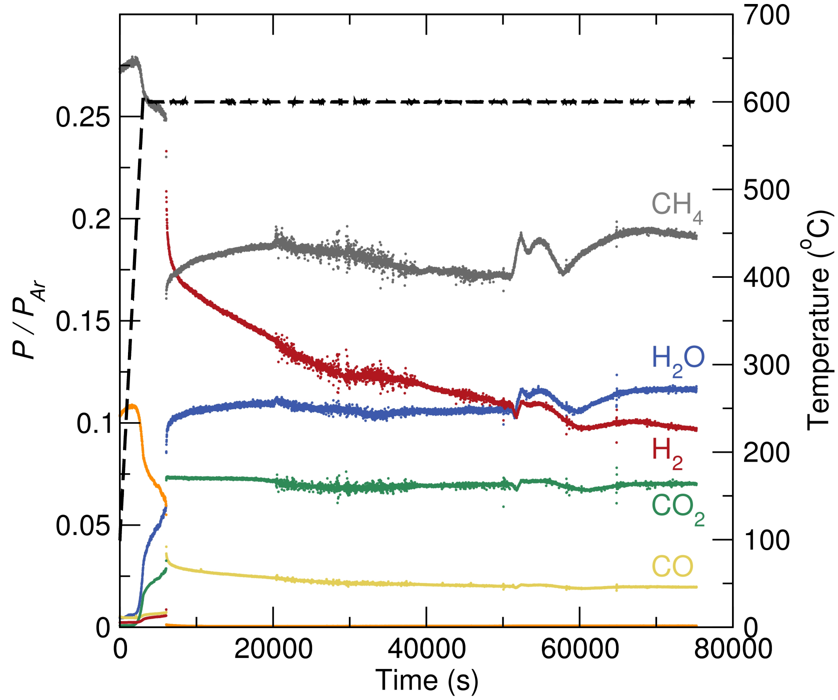

Figure 2.9: Partial oxidation of methane (2:1 CH_4/O2) in Ar heated at 10°C/min to 600°C over $Ce_{0.95}Pd_{0.05}O_{2-\delta}$. The catalyst remains active for 22 h. Figure reproduced with permission from Misch *et al.*, *Chem. Mater.*, reference [29], © 2011 American Chemical Society.

ported on CeO_2 (Figure 2.7(d)). Partial oxidation of CH_4 over Pd metal supported on CeO_2 shows identical reaction character to partial oxidation over the Pd-substituted CeO_2, but with activity for excess hydrogen production igniting at about 400°C as opposed to about 450°C in Pd-substituted CeO_2.

The reaction character observed for partial oxidation and dry reforming of methane over Pd-substituted CeO_2 is in contrast to that Pt-substituted CeO_2. Partial oxidation of methane over Pt-substituted CeO_2 does produce stoichiometric synthesis gas between 450 and 500°C, while Pd-substituted CeO_2 produces nonstoichiometric synthesis gas in the form of excess H_2. Pt–substituted CeO_2 is also active for dry reforming of methane to synthesis gas with relatively high conversion, while Pd-substituted ceria produces nonstoichiometric synthesis gas with a very low yield. Pd-substituted CeO_2 likely undergoes several secondary reactions during partial oxidation of methane, including dry reforming of methane, water-gas shift, and steam reforming of methane.

The synchrotron powder diffraction pattern was collected for postreaction $Ce_{0.95}Pd_{0.05}O_{2-\delta}$ mixed with Al_2O_3. Just as *fcc*-Pd was seen in the reduced material (Figure 2.5), so too is this phase observed in the diffraction pattern shown in Figure 2.10 along with the γ–Al_2O_3 diluent. We took special care to cool the material in an inert atmosphere after becoming active under reaction conditions. The material was also handled carefully, quickly contained, and promptly sent for characterization. We recognize that some reoxidation may take place but the*fcc*- Pd phase is very clearly seen in the postreaction material. Certainly no PdO phase is observed in the postreaction material. Moreover, the fact that the catalytic behavior matches that of Pd/CeO_2 further supports that the postreaction material does contain Pd metal. The correlation length of*fcc*-Pd determined from synchrotron XRD and the Scherrer line broadening equation is near 7 nm for postreaction $Ce_{0.95}Pd_{0.05}O_{2-\delta}$and near 100 nm for the as-prepared Pd/ CeO_2 used for comparison. However, it should be noted that the Scherrer line broadening equation does not provide the most accurate measure of coorelation length at these length scales. It seems that the catalytically active phase of $Ce_{0.95}Pd_{0.05}O_{2-\delta}$for partial oxidation of CH_4 is actually the reduced Pd supported on CeO_2. Other reactions and chemical probes were considered to determine the presence of metallic Pd in this catalyst.

It would appear that Pd-substituted CeO_2 becomes Pd supported on CeO_2 under reaction conditions. Since Pd supported on oxides is capable of catalyzing ethylene hydrogenation, we performed ethylene hydrogenation over $Ce_{0.95}Pd_{0.05}O_{2-\delta}$.[72] As seen in Figure 2.11(a), no ethane was produced over unsubstituted CeO_2. However, ethane was produced over prereduced $Ce_{0.95}Pd_{0.05}O_{2-\delta}$ at room temperature (Figure 2.11(b)). Increasing the temperature did not increase the ethylene conversion in this reaction. The same behavior

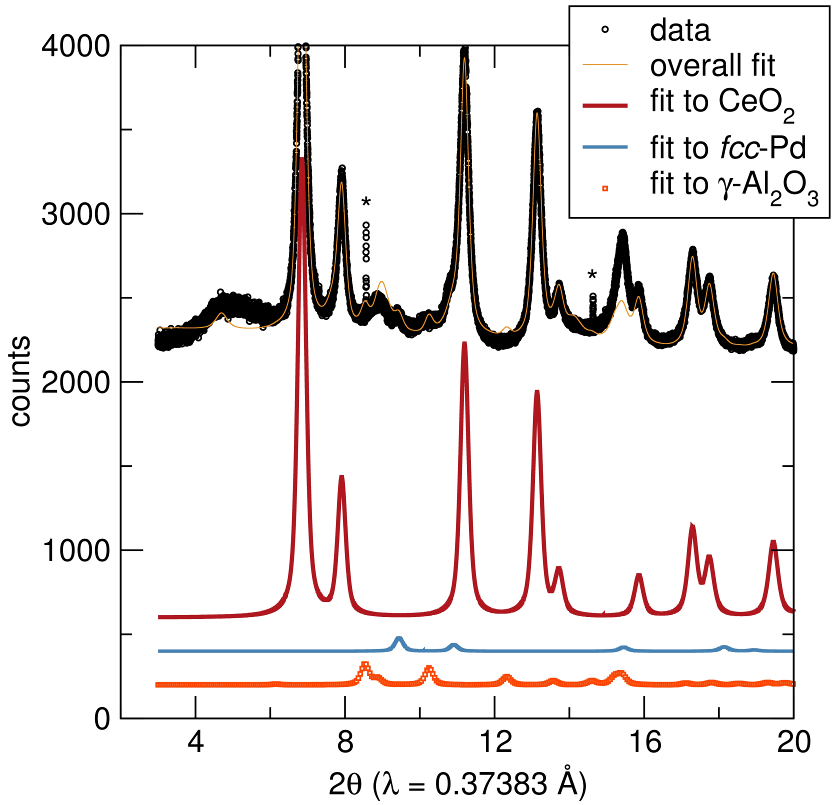

Figure 2.10: Synchrotron XRD data for $Ce_{0.95}Pd_{0.05}O_{2-\delta}$mixed with γ- Al_2O_3 after use as catalyst under partial oxidation conditions to 600°C. The Rietveld refinement shows*fcc*-Pd metal present along with diluent Al_2O_3. The asterisks indicate an unidentified impurity. Figure reproduced with permission from Misch *et al.*, *Chem. Mater.*, reference [29], © 2011 American Chemical Society.

was observed for reduced PdO/CeO_2 (Figure 2.11(c)). It is interesting to note that there appears to be a slightly higher selectivity toward ethane production for reduced $Ce_{0.95}Pd_{0.05}O_{2-\delta}$ than the reduced PdO/CeO_2 used for comparison. To confirm that this reaction proceeds over Pd metal supported on CeO_2, and not the as-prepared $Ce_{0.95}Pd_{0.05}O_{2-\delta}$, we attempted ethylene hydrogenation without a prereduction. The catalyst does not become active until it becomes sufficiently reduced by the ethylene and hydrogen flowing over the catalyst. Figure 2.12 shows that at around 110°C the catalyst was reduced to Pd metal supported on CeO_2 at which point ethylene was converted to ethane. The catalyst continued to actively produce ethane while it was cooled back to room temperature.

2.1.4 Conclusions

Pd-substituted CeO_2 catalysts have been successfully prepared via USP with a surface area of 32 m^2/g and hollow sphere morphology. These materials are phase pure up to 10 mol % Pd substitution. This material becomes catalytically active for C–H bond activation only after the Pt^{2+} ions have been reduced to Pd metal supported on CeO_2. Partial oxidation of CH_4 over $Ce_{0.95}Pd_{0.05}O_{2-\delta}$ yields the expected combustion products along with nonstiochiometric synthesis gas in the form of excess hydrogen gas. The excess hydrogen is a result of several

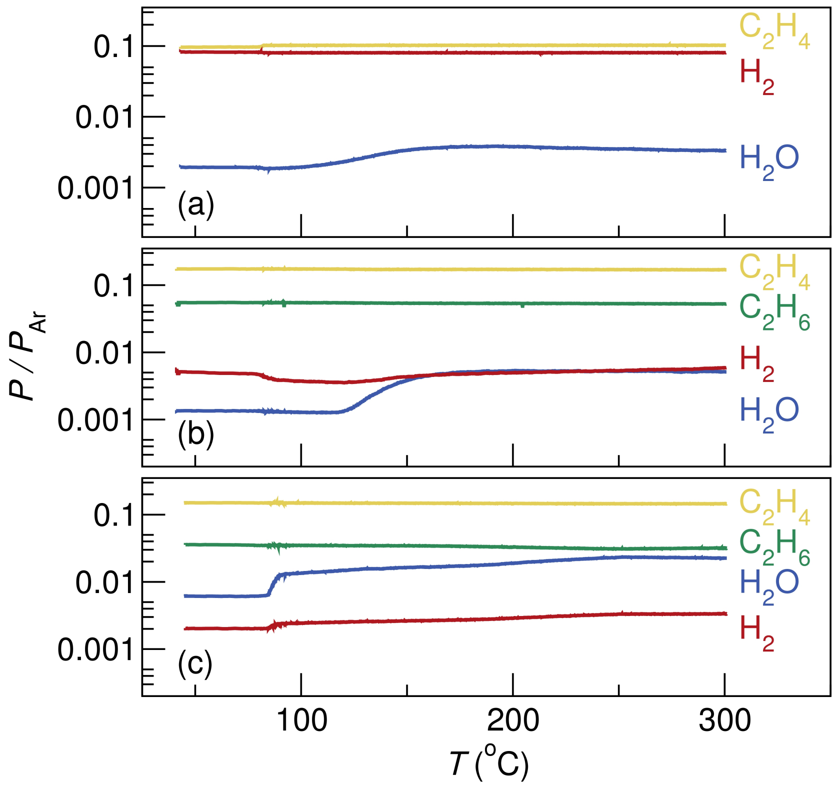

Figure 2.11: Ethylene hydrogenation (1:1 C_2H_4/H_2) in Ar heated at 10°C/min to 300°C over (a) CeO_2, (b) prereduced (20% H2 in Ar to 300°C 1 h) $Ce_{0.95}Pd_{0.05}O_{2-\delta}$, (c) prereduced (20% H2 in Ar to 300°C 1 h) PdO/CeO2. The reduced Pd substituted catalyst is active for a reaction known to take place on Pd metal and performs similarly to the supported Pd catalyst. Figure reproduced with permission from Misch *et al.*, *Chem. Mater.*, reference [29], © 2011 American Chemical Society.

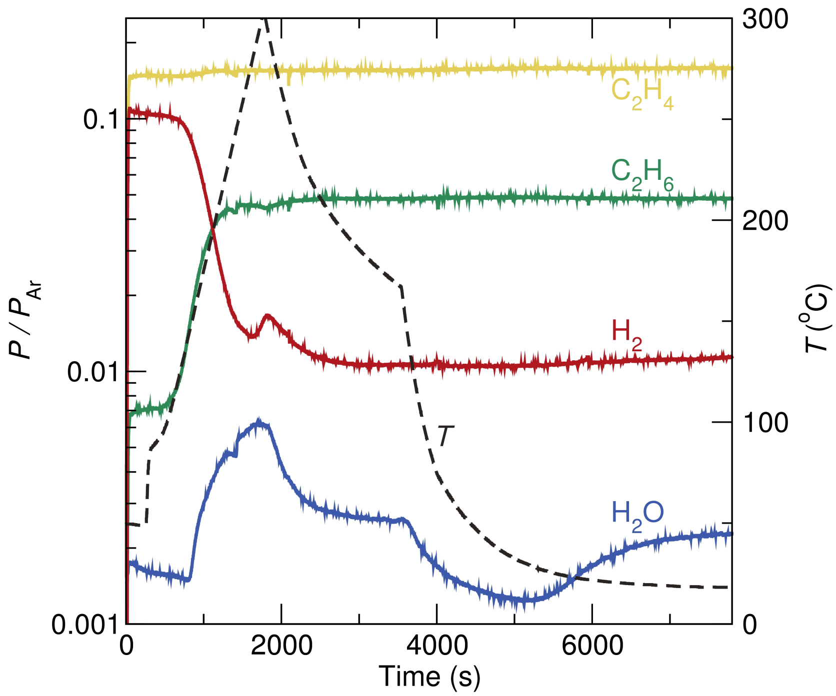

Figure 2.12: Ethylene hydrogenation (1:1 C_2H_4/H_2) over as-prepared $Ce_{0.95}Pd_{0.05}O_{2-\delta}$heated at 10°C/min to 300°C. The material becomes active and produces C_2H_6 only once the material become sufficiently reduced around 120°C, further confirming that the catalytically active form of this material is Pd supported on CeO_2. Figure reproduced with permission from Misch *et al.*, *Chem. Mater.*, reference [29], © 2011 American Chemical Society.

secondary reactions occurring after combustion, including dry reforming of CH_4, steam reforming of CH_4, and water gas shift. The catalytically active phase for this material is Pd supported on CeO_2, confirmed by the ethylene hydrogenation reaction. Additionally, we have identified USP as an adequate method for the preparation of substituted metal oxides and potentially for the preparation of well-dispersed metal nanoparticles on oxide supports upon reduction.

2.2 USP for Pd–substituted $LaFeO_3$

Pd–substitution can be achieved in other host oxides. Pd–substitution in perovskite hosts was of particular interest. Pd–substituted $LaFeO_3$ was prepared using USP with stoichiometric molar quantities of $La(NO_3)_3 \times 6H_2O$ (99.999%, Aldrich) and $Pd(NO_3)_2 \times 2H_2O$ (99.999%, Aldrich) dissolved in Millipore water. The precusor solution inside custom glassware was nebulized into a fine mist, using the modified Sunpenton humidifer, and carried through a Lindberg/BlueM tube furnace at 800°C. Product powders were collected in water bubblers and allowed to evaporate in a 100°C oven overnight.

Phase pure materials were achieved for $LaFe_{1-x}Pd_xO_{3-\delta}$ where x = 0, 0.01, 0.025, 0.05, 0.075, as shown in 2.13. There was no significant trend in lattice parameter with dopant concentration. There was no evidence for any PdO

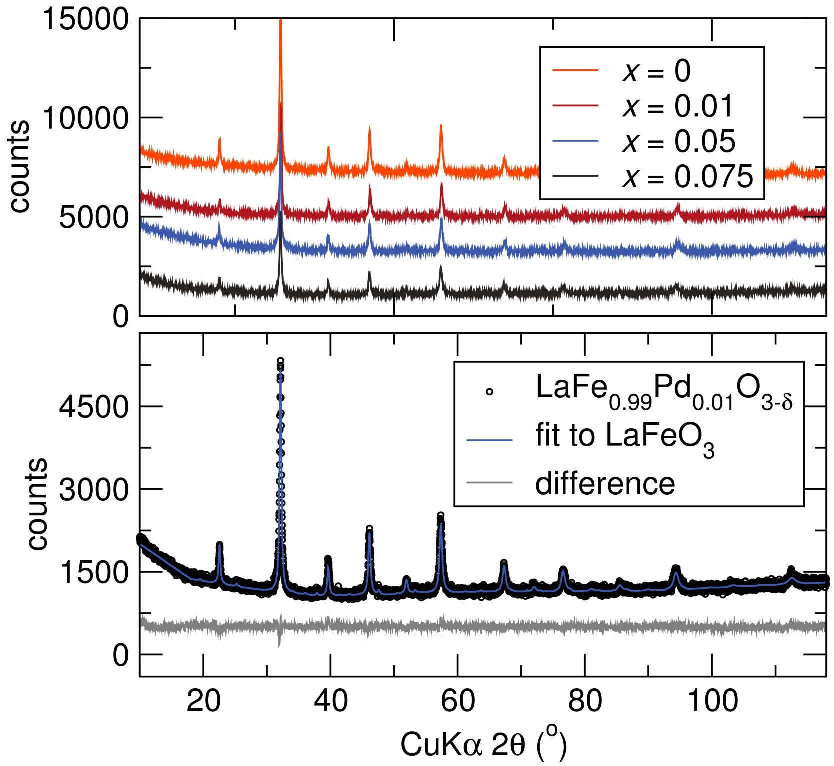

Figure 2.13: Lab X-ray diffraction data for $LaFe_{1-x}Pd_xO_{3-\delta}$. Materials are phase pure up to $x = 0.075$.

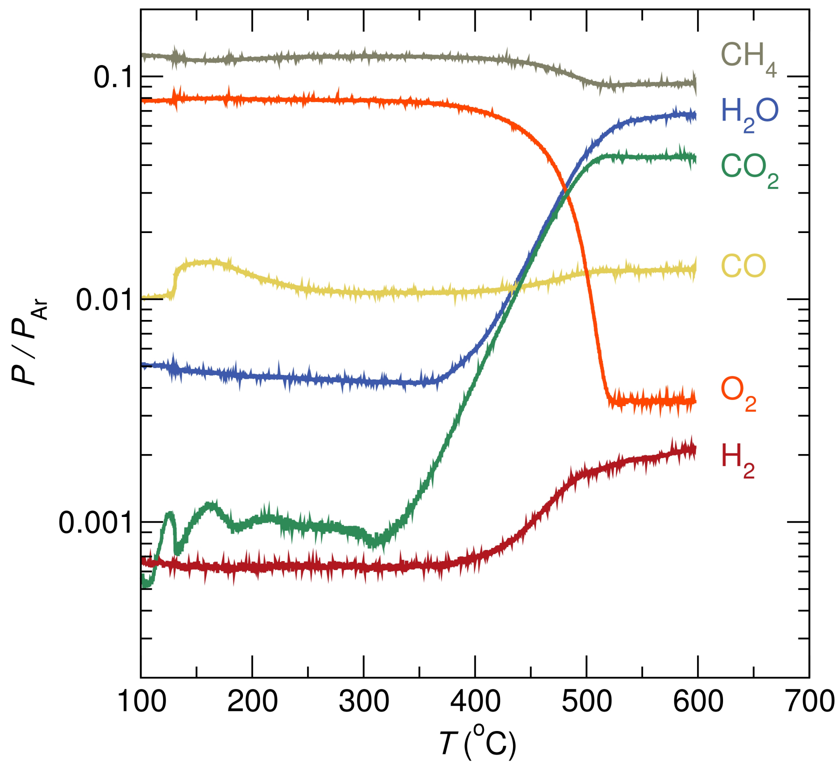

Figure 2.14: Partial oxidation of methane over 5%Pd–substituted $LaFeO_3$ (2:1 CH_4/O2) in Ar heated at 10°C/min to 600°C. Only combustion products are formed, indicating that no Pd metal is formed in this material under these reaction conditions.

or *fcc*–Pd in the USP prepared samples. X-ray photoelectron spectroscopy also revealed ionic Pd, similar to the results for Pd–substitution in CeO_2.

The true goal of Pd–substitution in a more complex oxide host was to stablize Pd ions under reducing reaction conditions, like those of partial oxidation of methane. We hypothesized that a perovskite host would allow Pd to remain ionic under parital oxidation conditions. We saw in 2.14 that the anticipated combustion products were observed, but no significant H_2 or CO was produced. This indicated that Pd was, in fact, remaining ionic under methane partial oxidation conditions. If this catalyst had produced the same product mixture as seen $Ce_{0.95}Pd_{0.05}O_{2-\delta}$, we would know that Pd metal was forming once again. Because it did not, we continued to examime this material and others in the pervoskite family in hopes of understanding how to properly stabilze Pd ions for catalytic testing.

Chapter 3

Pd–substituted perovskites for C–C coupling reactions

3.1 Pd–substituted LnFeO$_3$, Ln = Y, La

3.1.1 Introduction

Ionic noble metal catalysts continue to receive attention because they can provide means to enhanced reactivity. Substituting noble metals into oxide hosts

[1]Substantial portions of this chapter have been reproduced with permission from: L. M. Misch, A. Birkel, C. A. Figg, B. P. Fors, G. D. Stucky, C. J. Hawker, and R. Seshadri, Rapid microwave-assisted sol-gel preparation of Pd–substituted LnFeO$_3$ (Ln = Y, La): Phase formation and catalytic activity, *Dalton Trans.* **43** (2014) 2079–2087, reference [73] © 2014 Royal Society Publishing.

is an attractive alternative to supporting noble metal nanoparticles on oxides, with substitution allowing the use of very small amounts of expensive, precious metals while still accessing their reactivity for CO oxidation, NO_x reduction, and hydrocarbon conversion.[18] Hegde *et al.* have shown that Pd-substituted binary oxides are superior CO oxidation catalysts to the traditional metal nanoparticle catalyst on an oxide support.[19, 51] Recently, our group has reported that Pd-substituted CeO_2 can be used as a methane partial oxidation catalyst, and determined that CeO_2 as a host oxide is not able to maintain the stability of ionic Pd under strongly reducing reaction conditions.[29] However, it has been previously demonstrated that Pd ions can be substituted into pervoskites and stabilized in complex oxides.[8, 9, 74, 75] With this in mind, we now consider Pd-substitution in perovskite hosts.

Perovskites have been long been studied for catalytic purposes. First reports of perovskites as automotive emissions catalysts dates back to the 1970s.[76, 77] The utility of these materials lies in their ability to be reduced and subsequently re-oxidized multiple times. Structurally, the large A site, usually occupied by an alkaline earth or rare earth ion, and corner-sharing B site octahedra make the perovskite amenable to ion substitution on both cation sites. For this reason, perovskites can be prepared with various substituents, notably noble metals.[7] Although primarily studied as catalysts for CO oxidation and NO_x reduction,

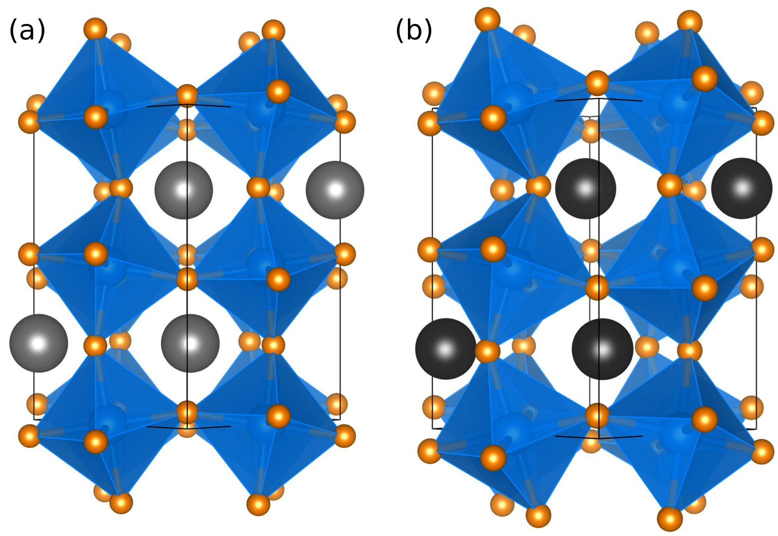

Figure 3.1: Crystal structures for (a) $LaFeO_3$ and (b) $YFeO_3$. The *A* site cations are displayed as grey spheres and FeO_6 octahedra in blue. Figure reproduced with permission from Misch *et al.*, *Dalton Trans.*, reference [73], © 2014 Royal Society Publishing.

these materials have also been considered as catalysts for coupling reactions in organic chemistry.[78] Although $LaFeO_3$ and $YFeO_3$ have a very similar crystal structures, the significant size difference of the *A* site cation results in the much smaller Y^{3+} creating significantly tilted and rotated octahedra in $YFeO_3$. This subtle difference is shown in Figure 3.1. It was of interest to understand whether these differences in the structure would result in distinct behavior.

We have prepared Pd-substituted (La,Y)FeO_3 in order to better understand the contribution of inductive effects from the A site cations and the role this plays in dopant ion stabilization. Pd compounds are of particular interest as catalysts for cross-coupling reactions (*i.e.* Suzuki-Miyaura,[4] Negishi,[79] Stille,[80] Sonogashira,[81] Buchwald-Hartwig,[82] Heck,[83] Hiyama,[84] *etc.*). More specifically, Pd-substituted perovskites have the ability to provide Pd^0 under reducing conditions, as well as to regenerate with Pd cations formedin an oxidative environment, thus providing a fully recyclable Pd source.[7, 85, 86] Previous success with Pd-perovskites as recyclable catalysts[78] in Suzuki-Miyaura reactions has further prompted our study of Pd-substituted (La,Y)FeO_3 for these reactions.[78, 87] Here we utilize the Suzuki-Miyaura reaction to compare and understand the catalytic activity of materials with various substitution levels of Pd (0, 5, 10-mol%), differing A site cations and varying surface areas, which can all be easily controlled using our rapid and facile microwave preparation method.

One very interesting approach to rapidly prepare uniform and phase pure materials is the use of microwave-assisted reactions.[88–91] Recently, it has been demonstrated that with simple modification and optimization, household microwave ovens can be employed to obtain high quality materials that enable various types of reactions, including conventional solid-state reactions to yield phosphors with high quantum yields,[25, 27] the heating of air-sensitive materials in evacuated fused silica tubes to access intermetallics for thermoelectrics[24, 28] and the use of sol-gel based preparations.[92] Along with providing stable, stoichiometric, complex compounds, the microwave preparation routes are also appropriate for preparing complex substituted oxides, in which a dopant ion resides on a metal cation site.

In the present study we report a rapid microwave-assisted combustion/sol-gel preparation as a method to produce noble metal-substituted perovskites. Unsubstituted materials as well as various synthetic pathways leading to them have been investigated previously.[8, 93–97] The specific approach followed here allows for the careful investigation of the phase formation process due to the very short and controllable heating times. We have applied the materials prepared using microwave-assisted techniques to Suzuki-Miyaura coupling reactions and determined that the substituted perovskites are actually precursor catalysts and provide a Pd source for coupling catalysis. The La containing perovskites are more active than the Y containing perovskites, and it has been established unambiguously through the use of the ligand 2-dicyclohexylphosphine-2′,6′-dimethoxybiphenyl (SPhos) that any catalytic activity does not stem from the perovskite itself, but from the reduced Pd^0 that is released and then bound by the ligand. We have demonstrated that these materials are appropriate for coupling of aryl chlorides under more mild conditions than has previously been reported.

3.1.2 Experimental methods

Sample Preparation All samples were prepared *via* a microwave-assisted reaction pathway, employing a citric acid based sol-gel reaction.[92] In a typical synthesis, to 15 mL of MilliPore water (18 MΩ·cm) and 5 mL ethanol (in a 50 mL beaker), a two-fold excess (in terms of metal cations) of citric acid was added and the solution was stirred until clear, which usually took about 5 minutes. Subsequently, the *p*H was adjusted to neutral through the addition of several drops of aqueous ammonia.

For the preparation of Ln_{1-x}Pd$_x$FeO$_{3-\delta}$ (with Ln = La, Y), stoichiometric amounts of of the metal nitrates Ln(NO$_3$)$_3$ $\cdot$ 6H$_2$O, Fe(III) acetylacetonate and Pd(II) acetylacetonate (all obtained from Sigma-Aldrich) were dissolved and the solution was vigorously stirred. After the addition of either La(NO$_3$)$_3$ $\cdot$ 6H$_2$O or Y(NO$_3$)$_3$ $\cdot$ 6H$_2$O, a milky precipitation formed. The other reagents were added after the dissolution of this precipitation.) In the case of Y$_{1-x}$Pd$_x$FeO$_{3-\delta}$, a small excess (between 5 mol-% and 10 mol-%)of Fe(III) acetylacetonate had to be used to limit the amount of Y$_2$O$_3$ impurities. The temperature of the reaction mixture was held at 65°C to slowly evaporate the solvent until a gel was formed, which usually happened between 8 h and 10 h. This gel is then dried at 125°C overnight and eventually finely ground. A batch size of about 250 mg of dried gel is then heated in a so-called hybrid microwave (Panasonic NN-SN667B, 1250 W) setup, as described in prior work.[25, 27, 98]

Many iterations with various heating profiles and power levels were attempted. The reaction time and power level were adjusted to optimize the crystallinity, phase purity, and surface area of the investigated samples. Time-dependent study of the phase formation was carried out at various reaction times, using a power setting of 100%, 1250 W. The optimized reaction time was 150 seconds at a power level setting of 70% for $La_{1-x}Pd_xFeO_{3-\delta}$ and a multi-step heating profile (2 minutes at a power setting of 90%, followed by several minutes at lower power settings) for $Y_{1-x}Pd_xFeO_{3-\delta}$. The temperature was measured in various intervals during and after the reaction was finished using a portable infrared pyrometer (PalmerWahl DHS235XEL).

Sample Characterization Laboratory powder X-ray diffraction (XRD) data were obtained using Cu Kα radiation (Philips X'Pert) over the angular range $15^\circ \leq 2\theta \leq 90^\circ$ with a step size of 0.016°. High resolution synchrotron powder diffraction data were collected using beamline 11-BM at the Advanced Photon Source (APS), Argonne National Laboratory using an average wavelength of 0.413893 Å. Discrete detectors covering an angular range from -6° to 16° 2θ were scanned over a 34° 2θ range, with data points collected every 0.001° 2θ at scan speed of 0.01°/s. Rietveld fits[99] of the data were obtained using the

TOPAS Academic program suite.[100] TGA was carried out using a METTLER TGA/sDTA851e ThermoGravimetric Analyzer in air scanning the temperature range between 25°C and 900°C at a heating rate of 10 °C per minute. X-ray photoelectron spectra were obtained on a Kratos Axis Ultra Spectrometer with monochromatic Al-Kα source (E = 1486.61 eV). Samples were mounted on a stainless steel holder using double-sided carbon tape. The residual pressure inside the sample analysis chamber was below 7×10^{-9} Torr. Survey spectra were collected with an analyzer pass energy of 80 eV and high-resolution Pd 3d spectra were acquired at a pass energy of 20 eV. Spectra were calibrated to the C 1s peak from adventitious hydrocarbons, expected at a binding energy of 285.0 eV. For peak fitting of the spin-orbit doublets in high resolution scans, the $d_{3/2}$ to $d_{5/2}$ peak area was constrained to a ratio of 2/3 with the use of CasaXPS software. Field-emission scanning electron microscopy was performed on a FEI XL40 Sirion FEG microscope with an Oxford Inca X-ray system attached for chemical analysis. SEM samples were mounted on aluminum stubs using double-sided conductive carbon tape and coated with a thin layer of Au/Pd in order to avoid charging effects. The images were recorded with an acceleration voltage of 5 kV. Energy-dispersive X-ray spectroscopy was performed on using an acceleration voltage of 20 kV. The samples were not sputtered with conductive coatings. Transmission electron microscopy was performed on a FEI Tecnai G2

Sphera Microscope with an acceleration voltage of 200 kV. TEM samples were prepared by dispersing a small amount of the powder in ethanol and subsequent ultrasonication for about 15 minutes. Then, 2 to 3 drops were administered onto copper grids (lacey carbon, Type-A, Ted Pella) and the solvent was allowed to evaporate overnight. Brunauer-Emmett-Teller (BET) surface area measurements were performed on a MicroMeritics TriStar 3000 porosimeter using N_2 as probe gas.

Catalytic Activity All reactions were carried out under an argon atmosphere. The isopropanol was purchased from Fischer Scientific and was degassed before use (three freeze-pump-thaw cycles). Aryl halides, aryl boronic acids, SPhos and potassium carbonate were purchased from Sigma-Aldrich and were used as received. All compounds were characterized by ^{1}H NMR, ^{13}C NMR, IR spectroscopy, and high-resolution mass spectrometry. Nuclear Magnetic Resonance (NMR) spectra were recorded on a Varian 600 MHz instrument. ^{1}H NMR experiments are reported in δ units, parts per million (ppm), and were measured relative to the signals for residual chloroform (7.26 ppm) in the deuterated solvent. ^{13}C NMR spectra are reported in δ units, ppm, relative to deuterochloroform (77.23 ppm) and all were obtained with ^{1}H decoupling. FT-IR spectra were obtained with a Thermo-Nicholet Avatar-330 IR spectrometer with a single-bounce attenuated total reflection (ATR) accessory with a Ge crystal. Gas chromatography (GC) analyses were performed on a Shimadzu GC-2014 instrument with a flame ionization detector (FID) using a Restek SHRXI-5MS column. High-resolution mass spectrometry was conducted with a Micromass QTOF2 Quadrupole/Time-of-Flight Tandem mass spectrometer. Flash chromatography was performed using a Biotage SP4 instrument with prepacked silica cartridges.

General procedure for a Suzuki-Miyaura reaction with different (La,Y)FeO perovskites. An oven-dried test tube, which was equipped with a magnetic stir bar and fitted with a teflon septum, was charged with SPhos (0 - 1 mol%), the perovskite (0 - 0.04 mol% Pd), phenylboronic acid (171 mg, 1.4 mmol) and K_2CO_3 (193 mg, 1.4 mmol). The vessel was evacuated and backfilled with argon (this process was repeated a total of 3 times) and then the 3-chloropyridine (95 μL, 1.0 mmol) and degassed solvent mixture (1:1 i-PrOH/H_2O, 2 mL) were added via syringe. The solution was heated to 80°C for 20 h and then cooled to room temperature, diluted with ethyl acetate (20 mL) and washed with water (5 mL). Decane was added to the solution as an internal standard and the yield was determined by GC analysis.

General procedure for a Suzuki-Miyaura reaction with $LaFe_{0.95}Pd_{0.05}O_{3-\delta}$. An oven-dried test tube, which was equipped with a magnetic stir bar and fitted with a teflon septum, was charged with SPhos (4.1 mg, 1 mol%), $LaFe_{0.95}Pd_{0.05}O_{3-\delta}$ (2 mg, 0.04 mol% Pd), arylboronic acid (1.4 mmol) and K_2CO_3 (193 mg, 1.4 mmol). The vessel was evacuated and backfilled with argon (this process was repeated a total of 3 times) and then the aryl halide (1.0 mmol) and degassed solvent mixture (1:1 i-PrOH/H_2O, 2 mL) were added via syringe. The solution was heated to 80°C for 20 h and then was cooled to room temperature, diluted with ethyl acetate (20 mL), washed with water (5 mL) and concentrated *in vacuo*. The crude product was purified using a Biotage SP4 flash purification system.

3.1.3 Results and Discussion

Evolution of perovskite products

Thermogravimetric analysis including differential thermal analysis of (La,Y)$Fe_{0.95}Pd_{0.05}O_{3-\delta}$ gels was conducted after the drying step at 125° and before the sample was subjected to any microwave heating. This offers insight into product formation during the microwave heating steps with two significant heat losses being observed during the TGA analysis. The first occurs between room temperature and 200°C, when the samples loses about 10% of their respective masses, due to evaporation of re-adsorbed water and surface hydroxyl groups as well as thermal decomposition of ammonium nitrate. The second major weight loss occurs in the temperature range between 200°C and 400-500°C. Here, the samples lose another 70% of their mass. As described in the experimental section, the gels contain an two-fold excess (in terms of total metal cations) of citric acid which combusts at temperatures exceeding 200°C. The DTA for both samples indicates two sharp exothermic events at this temperature. The combustion process is completed at about 500°C, and only a small weight loss after 500°C is observed, which is mostly due to the burning of residual organics. Our findings agree well with the results found by Qi *et al*[95], who prepared $LaFeO_3$ using combustion synthesis. Conventional solid-state preparation of these materials, usually starts from a mixture of oxides, generally requires temperatures of 1000°C and above, involves multiple regrinding steps in between multi-day heatings and yields very low surface area products. Even most sol-gel based preparation methods require several hours of heating at temperatures well above 500°C, proving again the time- and energy-saving nature of this microwave-assisted reaction pathway.

Taking advantage of the short heating and reaction times, the microwave-assisted sol-gel (or combustion) preparation allows us to study the phase formation process of the perovskites in more detail. It should be noted that although the microwave heating times are very short, the sol-gel preparation that pre-

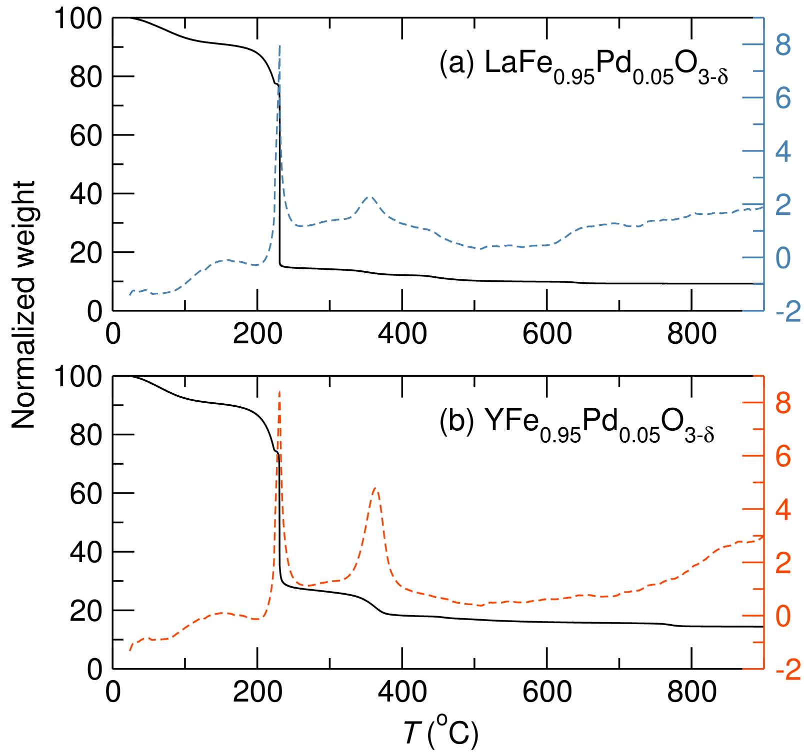

Figure 3.2: Thermogravmetric analysis of the decomposition of the dried precursor gels. Panel (a) shows the decomposition for $LaFe_{0.95}Pd_{0.05}O_{3-\delta}$ and (b) shows $YFe_{0.95}Pd_{0.05}O_{3-\delta}$. A 10% mass loss is observed between room temperature and 200°C which can be attributed to water and surface hydroxyls while a much larger weight loss is observed between 200°C and 500°C as a result of the citric acid combustion and burning of residual organics. Figure reproduced with permission from Misch *et al.*, *Dalton Trans.*, reference [73], © 2014 Royal Society Publishing.

ceeds microwave heating is completed over the course of two full days. The shortened heating time allowed by the microwave does significantly reduce the total time usually required of a sol-gel preparation, in which the final heating step may take up to several hours or days. The microwave-assisted heating method can be applied to a more conventional solid-state preparation in which precursor oxides can be ground with mortar and pestle in a matter of minutes followed by very short microwave heating times. We chose to pursue to sol-gel preparation because we were able to acheive more phase pure samples and higher surface areas than with the ceramic preparation.

Here we make use of the short heating and cooling times facilitated by the microwave and we focus on the evolution of reactants in the formation of $LaFe_{0.95}Pd_{0.05}O_{3-\delta}$. Figure 3.3 shows the laboratory X-ray diffraction data of different stages of the reaction, starting from the dried gel until 2 minutes, with 30 second steps. In both, the dried gel before subjecting to microwave radiation as well as the sample being subjected to microwave radiation for 30 s (a temperature of about 250°C was measured after that time with fume/smoke starting to evolve from the specimen), weak reflections of NH_4NO_3 can be found. These originate from the reaction of the nitrate precursor with the aqueous ammonia solution used to adjust the *p*H of the precursor solution.

After 60 s of microwave irradiation (and a temperature of 475°C), the

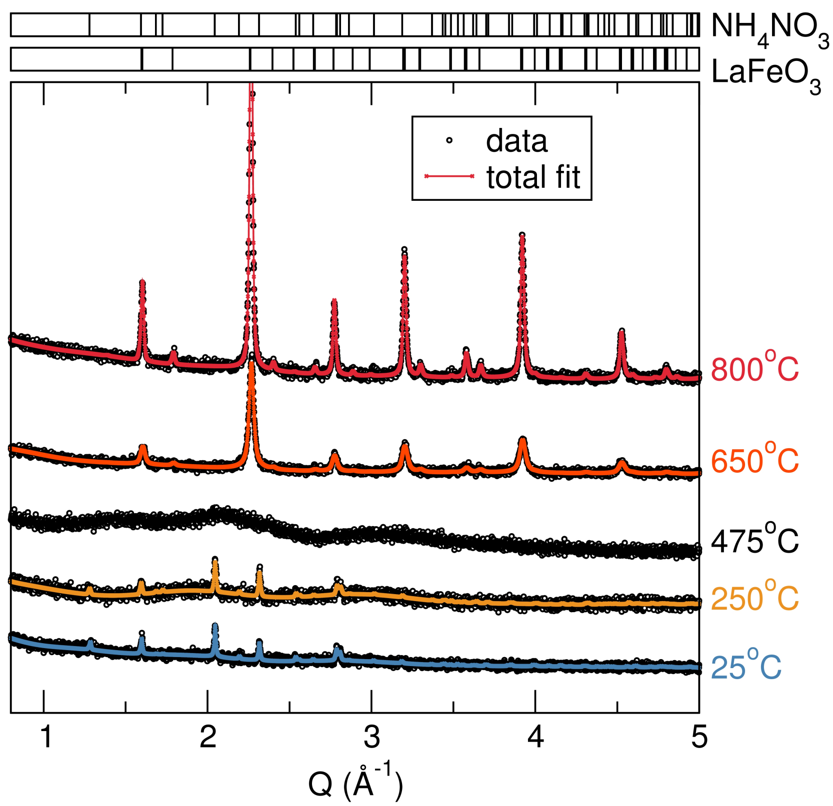

Figure 3.3: Phase evolution of LaFe$_{0.95}$Pd$_{0.05}$O$_{3-\delta}$ after 30 s intervals of the reaction, using laboratory X-ray powder diffraction data. The indicated temperatures were measured using the infrared pyrometer, aimed at the center of the inner crucible, immediately after the microwave irradiation has stopped. Formation begins after 650°C and becomes more crystalline at higher temperatures. Figure reproduced with permission from Misch *et al.*, *Dalton Trans.*, reference [73], © 2014 Royal Society Publishing.

NH_4NO_3 decomposed. Also, the sample's color changed from light brown to black with the evolution of additional smoke. At this point of the reaction, the X-ray data showed only an amorphous material, consisting of the citrate complexes of the dissolved precursors. After another 30 seconds (90 s total heating time), a temperature of about 650°C was reached and the X-ray diffraction data showed that the phase formation is completed, as only reflections of $LaFe_{0.95}Pd_{0.05}O_{3-\delta}$ are visible in the trace. These reflections are very broad and rather low intensity, pointing towards the fact that small crystallites have been formed. Crystallite size analysis using TOPAS Academic showed an average size of about 30 nm. At this point, the sample body color changed from black to a brown and the sample exhibited some fluffiness. Further heating increases the temperature to about 800°C, leading to a larger crystallite size (about 75 nm) and therefore sharper reflections. These findings correspond very well with the thermal decomposition behavior observed from the TGA data.

Laboratory and synchrotron X-ray powder diffraction data were collected to confirm the phase purity of all investigated materials. Rietveld fits of high-resolution synchrotron powder X-ray diffraction data collected at beam line 11-BM confirm that especially the substituted $YFeO_3$ samples contain at least some detectable, crystalline metallic palladium (Pd^0), as summarized in Figure 3.4. Although the amount estimated from a quantitative Rietveld fit does not exceed

2.5%, it is worth considering this when interpreting results catalytic reactivity results. In addition, LaO(OH) can be found in small quantities (less than 5-wt%) as a secondary phase in the $LaFe_{0.9}Pd_{0.1}O_{3-\delta}$ perovskites. We did observe some small changes in lattice parameter with various levels of Pd–substitution. However, no significant trend, such as a steady increase or decrease in the cell lengths as a function of increasing Pd content, was observed. This is not entirely unexpected, as this is a aliovalent substitution. As Pd^{2+} substitutes onto a 3+ site, an oxygen vacancy is subsequently created for neutrality. This was observed previously with Pd–substitution in $YFeO_3$.[8]

Scanning electron micrographs, as presented in Figure 3.5, for typical 5% Pd-substituted $LaFeO_3$ and $YFeO_3$ samples show that both substituted materials exhibit very similar morphologies. Near spherical particles that are 100 nm and smaller in size were observed and these agglomerate to form larger chunks. The micrographs shown here are representative of all perovskite materials prepared using the optimized heating profile, detailed in the experimental section. Surface area is a critical parameter for materials for catalytic applications. High surface area materials allow access to many active sites at once and are more efficient catalytic conversion of reactants to products than the same materials having lower surface area. With this in mind, the microwave heating profiles were adjusted through duration and power level to ensure that the materials

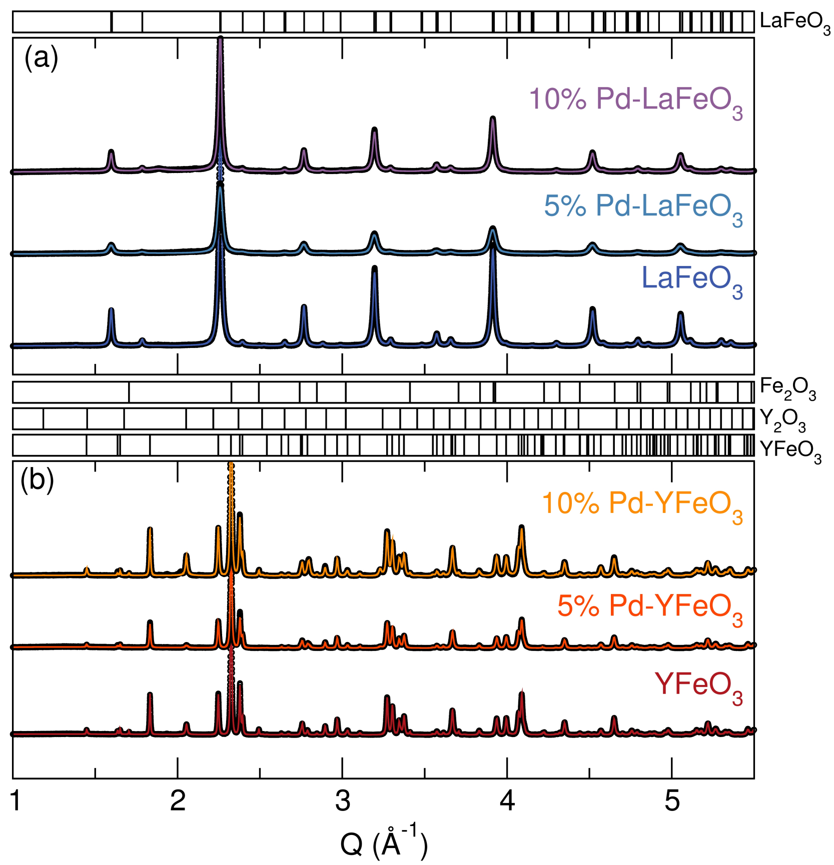

Figure 3.4: Synchrotron X-ray powder diffraction data of (a) $LaFe_{1-x}Pd_xO_{3-\delta}$ and (b) $YFe_{1-x}Pd_xO_{3-\delta}$ with various amounts of Pd substituted into the host (various x values). Figure reproduced with permission from Misch *et al.*, *Dalton Trans.*, reference [73], © 2014 Royal Society Publishing.

possessed the highest attainable surface area with this method. Materials that were heated for longer times and at higher power levels were subjected to sintering and showed fewer small particles and more large chunks. This phenomenon is directly related to surface area. Energy dispersive X-ray spectroscopy and mapping (shown in the supplemental information) confirmed increasing Pd content with Pd concentration during preparation and a homogeneous dispersion of Pd ions in as-prepared materials. Upon closer inspection with transmission electron microscopy, crystallinity anticipated from the X-ray diffraction data was observed. Similar to observations with the scanning electron micrographs, materials subjected to more strenuous heating profiles were not comprised of small enough particles to observe uniform crystallinity in the TEM.

With many iterations of various microwave heating profiles, intermittent XRD analysis, and the TGA result in mind that we were able to achieve phase-pure, crystalline materials, with surface areas near 25 m^2/g for $LaFeO_3$ materials and near 5 m^2/g for the $YFeO_3$ materials. The sol-gel microwave-assisted preparation method for substituted oxide catalysts has proven to produce superior materials in an extremely time-efficient manner compared to traditional solid-state methods. Due to different heating profiles required for La and Y containing oxides, their surface areas differ slightly. The lower surface area that is achieved for the Y analogue is attributed to the longer reaction time required to achieve

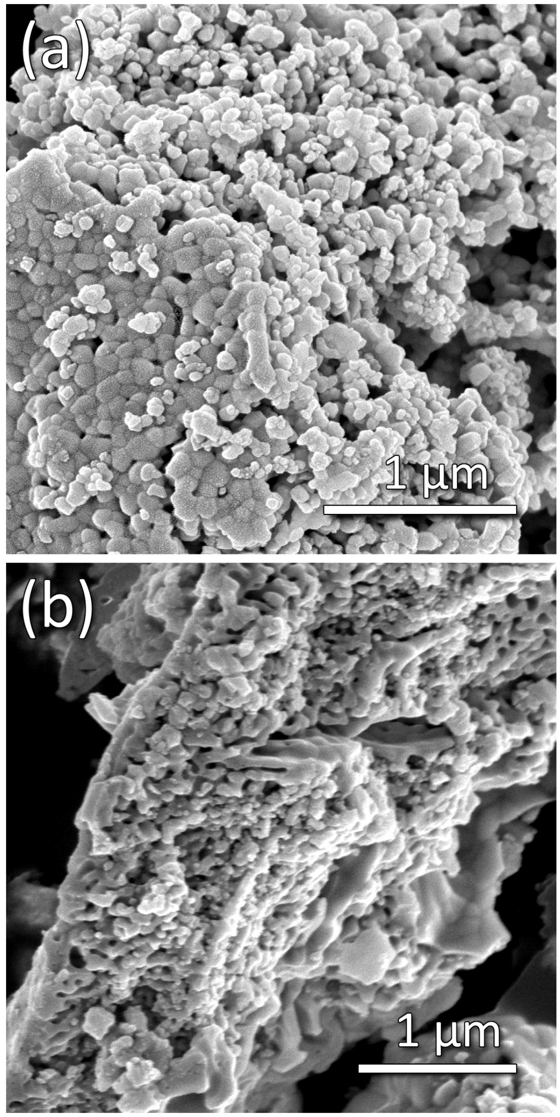

Figure 3.5: Scanning electron micrographs of (a) $LaFe_{0.95}Pd_{0.05}O_{3-\delta}$ and(b) $YFe_{0.95}Pd_{0.05}O_{3-\delta}$. Representative samples prepared using the optimized heating profiles show 100 nm crystallites agglomerated together. Figure reproduced with permission from Misch *et al.*, *Dalton Trans.*, reference [73], © 2014 Royal Society Publishing.

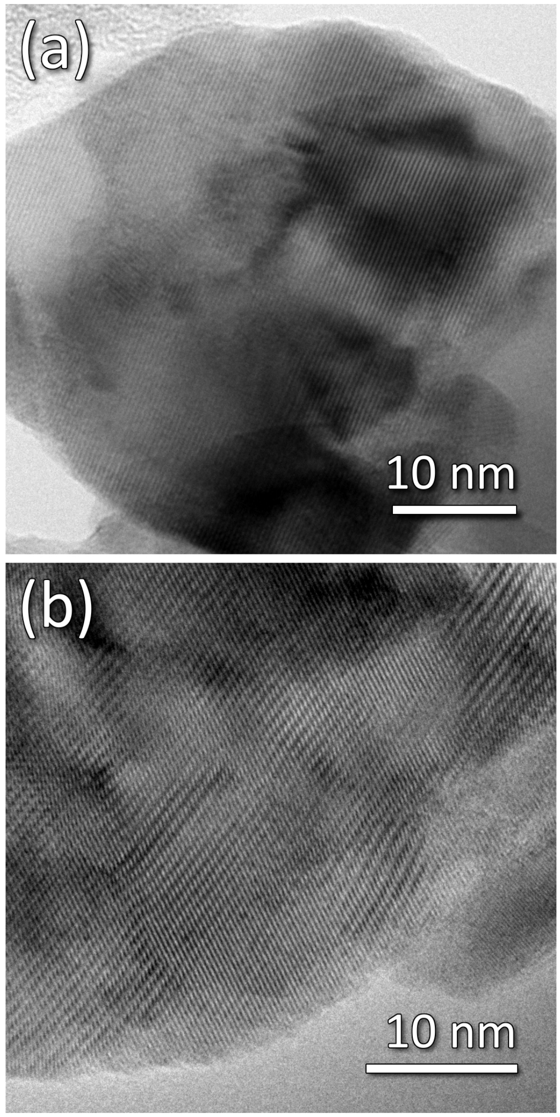

Figure 3.6: Transmission electron micrographs of (a) $LaFe_{0.95}Pd_{0.05}O_{3-\delta}$ and (b) $YFe_{0.95}Pd_{0.05}O_{3-\delta}$ show uniform crystallinity. Figure reproduced with permission from Misch *et al.*, *Dalton Trans.*, reference [73], © 2014 Royal Society Publishing.

phase purity. Though these surface areas are less than those of high surface area microporous catalysts, such as zeolitic materials, a 20-fold increase in surface area (in the La perovskite) over conventionally prepared solid-state materials is appreciable and suggests that this microwave-assisted method may be amenable to further modification for surface area enhancement.

X-ray photoelectron survey spectra and high-resolution spectra for the Pd 3d region were collected over the range of 1000 eV to 0 eV and 350 eV to 330 eV, respectively. Survey scans did not show evidence for any elements aside from the anticipated La/Y, Fe, Pd, O, and C. Quantification of the survey scans using CasaXPS software indicated that materials expected to contain 10% Pd were closer to 8% Pd, along with 51% La and 40% Fe. Materials expected to contain 5% Pd were shown to contain 5% Pd with 52% La and 43% Fe. It is expected that there is some inherent error in quantifying the survey spectra as peak areas and background type are selected manually within the software. High-resolution scans of the Pd 3d region shown in Figure 3.7 indicate that the Pd 3d peaks are shifted to slightly higher binding energy than the expected position for Pd^{2+} in PdO, 336.8 eV for the $3d_{5/2}$ peak, and Pd^0 in which the $3d_{5/2}$ appears at 335.4 eV.[70] This suggests that Pd is in a very ionic environment, more so than if PdO domains were forming along with the perovskite host.

It is clear that Pd substituted into $LaFeO_3$ is different than Pd substituted into $YFeO_3$. In the case of La as the A-site cation, we see two distinct Pd species. This is in contrast to the single Pd species observed when Y is on the A-site. This anomaly may be a result of differing inductive contributions from La and Y or Pd occupying more than one site in the case of La. The difference in catalytic behavior, discussed below, may be a result of the difference in Pd occupation in the two perovskites. We hypothesize that the La perovskite may make the Pd more accessible for catalysis and cycling to metallic Pd, while the Pd in the Y perovskite may be less accessible. This may explain the difference in catalytic reactivity for the two perovskites, as the difference in surface area is not significant enough to cause a noticeable effect. One future application for this work is to probe ionic Pd catalysis, which requires the preparation of materials that stabilize ionic Pd under various reaction conditions. It was shown in our previous work[29] that a binary oxide like CeO_2 is not a sufficient ion stabilizing host to maintain Pd ions under reducing reaction conditions. Here we show that Pd ions substituted onto the B-site of a perovskite host may experience increased ion stabilization as a result of A-site cation induction. The fact that dopant ionicity is affected by differing A-site cations further advances this stabilizing host oxide concept.

Catalytic Activity

The Suzuki-Miyaura coupling was chosen as a model reaction to demonstrate

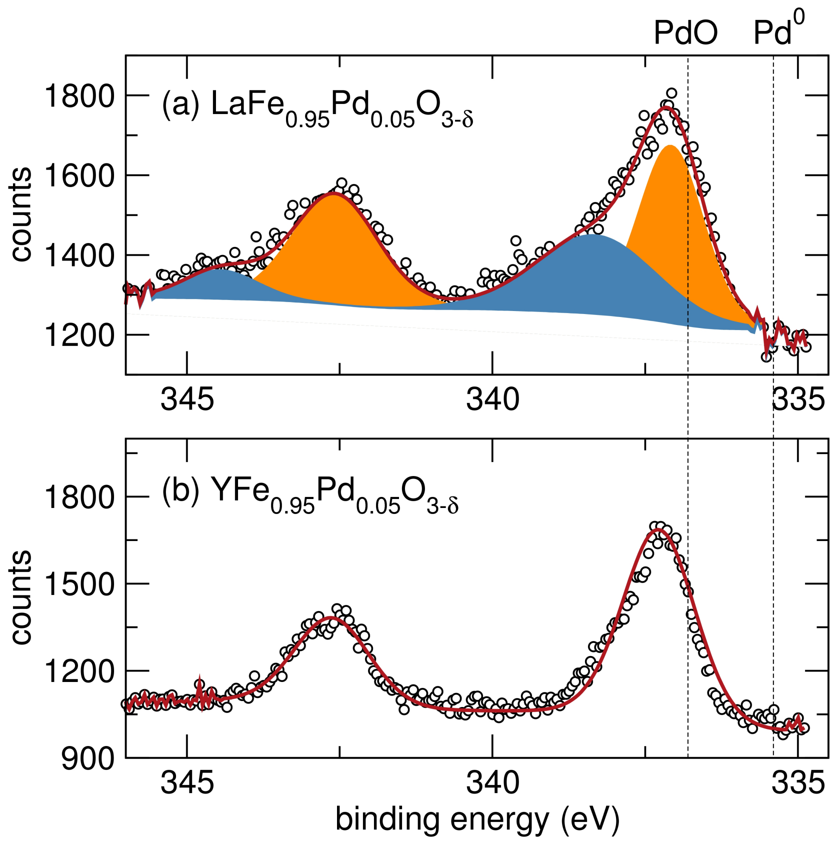

Figure 3.7: X-ray photoelectron spectroscopy data of (a) $LaFe_{0.95}Pd_{0.05}O_{3-\delta}$ and (b) $YFe_{0.95}Pd_{0.05}O_{3-\delta}$. There are two contributions observed in the case of the La perovskite and only one contribution observed for the Y perovskite. Both materials show the Pd 3d peaks shifted to higher binding energy than metallic Pd or PdO. Dashed reference lines are taken from [70]. Figure reproduced with permission from Misch *et al.*, *Dalton Trans.*, reference [73], © 2014 Royal Society Publishing.

the potential of Pd-substituted (La,Y)FeO_3 perovskites as catalyst precursors in cross-coupling reactions. Of equal importance, this reaction was selected to understand the effects of Pd-substitution levels, contribution of the A-site cation and particle surface area of our microwave synthesized perovskites on the catalytic activity of these systems.

Recently, Martin and coworkers demonstrated that Pd-containing perovskites are suitable catalysts for Suzuki-Miyaura reactions.[78, 87] They elegantly demonstrated that under their reaction conditions, Pd species desorb from the perovskite to give a soluble active catalyst. However, aryl and heteroaryl chlorides were poor substrates using this method, requiring harsh reaction conditions (*i.e.* 135°C) and resulting in modest yields. Currently, the most general catalyst systems for coupling these difficult substrates are based on discrete phosphine ligated Pd^0 complexes.[4] In order to demonstrate that perovskites can be general catalysts for cross-coupling reactions, we set out to develop a method that would efficiently couple aryl and heteroaryl chlorides under mild conditions.

We commence with the reaction of a heteroaryl chloride with an aryl boronic acid using $LaFe_{0.95}Pd_{0.05}O_{3-\delta}$ as the catalyst. We hypothesized that by adding a biarylphosphine ligand developed by Buchwald for Suzuki-Miyaura couplings, SPhos,[101] to the reaction mixture, the Pd^0 species would be ligated as it is desorbed from the perovskite, leading to the formation of a highly active catalyst. In support of this, using $LaFe_{0.95}Pd_{0.05}O_{3-\delta}$ (0.04 mol% Pd), SPhos (1 mol%), and K_2CO_3 in i-PrOH/H_2O at 80°C, 3-chloropyridine was reacted with phenylboronic acid to give the desired biaryl product in 93% yield (Table 3.1, entry 2). Interestingly, removing SPhos from this same reaction gave no product, demonstrating that the ligand is playing a critical role in the reaction and suggesting that the Pd^0 is indeed being ligated as it is desorbed from the $LaFe_{0.95}Pd_{0.05}O_{3-\delta}$.

We next investigated the impact of surface area, Pd-substitution levels, as well as the contribution of the A-site cation in the perovskite on the catalyst activity for this system. Reducing the surface area of the particles from 28.5 m^2/g to 3.4 m^2/g led to a decrease in yield from 93% to 50% (Table 3.1, entry 3); this result suggests that surface area has some influence on catalysis for this system. We hypothesize that the increased surface area enables more efficient desorption of the Pd from the perovskite leading to higher concentrations of active catalyst. Further, increasing the Pd-substitution from 5% to 10% in these materials substantially decreased the yield to 23% (Table 3.1, entry 4). This trend is similar to what was observed for Pd-substituted in CeO_2, where 5% Pd-substitution is more active than 2.5% Pd and 7.5%Pd substitution.[29] Moreover, using a material with no Pd-substitution, $LaFeO_3$, provided no desired product (Table 3.1, entry 1), confirming that Pd is responsible for catalysis. Lastly, substituting La

Table 3.1: Impact of the perovskite surface area, Pd-substitution levels and A-site cation identity in Suzuki-Miyaura cross-coupling reactions.

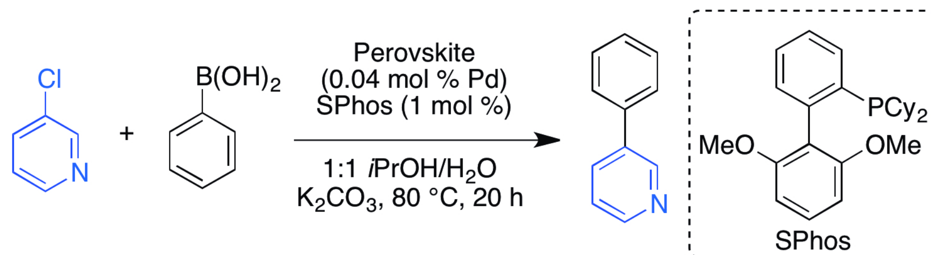

Entry	Perovskite	Surface Area (m^2/g)	GC Yield (%)
1	$LaFeO_3$ *	$\approx$ 15	0
2	$LaFe_{0.95}Pd_{0.05}O_{3-\delta}$	$\approx$ 25	93
3	$LaFe_{0.95}Pd_{0.05}O_{3-\delta}$	<5	50
4	$LaFe_{0.90}Pd_{0.10}O_{3-\delta}$	$\approx$ 15	23
5	$YFeO_3$ *	$\approx$ 10	0
6	$YFe_{0.95}Pd_{0.05}O_{3-\delta}$	<5	8
7	$YFe_{0.90}Pd_{0.10}O_{3-\delta}$	<5	0

Reaction conditions: perovskite (0.04 mol% Pd), SPhos (0 to 1 mol%), 3-chloropyridine (1.0 mmol), phenylboronic acid (1.4 mmol), K_2CO_3 (1.4 mmol), 1:1 i-PrOH/H_2O (2 mL), 80°C for 20 h.

There was no yield for reactions in which the ligand (SPhos) was omitted. *For perovskites with 0% Pd substitution the same mass was used in the reaction as the materials with 5% substitution.

for Y in these materials caused nearly complete loss in activity (Table 3.1, entries 6 - 8). We postulate that the differing A-site cation will contribute a varying inductive effect in the perovskite, influencing the stability of the Pd ions in the material, as well as the rate of desorption under reducing conditions.

The scope of this process was further examined utilizing the high surface area $LaFe_{0.95}Pd_{0.05}O_{3-\delta}$ as the Pd source and SPhos as a supporting ligand (Figure 3.8). Employing only 0.04 mol% Pd, heteroaryl chlorides and bromides were coupled with aryl boronic acids in good to excellent yields (Figure 3.8, a - d). Moreover, heteroarylboronic acids proved to be proficient coupling partners under these conditions. For example, 2-thienylboronic acid was reacted with 2-bromopyridine to give the desired product in 78% isolated yield (Figure 3.8). Aryl chlorides that did not contain any heteroatoms proved to be acceptable substrates under these conditions (Figure 3.8, e - g); however, they resulted in moderately decreased yields compared to heteroaryl chlorides. The above results clearly demonstrate that Pd-containing $LaFeO_3$ perovskites can be effective Pd sources in challenging cross-coupling reactions and can provide general and efficient catalytic activity when used in combination with supporting ligands. We envisage this strategy will be applicable to a wide range of processes and has the potential to afford highly active, long-lived and recyclable catalysts.

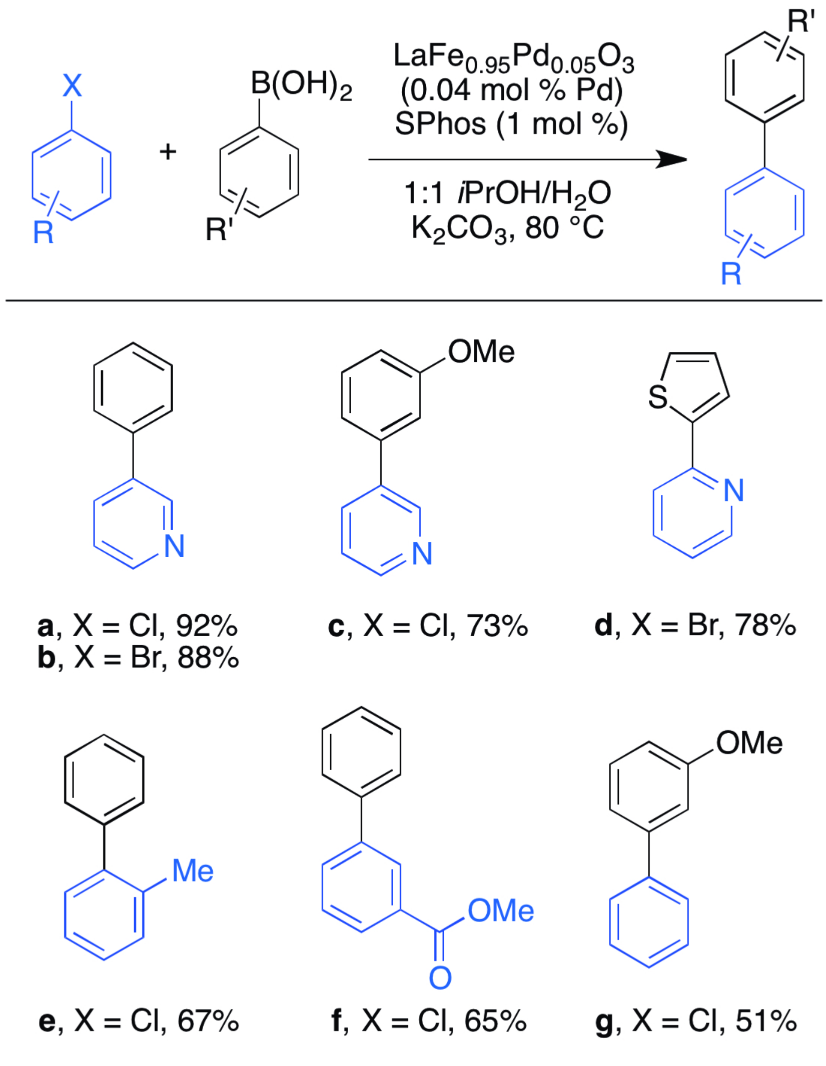

Figure 3.8: Substrate scope for Suzuki-Miyaura cross-coupling reactions using $LaFe_{0.95}Pd_{0.05}O_3$ as the Pd source (isolated yields). Figure reproduced with permission from Misch *et al.*, *Dalton Trans.*, reference [73], © 2014 Royal Society Publishing.

3.1.4 Conclusions

A rapid microwave-assisted sol-gel preparation method yields Pd-substituted perovskite materials $Ln_{1-x}\text{Pd}_x\text{FeO}_{3-\delta}$ (with Ln = La, Y). The very short heating times in microwave reactions help us elucidated the phase formation process and have shown that the reaction for forming LaFeO_3 is completed after 90 s. In contrast to furnace-based sol-gel or combustion methods, the microwave heating method has allowed the easy and reproducible tuning of material parameters such as crystallite size and surface area. Using a combination of characterization methods, we have shown that materials prepared with this method are phase pure and contain well-dispersed ionic Pd. We have also shown that changing the A site cation affects the structure and properties of the perovskite hosts. The applicability of the prepared perovskites as Pd^0 catalyst sources in Suzuki cross-coupling reactions has been demonstrated for aryl chlorides. This method is amenable to further tuning of the reaction parameters and may allow for the preparation of materials with even higher surface areas, thereby impacting their properties.

Chapter 4

Noble metal complex oxide catalysts

4.1 La_2BaPdO_5 and La_2BaPtO_5

4.1.1 Introduction

Noble metal catalysts are widely used in many types of important reactions, ranging from automotive emissions control[22] to coupling reactions.[73]

[1] Substantial portions of this chapter have been reproduced with permission from: L. M. Misch, J. Brgoch, A. Birkel, T. E. Mates, G. D. Stucky, and R. Seshadri, Rapid microwave preparation, and *ab-initio* studies of the stable complex noble metal oxides La_2BaPdO_5 and La_2BaPtO_5, *Inorg. Chem.* **53** (2014) 2628–2634, reference [102] © 2014 American Chemical Society.

These catalysts frequently comprise of noble metal nanoparticles on high surface area supports. More recently, it has been demonstrated that noble metals in their ionic forms also exhibit some catalytic reactivity, sometimes with better performance than their metallic analogs.[18] Cation substituted materials, notably Pd-substituted perovskites[7–9, 35], have received considerable attention for their cost-effectiveness and utility. However, substituted materials can be challenging to prepare and are unstable under reducing reaction conditions.[29] The activity associated with noble metal ions can be accessed in complex oxides where noble metals occupy their own site in the crystal instead of substituting onto another cation site. It has also been demonstrated that pure complex oxides containing noble metals ions in unique crystallographic sites (as opposed to small substitution) can be more effective than the corresponding metallic species supported on oxides for CO oxidation.[103] Complex oxides tend to be more robust and resistant to reduction than binary oxides due to inductive effects from neighboring cations. Of particular interest in complex oxides is the potential for structure-property relationships, with the crystal structure influencing stability and resistance to reduction or degradation.

Conventional solid-state methods for preparation of complex oxides of the platinum group metals generally require extending heating at elevated temperatures multiple re-grinding steps. Long calcination times are required because of the sluggish diffusion kinetics of (for example) Pd^{2+} in the solid state, related to the kinetic inertness of Pd^{2+} in aqueous solution.[104] The usual way to overcome sluggish diffusion is to carry out solid-state reactions at elevated temperatures. However, heating PdO or PtO at elevated temperatures results in auto-reduction, even under flowing O_2,[105] and the metals are sufficiently refractory that their re-oxidation is difficult. Consequently, it can take days or weeks to prepare phase pure platinum group metal oxides using conventional furnace heating methods. Microwave assisted heating significantly shortens the required preparation time for phase pure, high quality materials. Described in the literature as early as the 1980's[88–90], it has been shown that with simple modifications and optimizations, household microwave ovens can be employed to obtain high quality materials among them phosphors with high quantum yields[25, 27, 92], intermetallics[24, 28] and other thermoelectrics.[91] The microwave heats a carbon susceptor material which very rapidly transfers heat to the sample. Here we apply the microwave-assisted heating technique to prepare two prototypical complex oxide materials containing Pd^{2+} and Pt^{2+} and carry out a detailed analysis of their stability. Although this work focuses on solid-state routes for platinum group metal oxide preparation, other methods do exist. Zur Loye and co-workers have reviewed flux growth methods for oxides such as these.[106, 107]

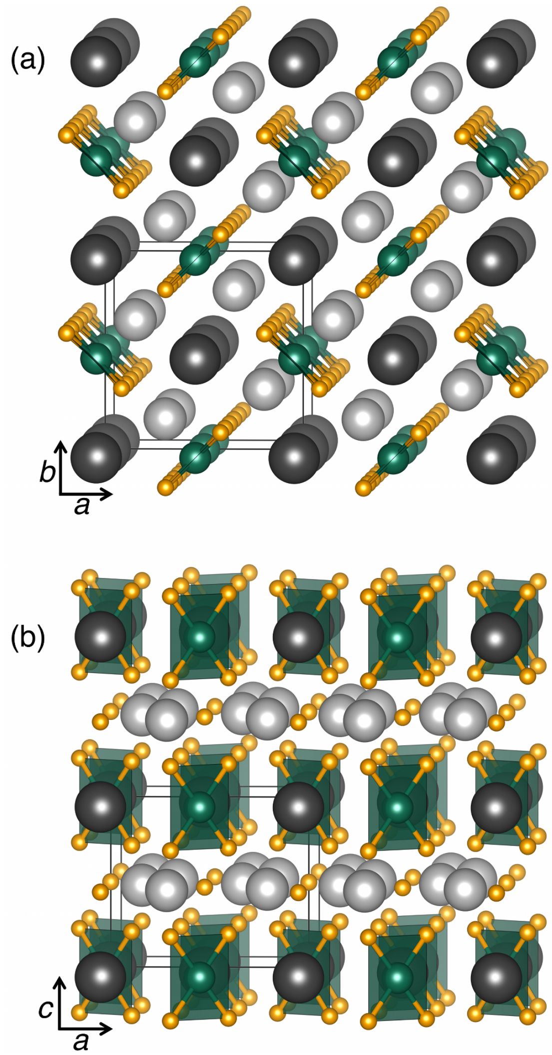

Figure 4.1: The crystal structure for La_2BaMO_5 (M = Pd or Pt) projected nearly down the (a) c axis, and (b) the b axis. The larger dark grey spheres are Ba, the smaller light grey spheres are La. Square planes of (Pd/Pt)O_4 are also depicted. Figure reproduced with permission from Misch *et al.*, *Inorg. Chem.*, reference [102], © 2014 American Chemical Society.

The isostructural compounds La_2BaPdO_5 and La_2BaPtO_5 were prepared using microwave-assisted heating with the aim of accessing ionic Pd and Pt for catalytic applications. La_2BaPdO_5, previously studied by Kurzman *et al.* and shown to be an effective catalyst,[103] is isostructural with Y_2BaPdO_5 reported by Laligant *et al.*[108] The synthesis and structure of La_2BaPtO_5 was reported by Müller-Buschbaum and Schlüter.[109]

The tetragonal structure of these complex oxides, with isolated $(Pd/Pt)O_4$ square planes, is displayed in Figure 4.1. The compounds have been characterized using a combination of synchrotron x-ray diffraction, electron microscopy, and x-ray photoelectron spectroscopy. The reactivity/stability of the compounds have been characterized using thermogravimetric analysis under flowing $5\%H_2/N_2$, in order to establish the enhanced stability of these compounds with respect to the simple oxides PdO and PtO. The formation energies have been calculated using Density Functional Theory (DFT), the origin of the stabilization of the complex oxides when compared with the corresponding simple oxide has been understood on the basis of DFT slab calculations following the method of van de Walle and Martin.[110] Such calculations allow the absolute energies of the different relevant states to be located, and therefore compared across different systems. The results show unambiguously that on going from the simple oxides PdO or PtO to the complex counterparts, La_2BaMO_5 (M

= Pd, Pt), the O-p states in the latter are destabilized ad pushed up by the electropositive cations, and this stabilizes for these oxophobic metal ions in an oxide environment.

4.1.2 Experimental methods

Sample Preparation These samples were prepared *via* microwave-assisted solid-state reaction pathways. For a typical synthesis of La_2BaMO_5 (M = Pd, Pt), stoichiometric amounts of La_2O_3 (heated at 700°C overnight, 99.99%, Sigma Aldrich), M(II) acetylacetonate (M = Pd, Pt, 99% and 97% respectively, Sigma Aldrich) and $BaCO_3$ (99.95%, Alfa Aesar) were thoroughly ground in an agate mortar. A typical batch size of 250-500 mg of the mixed powder is then heated in our hybrid microwave (Panasonic NN-SN667B, 1300 W) setup, as described earlier.[24, 25, 27, 28, 98] A typical heating profile for both materials consisted of maximum power, for about 15 - 20 minutes. For the phase evolution studies, the temperature was measured in various intervals during and after the reaction has finished using an infrared pyrometer (PalmerWahl DHS235XEL), aimed at the center of the inner crucible.

Characterization Laboratory powder X-ray diffraction (XRD) data were obtained using Cu Kα radiation (Philips X'Pert) over the angular range

$15^\circ \leq 2\theta \leq 90^\circ$ with a step size of 0.016°. High resolution synchrotron powder diffraction data were collected using beamline 11-BM at the Advanced Photon Source (APS), Argonne National Laboratory using an average wavelength of 0.413893 Å. Discrete detectors covering an angular range from -6 to 16° 2θ are scanned over a 34° 2θ range, with data points collected every 0.001° 2θ and scan speed of 0.01°/s. Full profile pattern using the LeBail[111] method and Rietveld fits[99] of the collected data were obtained using TOPAS Academic.[100]

TGA was carried out using a METTLER TGA/sDTA851e ThermoGravimetric Analyzer in air scanning the temperature range between 25°C and 900°C at a heating rate of 10 °C per minute. Stability of the compounds in various atmospheres (N_2, Air, and 5% H_2/95% N_2) was monitored using a Cahn TG-2141 TGA. The samples were heated to 1100°C with a heating ramp of 2.5°C/min and two hours of dwell time at the maximum temperature. X-ray photoelectron spectra were obtained on a Kratos Axis Ultra Spectrometer with monochromatic Al-Kα source (E = 1486.61 eV). Samples were mounted on a stainless steel holder using double-sided carbon tape. The residual pressure inside the sample analysis chamber was below 7×10^{-9} Torr. Survey spectra were collected with an analyzer pass energy of 80 eV and high-resolution Pd 3d and Pt 4f spectra were acquired at a pass energy 20 eV. Spectra were analyzed using CasaXPS software. Spectra were calibrated to the C 1s peak from adventitious hydrocarbons, expected at a binding energy of 285.0 eV. For peak fitting of the spin-orbit doublets in high resolution scans, the $d_{3/2}$ to $d_{5/2}$ and the $f_{5/2}$ to $f_{7/2}$ peak areas were constrained to a ratio of 2/3 and 3/4, respectively.

Field-emission scanning electron microscopy was performed on a FEI XL40 Sirion FEG microscope with an Oxford Inca X-ray system attached for chemical analysis. SEM samples were mounted on aluminum stubs using double-sided conductive carbon tape. The images have been recorded with an acceleration voltage of 5 kV.

***Ab-initio* Calculations** All *ab-initio* calculations were performed in the framework of density functional theory (DFT) using the Vienna *ab-initio* Simulation Package (VASP)[112, 113] in which the wavefunctions are described by plane-wave basis and the ionic potential is described by the projector augmented wave (PAW) method of Blöchl[114] and adapted in VASP by Kresse and Joubert[115]. Exchange and correlation was described by the Perdew–Burke–Ernzerhof generalized gradient approximation (GGA-PBE)[116]. The first Brillouin zone was sampled for all reciprocal space integration using a gamma-centered $6 \times 6 \times 6$ Monkhorst-Pack *k*-mesh[117] for La_2BaPdO_5, La_2BaPdO_5, and BaO while a $8 \times 8 \times 4$ *k*-mesh was used for PdO, PtO, and La_2O_3. The energy cutoff of the plane wave basis was 650 eV with the convergence criteria set at 0.01 meV.

4.1.3 Results and Discussion

Preparation and characterization

Microwave-assisted heating allows the investigation of phase evolution and formation of materials in great detail. Samples can be rapidly heated and cooled so that characterization can be performed as the reaction proceeds. We have studied the phase evolution and formation of La_2BaMO_5 (M = Pd, Pt) on a typical La_2BaPdO_5 sample, in 75 s increments. The mole percent of phases detected by X-ray diffraction and Rietveld refinement are displayed in Figure 4.2.

Rietveld refinements of the starting mixture and the mixture after 75 s heating intervals reveal the mole percent of phases present at each heating step. As shown in Figure 4.2, the starting mixture consists only of the expected compounds that have been employed as the reactants. After 75 s of microwave heating, all precursors except the $BaCO_3$ decomposed to form an amorphous reservoir as indicated by the background in the diffraction pattern. Another 75 s further into the reaction, PdO formed, La_2O_3 re-appeared, and a small amount of $La(OH)_3$ was detected. In yet another 75 s (3:45 min of total reaction time) the final product, La_2BaPdO_5, is the majority phase in the diffraction pattern. Minor amounts of Pd^0 and PdO can be indexed in the diffraction pattern, along with some remaining La_2O_3. After 5 min at the maximum power setting, reach-

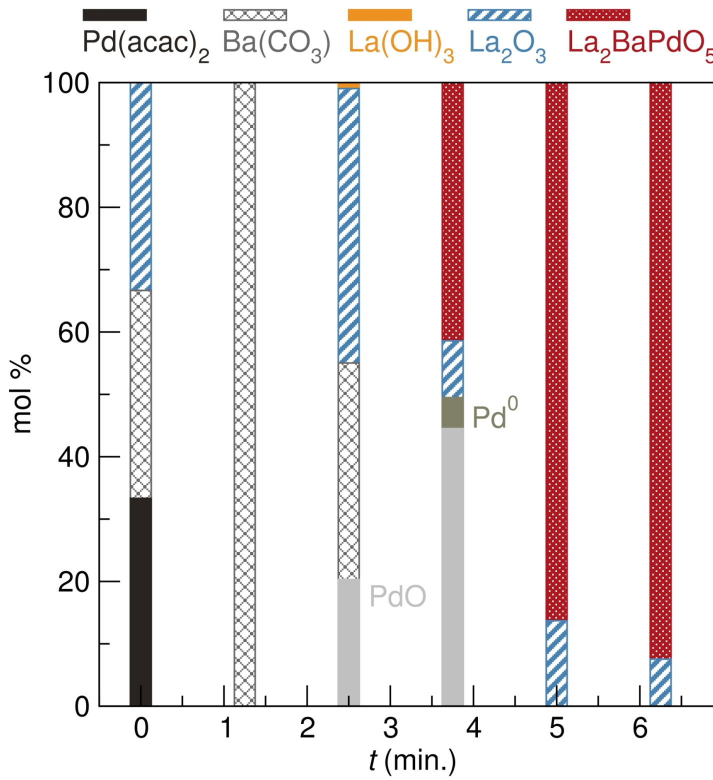

Figure 4.2: Phase evolution of La_2BaPdO_5 prepared by microwave-assisted solid-state heating technique. X-ray diffraction patterns of the starting mixture after 75s heating intervals were taken and Rietveld refinement revealed the mole percent of phases present. The desired phase is achieved after three minutes of reaction time and constitutes the majority of the phases present after six minutes of reaction time. Figure reproduced with permission from Misch *et al.*, *Inorg. Chem.*, reference [102], © 2014 American Chemical Society.

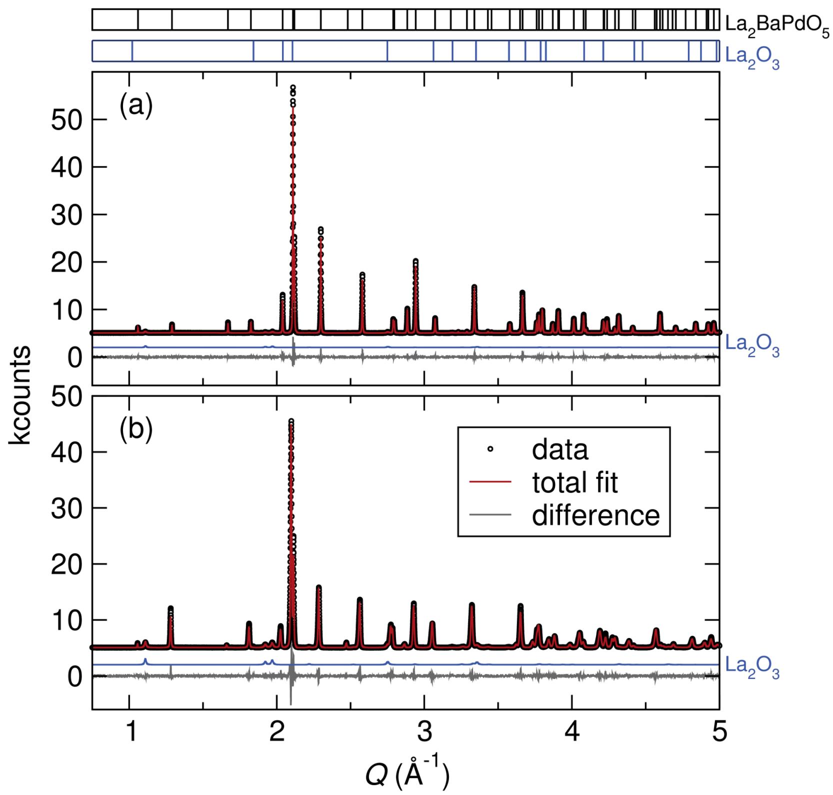

Figure 4.3: Synchrotron X-ray powder diffraction data of (a) La_2BaPdO_5 and (b) La_2BaPtO_5. Figure reproduced with permission from Misch *et al.*, *Inorg. Chem.*, reference [102], © 2014 American Chemical Society.

ing peak temperatures between 1000°C and 1050°C as measured by pyrometry, only trace amounts of La_2O_3 were observed and La_2BaPdO_5 is the majority phase. Although samples were nearly phase pure after 5 min of reaction time, an additional 15 min to 20 min of reaction, after a regrinding step time improved the purity and crystallinity of the product. It is these products that are described in what follows.

Table 4.1: Rietveld Refinement and Crystal Data for La_2BaPdO_5 and La_2BaPtO_5. Figure reproduced with permission from Misch *et al.*, *Inorg. Chem.*, reference [102], © 2014 American Chemical Society.

Formula	La_2BaPdO_5	La_2BaPtO_5
Radiation type, λ (Å)	Synchrotron (11-BM), 0.413893	
2θ range (degree)	2.5–50	
Temperature (K)	295	
Crystal System	hexagonal	hexagonal
Space group	$P4/mbm$	$P4/mbm$
Lattice Parameters (Å)	a = 6.8883(1)	a = 6.9353(3)
	c = 5.9296(1)	c = 5.9444(3)
Volume (Å^3)	V = 281.35(1)	V = 285.91(1)
R_p	7.498	11.353
R_{wp}	9.666	14.065
χ^2	1.568	2.820

The final phase purity of the two complex oxides was investigated using synchrotron X-ray diffraction data. Rietveld fits are shown in Figure 4.3. Both samples show a high degree of phase purity with some small quantities of secondary phases, such as La_2O_3 or $La(OH)_3$; their amounts do not exceed 10 wt-%. The cell parameters, cell volumes, and atomic coordinates derived from the Rietveld fits using TOPAS Academic are are summarized in Tables 4.1 and 4.2. The values found here compare well to the obtained parameters found previously[74, 109] on samples prepared *via* conventional solid-state pathways.

The presence of remaining La_2O_3 in the final product raises the question of the fate of stoichiometric amounts of Ba and Pd precursors. To determine if the other precursors were simply evaporating off, we attempted to prepare La_2BaPdO_5 with a 5 mol% La_2O_3 deficiency. Subsequent laboratory X-ray diffraction data with Rietveld refinement did not show a significant decrease in the La_2O_3 phase present in in the final product, but the formation of *fcc*–Pd metal was promoted. Ultimately, we expect that the Ba and Pd precursors are, in fact, still present in the final material, but are much less than are easily detectable. Previous work has shown that Ba readily binds hydroxyls, carbonates, and other surface species, rendering the Ba species not incorporated into the final product hard to detect by XRD.[35] Due to the lower atomic weight, Pd does not scatter as significantly as compared to La and Ba.

X-ray photoelectron spectroscopy was performed to determine the oxidation state of the Pd and Pt in La_2BaMO_5. Survey scans indicated that no elements besides the anticipated La, Ba, Pd, Pt, O were present. Carbon was present due to sample mounting on double-sided carbon tape. The high resolution scan of La_2BaPdO_5 showed Pd 3d peaks to be shifted to higher binding energy than Pd^0 and Pd^{2+} in PdO. This is representative of a highly ionic Pd environment. The observed peak positions and anticipated positions for the reference materials is shown in Figure 4.4(a).

The initial high resolution scan of La_2BaPtO_5, showed two doublets in the Pt 4f region, suggesting some surface reaction. Argon sputtering of the sample followed by another high resolution scan, Figure 4.4 (b), of the Pt 4f region primarily showed mostly a single doublet contributing to the total signal and a decreased contribution from the another doublet that we associate with the The Pt 4f binding energy is typical of Pt^{2+} species, and the shift from Pt^0 to Pt^{2+} is comparable to what is seen in the case of Pd^0 to Pd^{2+}.

The morphological features of the two complex oxides were investigated using scanning electron microscopy, the obtained images are presented in Figure 4.5. Both samples, La_2BaPdO_5 and La_2BaPtO_5 exhibit comparable morphologies, with almost spherical particles and sizes ranging from 100 nm in diameter to several micrometers. The average size of the particles, derived from measurements of several hundred of particles is about 0.56 μm and 0.58 μm for La_2BaPdO_5 and La_2BaPtO_5, respectively. The values found from electron microscopy agree with the calculated crystallite sizes from the synchrotron data,

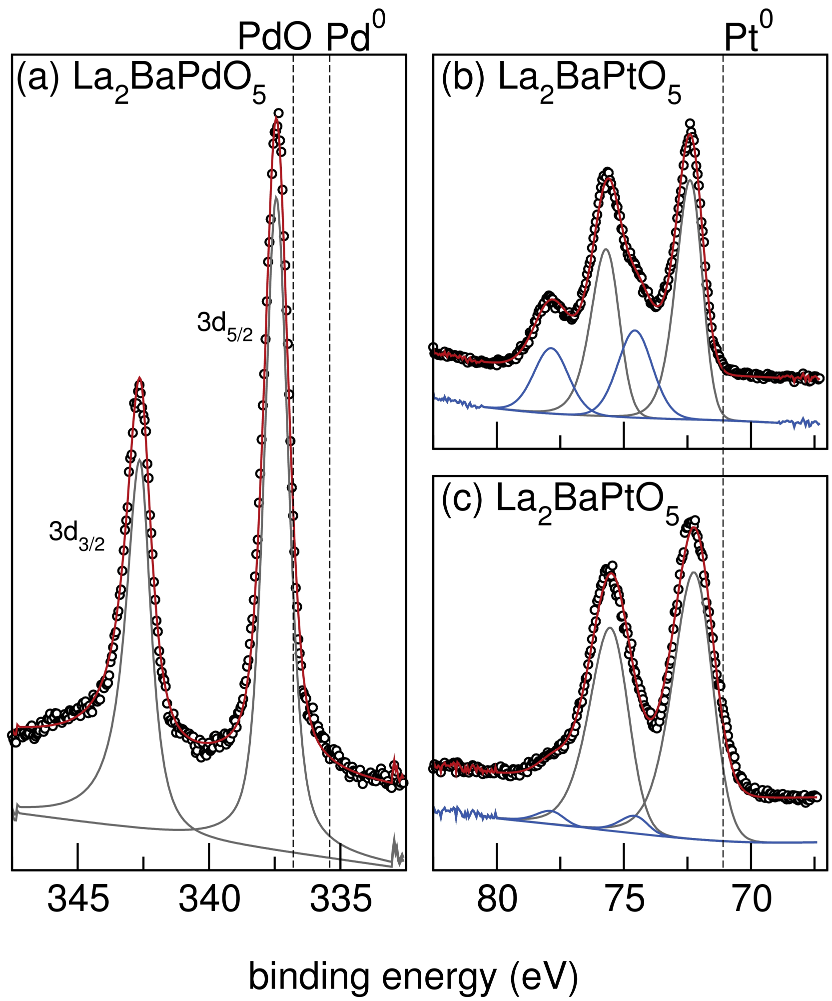

Figure 4.4: X-ray photoelectron spectra for the Pd 3d and Pt 4f regions in (a) La_2BaPdO_5 and (b,c) La_2BaPtO_5. La_2BaPtO_5 as prepared (b) showed two doublets in the Pt 4f region, while La_2BaPtO_5 with Ar sputtering (c) showed mostly one doublet in the Pt 4f region. Ar sputtering was necessary to deconvolute the surface contribution from the actual contribution from the Pt environment. Figure reproduced with permission from Misch *et al.*, *Inorg. Chem.*, reference [102], © 2014 American Chemical Society.

about 0.4 μm. The slightly smaller size derived from the refinement might point towards the fact that the particles are not entirely single crystalline, but rather consist of several domains. It is important to note here that the crystallite and/or particle size can very easily be influenced by extending or shortening the microwave heating treatment. Energy dispersive X-ray spectroscopy and elemental mapping also indicated that ions were well dispersed throughout the materials.

The addition of electropositive cations to the surrounding structure for noble metals will stabilize the noble metal d-states.[22] With this in mind, it is likely that the Pd ions in the complex structures would reduce to Pd metal at higher temperatures than PdO. By designing a material that would maintain Pd ionicity at high temperatures even in reducing conditions will be adventitious when considering catalytic applications. To probe the stability with respect to decomposition at elevated temperatures, La_2BaPdO_5 and La_2BaPtO_5 were heated in flowing 5%H_2/95%N_2 from room temperature to 1000°C at 2.5°C/min. The decomposition profiles are shown in Figure 4.6. Just before the major decomposition near 500°C, an increase in mass is observed due to buoyancy effects in the TGA. At 600°C, La_2BaPdO_5 and La_2BaPtO_5 experienced the most significant mass loss. We expect that this loss corresponds to the reduction of the Pd or Pt ion to metal with the loss of $\frac{1}{2}O_2$, reflected in Equation 4.2. La_2BaPdO_5 and La_2BaPtO_5 are expected to lose 2.6% and 2.3%, respectively. These theo-

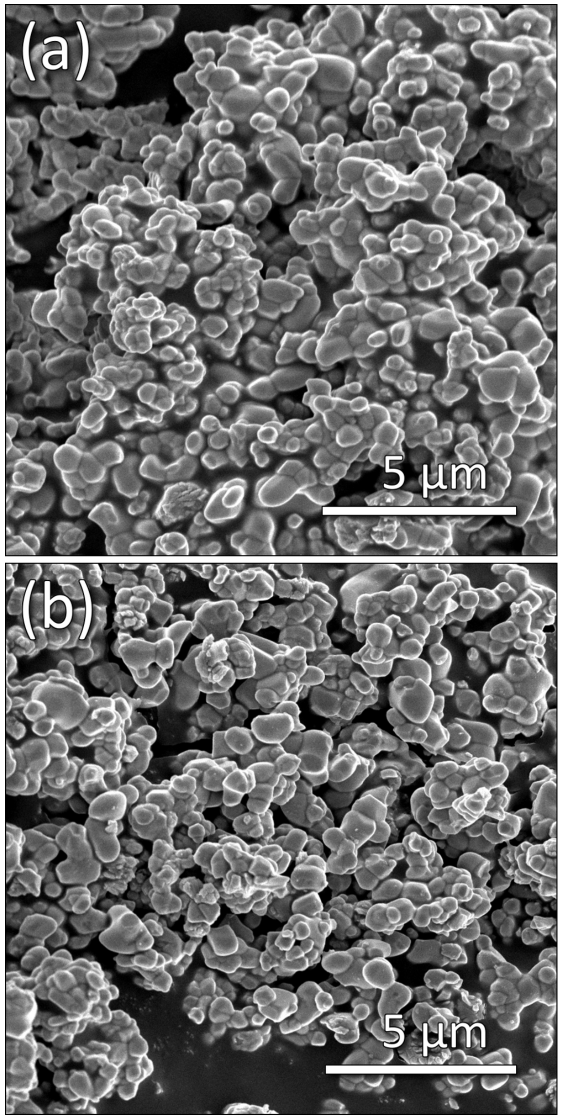

Figure 4.5: Scanning electron micrographs of (a) La_2BaPdO_5 and (b) La_2BaPtO_5 indicate consistent morphology and uniform particle size for samples prepared using microwave-assisted heating. Figure reproduced with permission from Misch *et al.*, *Inorg. Chem.*, reference [102], © 2014 American Chemical Society.

retical losses are indicated with dashed lines in Figure 4.6. La_2BaPtO_5 reduces just before the Pd analog, yet their decomposition profiles are nearly identical. For comparison, the same experiment was carried out for the binary PdO. Here, when placed under flowing 5%H_2/95%N_2 the compound reduces readily at room temperature.

Ab-initio studies of the stability

The elevated temperature required to reduce the complex oxides is considerably different compared to the binary oxides, in particular PdO, which reduces at room temperature in air. To gauge the effect of structure and composition on this notable difference, the energetics of formation were calculated based on first principles. A hypothetical decomposition was considered following Equations 4.1 and 4.2, where M is Pd or Pt.

$$M\mathrm{O} \rightarrow M + \frac{1}{2}\mathrm{O}_2 \tag{4.1}$$

$$\mathrm{La_2Ba}M\mathrm{O_5} \rightarrow \mathrm{La_2O_3} + \mathrm{BaO} + M + \frac{1}{2}\mathrm{O}_2 \tag{4.2}$$

The total energy of these reactions (ΔE) at 0 K, were calculated as a function of oxygen chemical potential (μ_O) using Equations 4.3 and 4.4,

$$\Delta E = E_{M\mathrm{O}} - E_M - \mu_\mathrm{O} - \frac{1}{2}E_{\mathrm{O}_2} \tag{4.3}$$

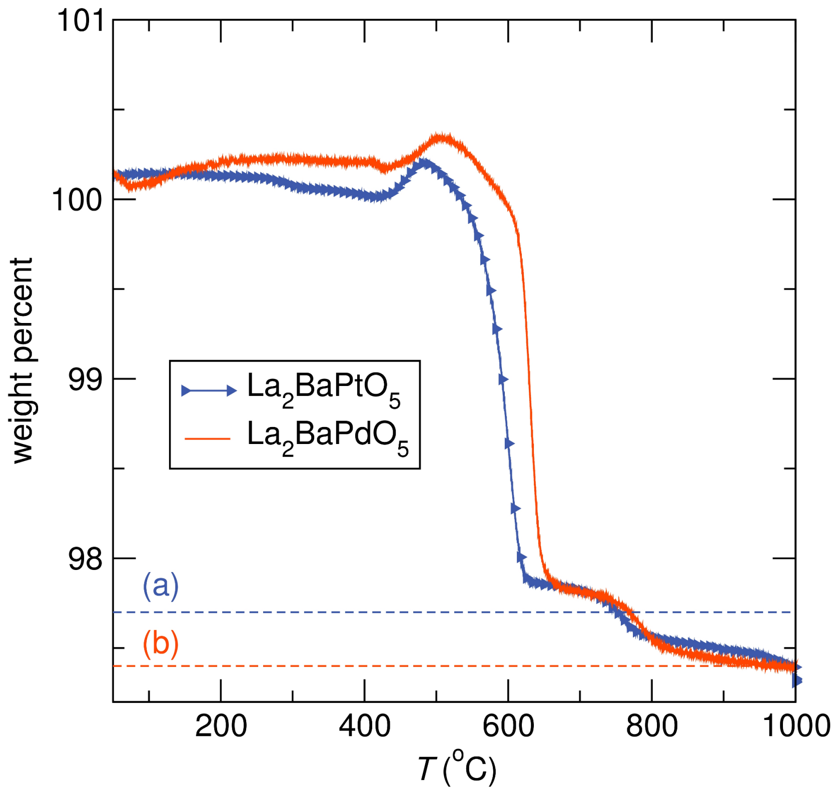

Figure 4.6: Thermogravmetric analysis of the decomposition of final product acheived after microwave heating. Samples were heated from room temperature to 1000°C at 2.5°C/min in 5%H_2/95%N_2. La_2BaPdO_5 reduces at a slightly higher temperature than La_2BaPtO_5 and their decomposition profiles are very similar. La_2BaPdO_5 and La_2BaPtO_5 are expected to lose 2.6% and 2.3%, respectively, based on Equation 4.2. These losses are indicated with dashed lines, (a) 2.3% for La_2BaPtO_5 and (b) 2.6% for La_2BaPdO_5, subracted from 100%. Figure reproduced with permission from Misch *et al.*, *Inorg. Chem.*, reference [102], © 2014 American Chemical Society.

$$\Delta E = E_{\mathrm{La_2Ba}M\mathrm{O_5}} - E_{\mathrm{La_2O_3}} - E_{\mathrm{BaO}} - E_M - \mu_{\mathrm{O}} - \frac{1}{2}E_{\mathrm{O_2}} \tag{4.4}$$

where, $E_{\mathrm{La_2Ba}M\mathrm{O_5}}$, $E_{M\mathrm{O}}$, $E_{\mathrm{La_2O_3}}$, E_{BaO}, and E_M $E_{\mathrm{O_2}}$ are the total calculated energies *per* formula unit.

In the calculations, μ_{O} is the oxygen chemical potential, which varies as a function temperature and oxygen partial pressure (p) following the equation $\mu_{\mathrm{O_2}} = E_{\mathrm{O_2}} - kT \ln \frac{p_0}{p}$. As illustrated in Figure 4.7, the binary oxides are favored at relatively high chemical potentials of O_2 (μ_{O}¡-1 eV) but at lower chemical potentials, display a decided preference to reduce to the metal. The equilibrium favors the complex oxides across a much wider μ_{O} range, and decomposition is favored only when μ_{O} $>$3.5 eV. Moreover, the decomposition of PtO occurs at a higher chemical potential, μ_{O} $\approx$2.5 eV, suggesting that the stabilization against reduction to the metal in the complex oxides is much more dramatic in La_2BaPtO_5 than in La_2BaPdO_5.

The origin of relative stability again decomposition for these complex oxides compared to the binary metal oxides was established from the electronic structures. To allow a direct comparison of the density of states (DOS) for PdO, PtO, La_2BaPdO_5, and La_2BaPtO_5 band offset calculations were carried out (Figure 4.8). Slabs models were constructed using an $8 \times 1 \times 1$ supercell with four

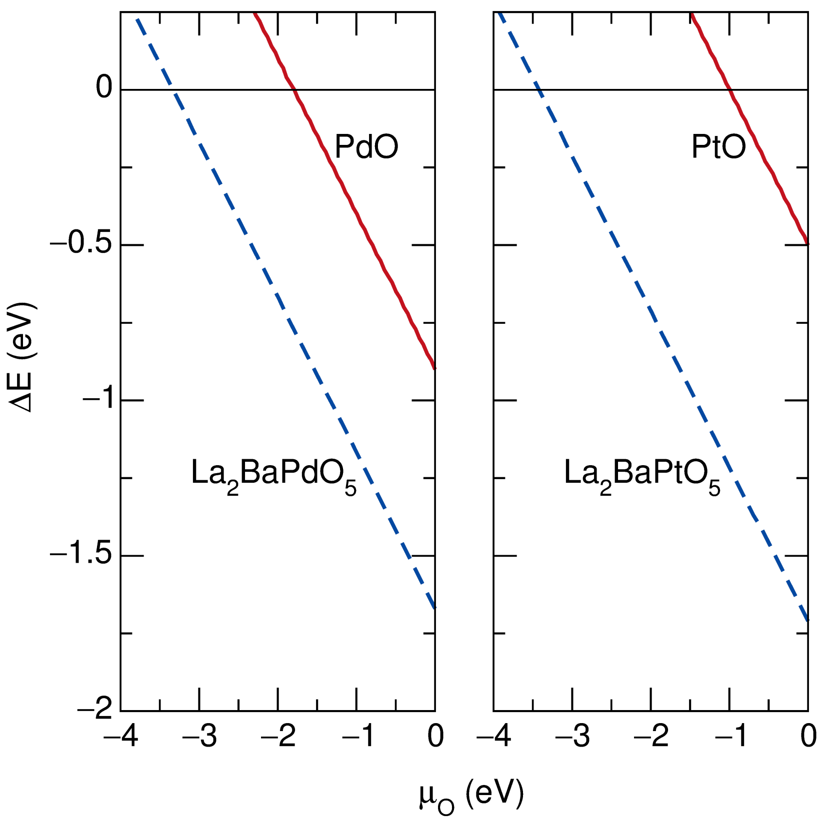

Figure 4.7: The enthalpy of formation (ΔE) as a function of oxygen chemical potential (μ_{O}) for the reactions outlined in Eqs. 4.1 and 4.2. The partial pressure of oxygen is assumed to be $1{\times}10^{-10}$ Pa. and a temperature ranging from 0 K to 1100 K

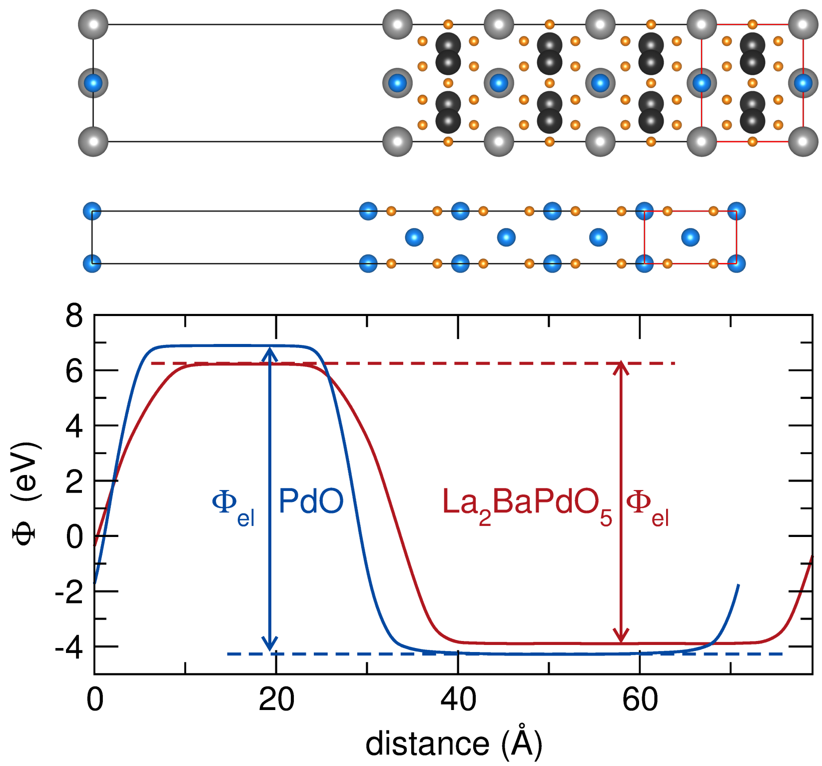

Figure 4.8: Band offset calculations for La_2BaPdO_5 (top) and PdO (middle) were carried out to allow a direct comparison of the band positions. Figure reproduced with permission from Misch *et al.*, *Inorg. Chem.*, reference [102], © 2014 American Chemical Society.

cells containing the respective structures and four vacuum cells. The difference between the vacuum energy and the average electrostatic potential (Φ_{el}) is used to normalize the position of the Fermi level (E_F) for these systems. The band positions were determined by aligning the center of the vacuum region with the center of the atomic electrostatic potential (assuming it represents the bulk potential).

The DOS of La_2BaPdO_5[74] and PdO are illustrated in Figure 4.9 while La_2BaPtO_5 and PtO are shown in Figure 4.10. The electronic structures of the binary oxides differ significantly compared to the complex oxides. Most notably, in the case of palladium, PdO is a metal whereas La_2BaPdO_5 is a semiconductor. However, the metallicity for PdO is an artefact due to the PBE functional. It has been shown previously that using a screened-hybrid functional (*e.g.*, HSE06) opens a 1 eV gap at the Fermi level.[103] In PdO, the O 2p bands are rather disperse with a majority of the states residing between -12 eV and -8 eV while the remainder extend across E_F. The Pd 4d orbitals in PdO are fairly narrow between -8 eV to -3 eV. The complex oxide, La_2BaPdO_5, has a wider band gap ($\approx$2 eV) compared to the binary oxide with the valence band maximum (VBM) composed of Pd 4d states and the conduction band minimum (CBM) coming from the O 2p states. The Pd 4d states span from -7 eV to the E_F while the O 2p orbitals are higher in energy compared to PdO showing nearly perfect

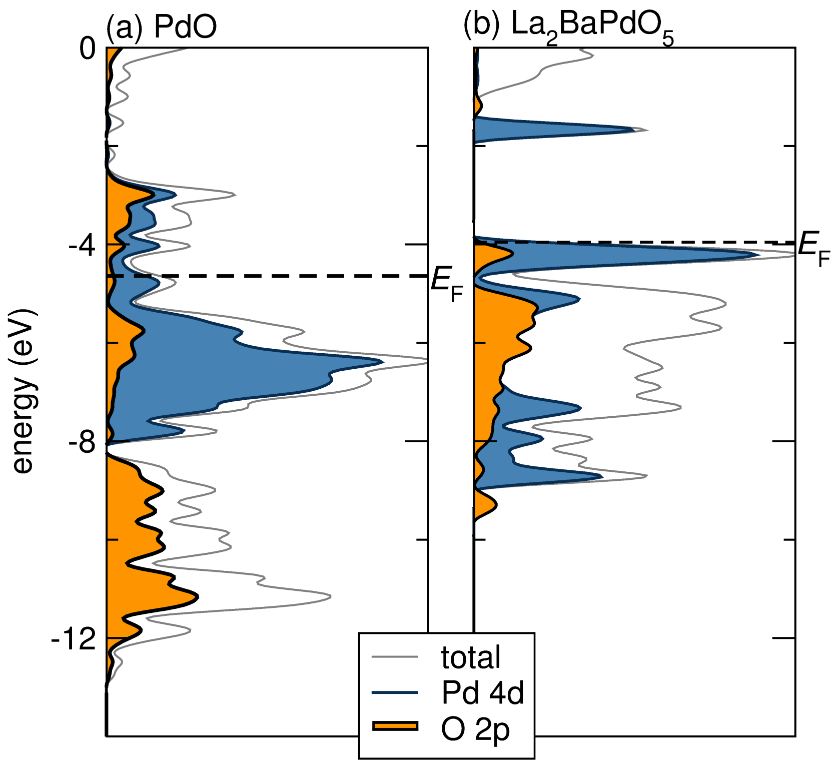

Figure 4.9: The calculated density of states for (a) PdO and (b) La_2BaPdO_5 using the PBE functional. The O 2p partial DOS corresponds to the Pd nearest neighbors. E_F is -4.64 eV for PdO and -3.95 eV for La_2BaPdO_5 relative to vacuum. Figure reproduced with permission from Misch *et al.*, *Inorg. Chem.*, reference [102], © 2014 American Chemical Society.

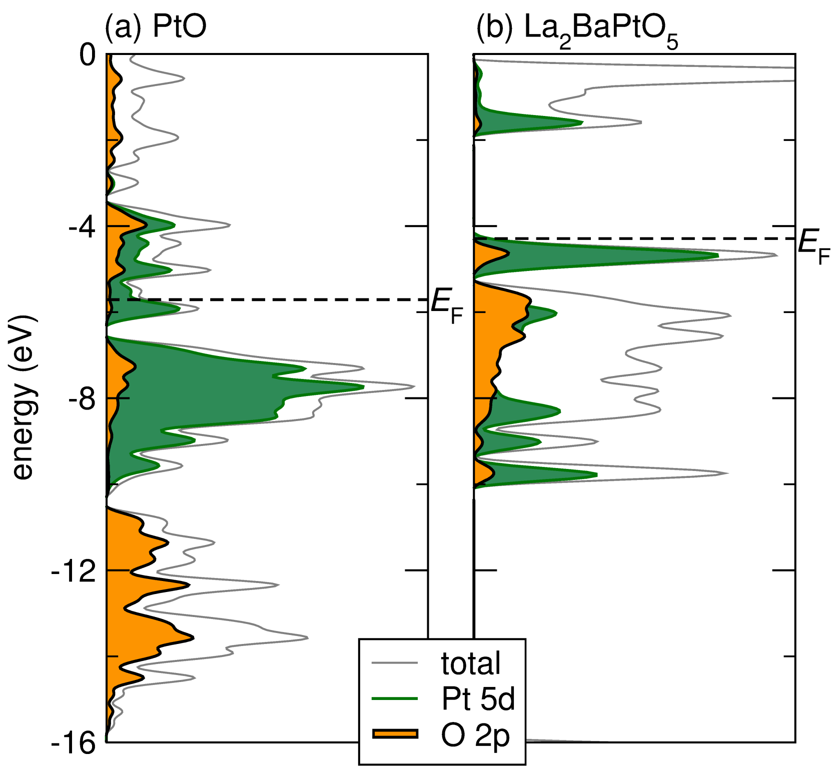

Figure 4.10: The calculated density of states for (a) PtO and (b) La_2BaPtO_5 using the PBE functional. The O 2p partial DOS corresponds to the Pd nearest neighbors. E_F is -5.71 eV for PtO and -4.29 for La_2BaPtO_5 relative to vacuum. Figure reproduced with permission from Misch *et al.*, *Inorg. Chem.*, reference [102], © 2014 American Chemical Society.

energetic overlap with the Pd 4d orbitals. The DOS of the Pt-oxides are nearly identical to the Pd-oxides. In PtO, the compound is also calculated to be a metal, although using a hybrid functional will open a gap.[118] The O 2p orbitals span a wider energy range, between -16 eV to above E_F, with a majority of the states between -16 eV and -10 eV. The Pt 5d orbitals have nearly the same band dispersion as PdO extending from approximately -10 eV to the -4 eV. La_2BaPtO_5 also has a similar electronic structure to the Pd analogue. The O 2p bands range between -10 eV and E_F as well as above -2 eV composing the CBM. The Pt 5d orbitals are in the same energy region, between -10 eV and E_F, and make up the VBM.

The changes in the DOS going from the binary oxide to the complex oxide are due to the incorporation of the more electropositive cations in the structure (*i.e.*, Ba^{2+} and La^{3+}).[22] Adding the unoccupied orbitals of these cations destabilizes the oxygen 2p states raising their energy, as observed in Figures 4.9 and 4.10. Increasing the energy of the O 2p states to the same energy window as the transition metal promotes orbital overlap of the M–O square-planes. These changes in electronic structure suggest a pathway for the stabilization of these complex oxides with respect to reduction.

4.1.4 Conclusions

La_2BaPdO_5 and La_2BaPtO_5 were prepared using microwave-assisted heating. X-ray diffraction indicated that the desired phase was present after just a few minutes and that highly crystalline materials could be achieved after 20 min of heating. This represents significant savings in time, compared to conventional solid state methods, that can take days or weeks of heating. Confirmed by XPS and TGA, these materials stabilize ionic Pd^{2+} and Pt^{2+} and maintain their ionic nature up to 600°C under 5%H_2/N_2. The stability of Pd^{2+} and Pt^{2+} ions is directly related to the introduction of electropositive cations into the surrounding lattice. Electronic structure calculations using DFT, of the energies of formation and of the absolute energetics of electronic states support such stabilization and and provide credence for the hypothesis that O-p states are shifted up in energy with the introduction of these cations, to contribute to increased covalency of O p with noble-metal d states.

4.2 Other complex oxide systems

4.2.1 Introduction

The microwave-assisted heating method allowed for rapid investigation of several other Pd–containing complex oxides. Attfield, Férey, and co-workers pioneered this area are in the late 80's, with $LiBiPd_2O_4$, La_4PdO_7, and $La_2Pd_2O_5$.[108, 119, 120] These three materials were prepared with conventional solid state methods. $LiBiPd_2O_4$ required two heating steps at 500°C and 700°C for 18 h and 7 h, respectively. There has not been much further investigation of these oxides. One report of $LiBiPd_2O_4$ for interlayer communication[121] and a few reports of thermodynamic properties for $La_2Pd_2O_5$ and La_4PdO_7 and for various applications, such as magnetic materials and exhaust emissions catalysis.[122, 122] The layered structure of $LiBiPd_2O_4$, shown in Figure 4.11, indicates that ion conduction could occur readily in this oxide. $LiBiPd_2O_4$ was prepared using our microwave-assisted heating method with the aim of doing conductivity measurements. Attempts were made at microwave-assisted preparation of La_4PdO_7 and $La_2Pd_2O_7$ with various applications in mind.

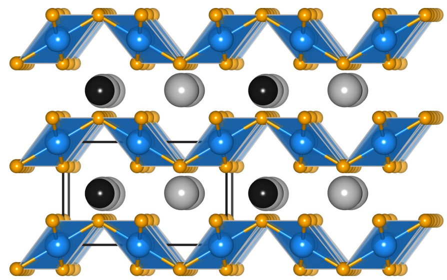

Figure 4.11: Crystal structure for $LiBiPd_2O_4$

4.2.2 Experimental procedures

$LiBiPd_2O_4$ was prepared using solid-state microwave-assisted heating methods, as described earlier in this chapter. Stoichiometric amounts of Li_2CO_3 (99.9%, Sigma Aldrich), Bi_2O_3 (99.99%, Sigma Aldrich), and PdO (99.999%, Sigma Aldrich) were ground together using an agate mortar and pestle. The precursor material was placed in an alumina crucible and inserted into the larger, carbon susceptor containing crucible, and placed in the alumina fiber board housing. Materials were heated for 5 min at 50% power followed by 5 min at 70% power with no intermediate griding step. La_4PdO_7 and $La_2Pd_2O_7$ were both prepared with stoichiometric amounts of La_2O_3 (heated at 700°C overnight, 99.99%, Sigma Aldrich) and PdO (99.999%, Sigma Aldrich. Neither of these oxides have yet been prepared as completely phase pure, and an appropriate heating profile has not yet been identified.

Laboratory powder X-ray diffraction (XRD) data were obtained using Cu Kα radiation (Philips X'Pert) over the angular range $15^\circ \leq 2\theta \leq 90^\circ$ with a step size of 0.016°. Full profile pattern using the LeBail[111] method and Rietveld fits[99] of the collected data were obtained using TOPAS Academic.[100] X-ray photoelectron spectra were obtained on a Kratos Axis Ultra Spectrometer with monochromatic Al-Kα source (E = 1486.61 eV). Samples were mounted on a stainless steel holder using double-sided carbon tape. The residual pressure inside the sample analysis chamber was below 7×10^{-9} Torr. Survey spectra were collected with an analyzer pass energy of 80 eV and high-resolution Pd 3d and Pt 4f spectra were acquired at a pass energy 20 eV. Spectra were analyzed using CasaXPS software. Spectra were calibrated to the C 1s peak from adventitious hydrocarbons, expected at a binding energy of 285.0 eV. For peak fitting of the spin-orbit doublets in high resolution scans, the $d_{3/2}$ to $d_{5/2}$ peak areas were constrained to a ratio of 2/3.

4.2.3 Results and Discussion

$LiBiPd_2O_4$ was prepared relatively phase pure. X-ray diffraction data is shown in Figure 4.12. As is indicated in the figure, a PdO impurity remained. An attempt was made at preparing this material with a PdO deficiency, instead of stiochiometric amounts of precursor. However, this lead to $LiBiO_2$ formation along with *fcc*-Pd. X-ray photoelectron spectroscopy of the Pd 3d region for $LiBiPd_2O_4$ indicates two Pd contributions. This is not unexpected based on our results from diffraction, as there is a Pd position in the desired phase along with a Pd contribution from PdO. The more ionic contribution appears at slightly higher binding energy than the additional PdO contribution, indicated in Figure 4.13 with a dashed line.

This material was tested for ion conductivity and temperature dependent resistivity is shown in Figure 4.14. A metallic, conducting material would exhibit constant resistivity over the temperature range. $LiBiPd_2O_4$ behaves more like a semiconductor, but exhibits mostly insulating behavior. Ca–doping onto the Li site has been considered as a possibility for improving the conductivity. However, phase separation occurs when introducing Ca and more work is required to test this hypothesis.

La_4PdO_7 was attempted with a similar heating profile as that chosen for

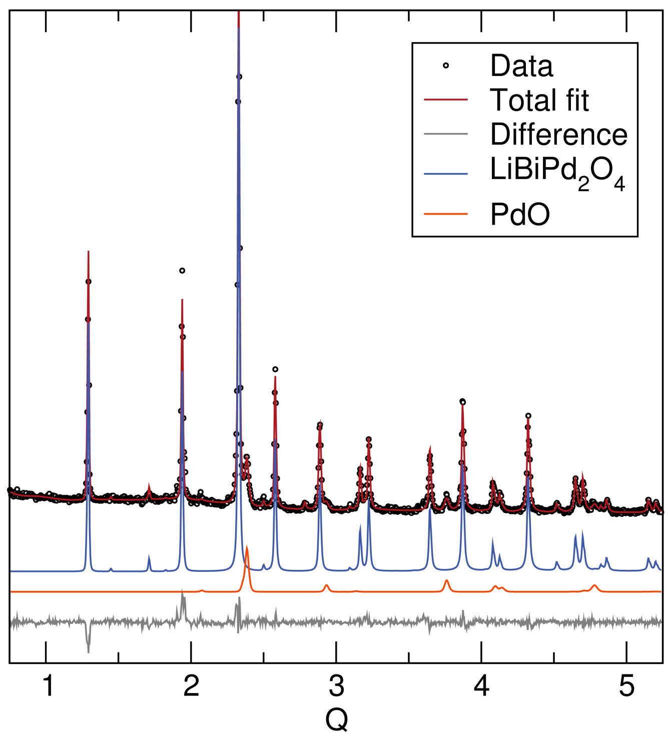

Figure 4.12: Laboratory X-ray diffraction data with Rietveld refinement indicates that the desired phase is present along with a PdO impurity.

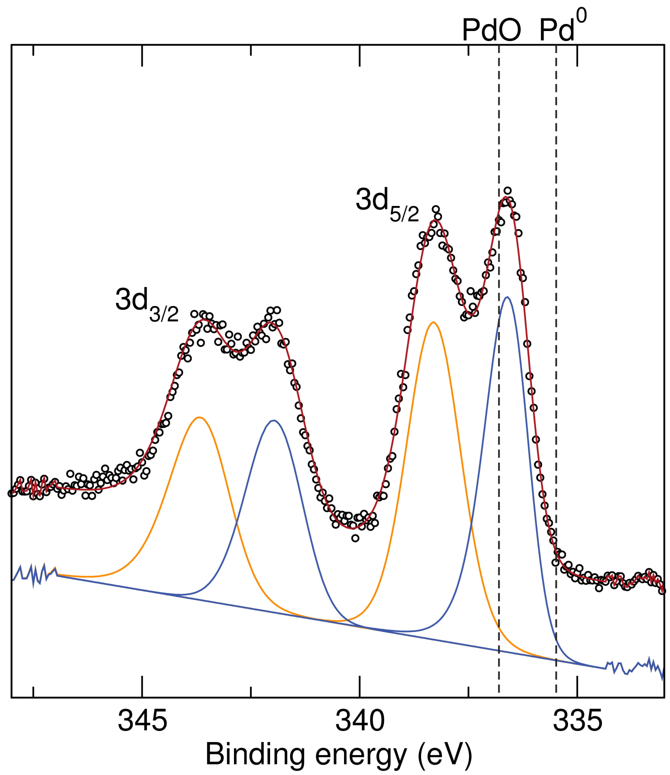

Figure 4.13: X-ray photoelectron spectrum of the Pd 3d region for $LiBiPd_2O_4$ shows two Pd contributions. The contribution at higher binding energy is from Pd in the complex oxide phase while the lower binding energy contribution is from PdO. This matches well with the diffraction results.

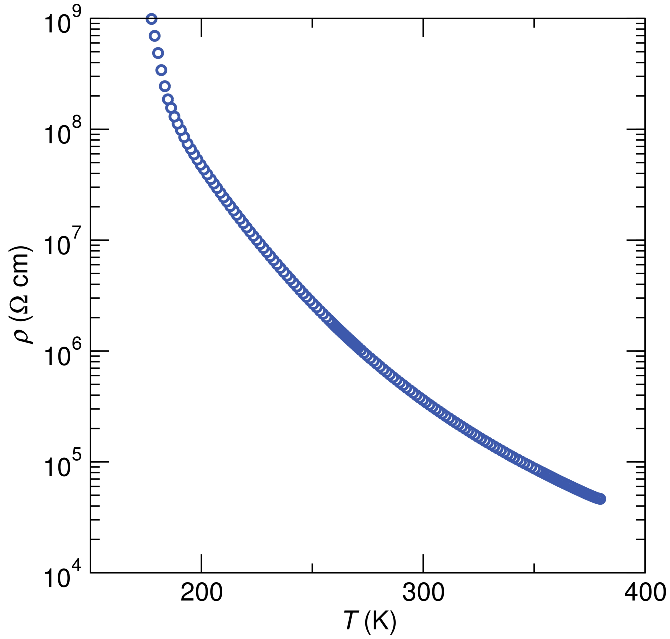

Figure 4.14: Resistivity measurements indicate that $LiBiPd_2O_4$ behaves like an insulator.

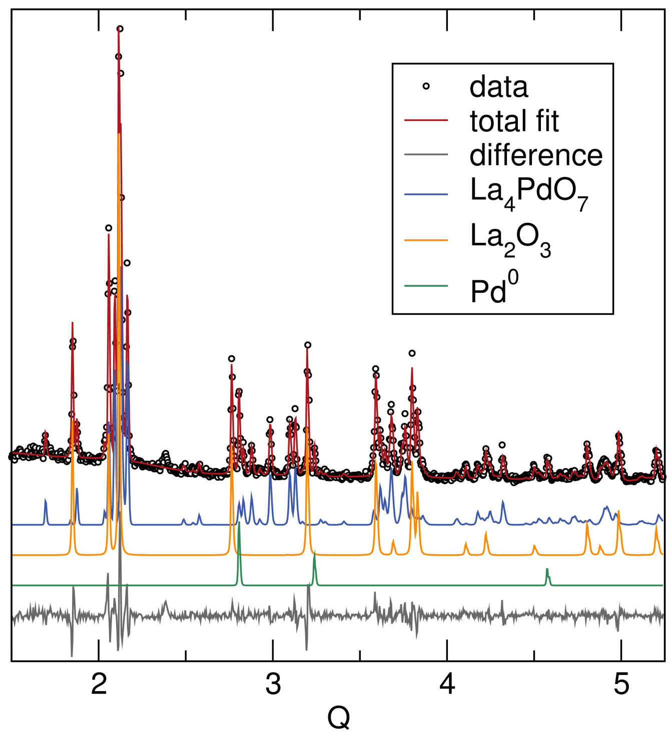

Figure 4.15: Laboratory X-ray diffraction data with Rietveld refinement indicates that the desired phase is present, but the reaction has not gone to completion and La_2O_3 and PdO phases are still present.

$LiBiPd_2O_4$. Laboratory X-ray diffraction data with Rietveld refinement is shown in 4.15. The desired phase is formed, but it appears as though this microwave reaction has not gone to completion as peaks for both precursor materials are present. $La_2Pd_2O_5$ could not be formed with these conditions. Further investigation towards a more appropriate heating profile in the microwave may yield phase formation.

4.2.4 Conclusions

Complex oxides can be prepared using microwave-assisted heating methods, with a tremendous improvement on the overall reaction time required for phase formation. $LiBiPd_2O_4$ was prepared relatively phase pure and ionic. This material was tested for ion conductivity but more work on improving this material is required. One possibility could be Ca-doping in the Li site. Additional work is also required for phase formation of the LaPdO ternary oxides.

Table 4.2: Refined atomic coordinates and equivalent isotropic displacement parameters of (a) La_2BaPdO_5 and (b) La_2BaPtO_5 determined by Rietveld refinement of powder synchrotron X-ray diffraction data collected at room temperature. Figure reproduced with permission from Misch *et al.*, *Inorg. Chem.*, reference [102],

(a) La_2BaPdO_5

Atom	Wyck. Position	Occ.	x	y	z	B_{eq} (Å^2)
La1	$4h$	1	0.174(1)	0.674(1)	$\frac{1}{2}$	0.397(3)
Ba1	$2a$	1	0	0	0	0.805(5)
Pd1	$2d$	1	0	$\frac{1}{2}$	0	0.358(5)
O1	$8k$	1	0.359(1)	0.859(1)	0.755(1)	0.676(3)
O2	$2b$	1	0	0	$\frac{1}{2}$	0.759(5)
(b) La_2BaPtO_5						
La1	$4h$	1	0.174(1)	0.674(1)	$\frac{1}{2}$	0.298(8)
Ba1	$2a$	1	0	0	0	0.83(1)
Pt1	$2d$	1	0	$\frac{1}{2}$	0	0.304(9)
O1	$8k$	1	0.361(1)	0.861(1)	0.751(1)	0.84(6)
O2	$2b$	1	0	0	$\frac{1}{2}$	0.61(1)

Chapter 5

Summary and Outlook

Through our study of noble metal ions, specifically Pd, substituted and stabilized into oxide lattices, we have discovered novel methods of preparation that will be suitable for other substituted or stoichiometric materials for various applications. USP has already been employed to prepare $Nd_2Ru_2O_7$ for thermoelectric measurements, etc.[24] The importance of specialized characterization for these materials cannot be over-emphasized. Neutron diffraction is one method for elucidating the sometimes complicated structures for substituted metal oxides. We have shown that Pd–substituted CeO_2 readily reduces to *fcc*-Pd on CeO_2. It would be interesting to know more precisely how Pd substituted on the Ce site in this binary oxide. Scanlon *et al.* suggested that Pd may

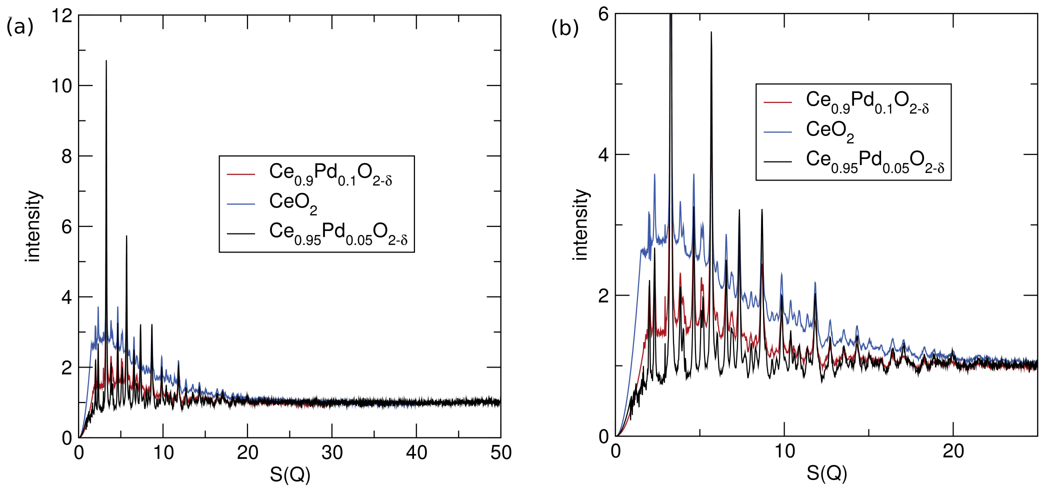

Figure 5.1: Neutron diffraction taken on NPDF at Los Alamos National Lab. Diffraction patterns for 0, 5, 10%Pd-CeO_2 have a large background at low Q, indicative of surface hydrogen. (a) is the full data set, while (b) the same data zoomed in on a the low Q region.

prefer a square planar d^8 configuration over the octahedral configuration taken by Ce. Neutron diffraction could tell us more about Pd–O bond distances and allow us to better understand oxygen vacancies in these systems.

Along with oxygen vacancies, some materials having aliovalent substitutions may have significant surface hydrogen to account for charge imbalance. Our attempts at neutron diffraction on Pd–substituted CeO_2 revealed just that. Shown in Figure 5.1 is the raw neutron diffraction data for 0, 5, 10%Pd–substituted CeO_2. The large background at low Q is indicative of surface hydrogen. The data for 5%Pd–substituted CeO_2 was able to be transformed into the more com-

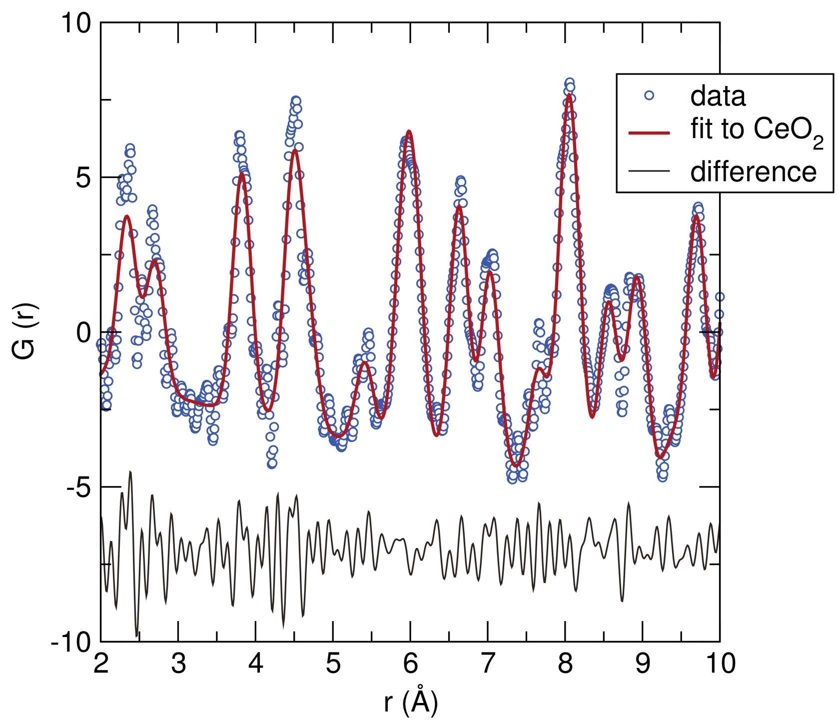

Figure 5.2: Transformed neutron diffraction data for 5%Pd–CeO_2 with fit to CeO_2. There is not excellent agreement between our data and the model, this continues to be a result of surface hydrogen contributions.

pelling $G(r)$ data, which displays peaks for bond distances in the material. The $G(r)$ data is shown in Figure 5.2, but the fit to CeO_2 is not spectacular. There is more to be determined about the structure of Pd–substituted CeO_2 and other substituted oxides.

The issue of surface hydrogen on substituted oxides peaked our interest about the utility of tightly bound surface species such as this. Perhaps substituted oxides could behave like solid-state acid catalysts. Just as aluminum on silicon sites in zeolites generates acidity in solids, so too should lower valence substitution on higher valence cation sites in complex oxides give rise to acidity through proton charge compensation. Additional exploration in this area could be very exciting. Along with neutron diffraction to determine more precise crystal structure for substituted oxides, extended X-ray absorption fine structure (EXAFS) measurements can be extremely beneficial. We have initiated work on *in–situ* EXAFS measurements on Pd–substituted $LaFeO_3$ and $YFeO_3$ to determine the redox behavior.

In general, there is still much to discover for oxide catalysts and ionic species. Methods for preparation and characterization of these types of materials are just becoming established. A new catalyst for energy conversion really could have a significant impact on our society. The potential for making such a contribution to scientific research is nothing short of thrilling. For this reason, researchers will continue to pursue this area. Our understanding, techniques, and instrumentation will only continue to improve. When considering how scientific research has developed over the past century, especially more recently with computer technology and Internet access, it is not an overstatement to say that the possibilities are endless.

Bibliography

[1] D. S. Jenkinson. The impact of humans on the nitrogen cycle, with focus on temperate arable agriculture. *Plant Soil*, 228:3–15, 2001.

[2] K. D. Karlin. Metalloenzymes, structural motifs, and inorganic models. *Science*, 261:701–708, 1993.

[3] J. Kašpar, P. Fornasiero, and N. Hickey. Automotive catalytic converters: current status and some perspectives. *Catal. Today*, 77:419–449, 2003.

[4] R. Martin and S. L. Buchwald. Palladium-catalyzed Suzuki-Miyaura cross-coupling reactions employing dialkylbiaryl phosphine ligands. *Acc. Chem. Res.*, 41:1461–1473, 2008.

[5] L. Yin and J. Liebscher. Carbon–carbon coupling reactions catalyzed by heterogeneous palladium catalysts. *Chem. Rev.*, 107:133–173, 2007.

[6] C. H. Bartholomew and R. J. Farrauto. *Fundamentals of Industrial Catalytic Processes*. 2011.

[7] Y. Nishihata, J. Mizuki, T. Akao, H. Tanaka, M. Uenishi, M. Kimura, T. Okamoto, and N. Hamada. Self-regeneration of a Pd-perovskite catalyst for automotive emissions control. *Nature*, (6894):164–167, 2002.

[8] J. Li, U. G. Singh, T. D. Schladt, J. K. Stalick, S. L. Scott, and R. Seshadri. Hexagonal $YFe_{1-x}Pd_xO_{3-\delta}$: Nonperovskite host compounds for Pd^{2+} and their catalytic activity for CO oxidation. *Chem. Mater.*, 20:6567–6576, 2008.

[9] U. Singh, J. Li, J. Bennett, A. Rappe, R. Seshadri, and S. Scott. A Pd-doped perovskite catalyst, $BaCe_{1-x}Pd_xO_{3-\delta}$, for CO oxidation. *J. Catal.*, 249:349–358, 2007.

[10] M. C. J. Bradford and M. A. Vannice. CO_2 reforming of CH_4. *Catal. Rev.*, 41:1–42, 1999.

[11] A. P. E. York, T.-C. Xiao, M. L. H. Green, and J. B. Claridge. Methane oxyforming for synthesis gas production. *Catal. Rev.*, 49:511–560, 2007.

[12] Y.-F. Y. Yao. The oxidation of CO and hydrocarbons over noble metal catalysts. *J. Catal.*, 87:152–162, 1984.

[13] J. Wei and E. Iglesia. Mechanism and site requirements for activation and chemical conversion of methane on supported Pt clusters and turnover rate comparisons among noble metals. *J. Phys. Chem. B*, 108:4094–4103, 2004.

[14] B. L. Mojet, J. T. Miller, D. E. Ramaker, and D. C. Koningsberger. A new model describing the metal–support interaction in noble metal catalysts. *J. Catal.*, 186:373–386, 1999.

[15] J. Kašpar, P. Fornasiero, and M. Graziani. Use of CeO_2-based oxides in the three-way catalysis. *Catal. Today*, 50:285–298, 1999.

[16] S. Schauermann, N. Nilius, S. Shaikhutdinov, and H.-J. Freund. Nanoparticles for heterogeneous catalysis: New mechanistic insights. *Acc. Chem. Res.*, 46:1673–1681, 2013.

[17] E. W. McFarland and H. Metiu. Catalysis by doped oxides. *Chem. Rev.*, 113:4391–4427, 2013.

[18] M. S. Hegde, G. Madras, and K. C. Patil. Noble metal ionic catalysts. *Acc. Chem. Res.*, 42:704–712, 2009.

[19] A. Gupta, A. Kumar, U. V. Waghmare, and M. S. Hegde. Origin of activation of lattice oxygen and synergistic interaction in bimetal-ionic $Ce_{0.89}Fe_{0.1}Pd_{0.01}O_{2-\delta}$ Catalyst. *Chem. Mater.*, 21:4880–4891, 2009.

[20] A. Gupta, U. V. Waghmare, and M. S. Hegde. Correlation of oxygen storage capacity and structural distortion in transition-metal-, noble-metal-, and rare-earth-ion-substituted CeO_2 from first principles calculation. *Chem. Mater.*, 22:5184–5198, 2010.

[21] T. Baidya, G. Dutta, M. S. Hegde, and U. V. Waghmare. Noble metal ionic catalysts: correlation of increase in CO oxidation activity with increasing effective charge on Pd ion in Pd ion substituted $Ce_{1-x}M_xO_{2-\delta}$ (M = Ti, Zr and Hf). *Dalton Trans.*, (3):455, 2008.

[22] J. A. Kurzman, L. M. Misch, and R. Seshadri. Chemistry of precious metal oxides relevant to heterogeneous catalysis. *Dalton Trans.*, 42:14653–14667, 2013.

[23] S. E. Skrabalak and K. S. Suslick. Porous carbon powders prepared by ultrasonic spray pyrolysis. *J. Am. Chem. Soc.*, 128:12642–12643, 2006.

[24] M. W. Gaultois, P. T. Barton, C. S. Birkel, L. M. Misch, E. E. Rodriguez, G. D. Stucky, and R. Seshadri. Structural disorder, magnetism, and electrical and thermoelectric properties of pyrochlore $Nd_2Ru_2O_7$. *J. Phys.: Condens. Matter*, 25:186004, 2013.

[25] A. Birkel, L. E. Darago, A. Morrison, L. Lory, N. C. George, A. A. Mikhailovsky, C. S. Birkel, and R. Seshadri. Microwave assisted preparation of Eu^{2+}-doped Åkermanite $Ca_2MgSi_2O_7$. *Solid State Sci.*, 14(6):739–745, 2012.

[26] A. Birkel, Y.-G. Lee, D. Koll, X. Van Meerbeek, S. Frank, M. J. Choi, Y. S. Kang, K. Char, and W. Tremel. Highly efficient and stable dye-sensitized solar cells based on SnO_2 nanocrystals prepared by microwave-assisted synthesis. *Energy Environ. Sci.*, 5:5392–5400, 2012.

[27] A. Birkel, K. A. Denault, N. C. George, C. E. Doll, B. Héry, A. A. Mikhailovsky, C. S. Birkel, B.-C. Hong, and R. Seshadri. Rapid microwave preparation of highly efficient Ce^{3+}–substituted garnet phosphors for solid state white lighting. *Chem. Mater.*, 24:1198–1204, 2012.

[28] C. S. Birkel, W. G. Zeier, J. E. Douglas, B. R. Lettiere, C. E. Mills, G. Seward, A. Birkel, M. L. Snedaker, Y. Zhang, G. J. Snyder, T. M. Pollock, R. Seshadri, and G. D. Stucky. Rapid microwave preparation of thermoelectric tinisn and ticosb half-heusler compounds. *Chem. Mater.*, 24:2558–2565, 2012.

[29] L. M. Misch, J. A. Kurzman, A. R. Derk, Y.-I. Kim, R. Seshadri, H. Metiu, E. W. McFarland, and G. D. Stucky. C–H bond activation by Pd-substituted CeO_2: Substituted ions *versus* reduced species. *Chem. Mater.*, 23:5432–5439, 2011.

[30] R. H. Crabtree. Aspects of methane chemistry. *Chem. Rev.*, 95:987–1007, 1995.

[31] J. M. Thomas. Heterogeneous catalysis: Enigmas, illusions, challenges, realities, and emergent strategies of design. *J. Chem. Phys.*, 128:182502, 2008.

[32] P. Bera, K. C. Patil, V. Jayaram, G. N. Subbanna, and M. S. Hegde. Ionic dispersion of Pt and Pd on CeO_2 by combustion method: Effect of metal–ceria interaction on catalytic activities for NO reduction and CO and hydrocarbon oxidation. *J. Catal.*, 196:293–301, 2000.

[33] T. Baidya, A. Marimuthu, M. S. Hegde, N. Ravishankar, and G. Madras. Higher catalytic activity of nano-$Ce_{1-x-y}Ti_xPt_yO_{2-\delta}$ compared to nano-$Ce_{1-x}Pd_xO_{2-\delta}$ for CO oxidation and N_2O and NO reduction by CO: Role of oxide ion vacancy. *J.Phys. Chem. C*, 111:830–839, 2007.

[34] A. K. Datye, J. Bravo, T. R. Nelson, P. Atanasova, M. Lyubovsky, and L. Pfefferle. Catalyst microstructure and methane oxidation reactivity during the Pd–PdO transformation on alumina supports. *Appl. Catal. A-Gen.*, 198:179–196, 2000.

[35] J. Li, U. G. Singh, J. W. Bennett, K. Page, J. C. Weaver, J.-P. Zhang, T. Proffen, A. M. Rappe, S. Scott, and R. Seshadri. $BaCe_{1-x}Pd_xO_{3-\delta}$ ($0 \leq x \leq 0.1$): Redox controlled ingress and egress of palladium in a perovskite. *Chem. Mater.*, 19:1418–1426, 2007.

[36] F. H. Ribeiro and M. Chow. Kinetics of the complete oxidation of methane over supported palladium catalysts. *J. Catal.*, 146:537–544, 1994.

[37] L. S. Escandon, S. Ordonez, and A. Vega. Oxidation of methane over palladium catalysts: effect of the support. *Chemosphere*, 58:9–17, 2005.

[38] R. F. Hicks, H. Qi, and M. L. Young. Structure sensitivity of methane oxidation over platinum and palladium. *J. Catal.*, 122:280–294, 1990.

[39] A. Basile and L. Paturzo. The partial oxidation of methane to syngas in a palladium membrane reactor: Simulation and experimental studies. *Catal. Today*, 67:65–75, 2001.

[40] C. F. Cullis, T. G. Nevell, and D. L. Trimm. Role of the catalyst support in the oxidation of methane over palladium. *J. Chem. Soc. Farad. T. 1*, 68:1406, 1972.

[41] C. A. Muller, M. Maciejewski, and R. A. Koeppel. Combustion of methane over palladium/zirconia derived from a glassy Pd-Zr alloy: Effect of Pd particle size on catalytic behavior. *J. Catal.*, 166:36–43, 1997.

[42] C. A. Muller, M. Maciejewski, R. A. Koeppel, and A. Baiker. Combustion of methane over palladium/zirconia: effect of Pd-particle size and role of lattice oxygen. *Catal. Today*, 47:245–252, 1999.

[43] D. Ciuparu, E. Altman, and L. Pfefferle. Contributions of lattice oxygen in methane combustion over PdO-based catalysts. *J. Catal.*, 203:64–74, 2001.

[44] G. Groppi, C. Cristiani, L. Lietti, C. Ramella, M. Valentini, and P. Forzatti. Effect of ceria on palladium supported catalysts for high temperature combustion of CH_4 under lean conditions. *Catal. Today*, 50:399–412, 1999.

[45] J. N. Carstens and S. C. Su. Factors affecting the catalytic activity of Pd/ZrO_2 for the combustion of methane. *J. Catal.*, 176:136–142, 1998.

[46] J.-D. Grunwaldt, M. Maciejewski, and A. Baiker. In situ X-ray absorption study during methane combustion over Pd/ZrO_2 catalysts. *Phys. Chem. Chem. Phys.*, 5:1481–1488, 2003.

[47] R. Strobel, S. E. Pratsinis, and A. Baiker. Flame-made Pd/La_2O_3/Al_2O_3 nanoparticles: Thermal stability and catalytic behavior in methane combustion. *J. Mater. Chem.*, 15:605, 2005.

[48] K. Persson, A. Ersson, K. Jansson, N. Iverlund, and S. Jaras. Influence of co-metals on bimetallic palladium catalysts for methane combustion. *J. Catal.*, 231:139–150, 2005.

[49] S. Roy, M. S. Hedge, N. Ravishankar, and G. Madras. Creation of redox adsorption sites by Pd^{2+} ion substitution in nano TiO_2 for high photocatalytic activity of CO oxidation, NO reduction, and NO decomposition. *J. Phys. Chem. C*, 111:8153–8160, 2007.

[50] S. Roy, A. Marimuthu, M. S. Hegde, and G. Madras. High rates of NO and N_2O reduction by CO, CO and hydrocarbon oxidation by O_2 over nano crystalline $Ce_{0.98}Pd_{0.02}O_{2-\delta}$: Catalytic and kinetic studies. *Appl. Catal. B-Environ.*, 71:23–31, 2007.

[51] T. Baidya, A. Gupta, P. A. Deshpandey, G. Madras, and M. S. Hegde. High oxygen storage capacity and high rates of CO oxidation and NO reduction catalytic properties of $Ce_{1-x}SnO_2$ and $Ce_{0.78}Sn_{0.2}Pd_{0.02}O_{2-\delta}$. *J. Phys. Chem. C*, 113:4059–4068, 2009.

[52] S. Roy, M. S. Hegde, and G. Madras. Catalysis for NOx abatement. *Appl. Energ.*, 86:2283–2297, 2009.

[53] P. Singh and M. S. Hegde. Controlled synthesis of nanocrystalline CeO_2 and $Ce_{1-x}M_xO_2 - \delta$ (M = Zr, Y, Ti, Pr and Fe) solid solutions by the hydrothermal method: Structure and oxygen storage capacity. *J. Solid State Chem.*, 181:3248–3256, 2008.

[54] T. Baidya, K. R. Priolkar, P. R. Sarode, M. S. Hegde, K. Asakura, G. Tateno, and Y. Koike. Local structure of Pt and Pd ions in $Ce_{1-x}Ti_xO_2$: X-ray diffraction, x-ray photoelectron spectroscopy, and extended x-ray absorption fine structure. *J. Chem. Phys.*, 128:124711, 2008.

[55] D. O. Scanlon, B. J. Morgan, and G. W. Watson. The origin of the enhanced oxygen storage capacity of $Ce_{1-x}(Pd/Pt)_xO_2$. *Phys. Chem. Chem. Phys.*, 13:4279, 2011.

[56] M. Haneda, T. Mizushima, and N. Kakuta. Synergistic effect between Pd and nonstoichiometric cerium oxide for oxygen activation in methane oxidation. *J. Phys. Chem. B*, 102:6579–6587, 1998.

[57] D. Ciuparu, F. Bozon-Verduraz, and L. Pfefferle. Oxygen exchange between palladium and oxide supports in combustion catalysts. *J. Phys. Chem. B*, 106:3434–3442, 2002.

[58] R. Gorte and S. Zhao. Studies of the water-gas-shift reaction with ceria-supported precious metals. *Catal. Today*, 104:18–24, 2005.

[59] S. Sharma, P. A. Deshpande, M. S. Hegde, and G. Madras. Nondeactivating nanosized ionic catalysts for water-gas shift reaction. *Ind. Eng. Chem. Res.*, 48:6535–6543, 2009.

[60] Q. Fu. Active nonmetallic Au and Pt species on ceria-based water-gas shift catalysts. *Science*, 301:935–938, 2003.

[61] L. C. Kao, A. C. Hutson, and A. Sen. Low-temperature, palladium(II)-catalyzed, solution-phase oxidation of methane to a methanol derivative. *J. Am. Chem. Soc.*, 113:700–701, 1991.

[62] J. H. Lunsford. Catalytic conversion of methane to more useful chemicals and fuels: A challenge for the 21st century. *Catal. Today*, (63):165–174, 2000.

[63] W. Tang, Z. Hu, M. Wang, G. D. Stucky, H. Metiu, and E. W. McFarland. Methane complete and partial oxidation catalyzed by Pt-doped CeO_2. *J. Catal.*, 273:125–137, 2010.

[64] J. F. Bérar and G. Baldinozzi. Procedures for the refinement of incommensurate structures using XND. Coding issues for the refinement of incommensurate structures., 2005.

[65] B. Palosz, E. Grzanka, S. Gierlotka, S. Stel'makh, R. Pielaszek, U. Bismayer, J. Neuefeind, H. P. Weber, T. Proffen, R. Von Dreele, and W. Palosz. Analysis of short and long range atomic order in nanocrystalline diamonds with application of powder diffractometry. *Z. Kristallogr.*, 217:497–509, 2002.

[66] B. Palosz, E. Grzanka, S. Gierlotka, S. Stel'makh, R. Pielaszek, W. Lojkowski, U. Bismayer, J. Neuefeind, H. P. Weber, and W. Palosz. Application of X-ray powder diffraction to nano-materials - determination of the atomic structure of nanocrystals with relaxed and strained surfaces. *Phase Transit.*, 76:171–185, 2003.

[67] B. Palosz, E. Grzanka, S. Gierlotka, and S. Stel'makh. Nanocrystals: Breaking limitations of data analysis. *Z. Kristallogr.*, 225:588–598, 2010.

[68] G. K. Williamson and W. H. Hall. X-ray line broadening from filed aluminium and wolfram. *Acta Metall.*, 1:22–31, 1953.

[69] K. R. Priolkar, P. Bera, P. R. Sarode, M. S. Hegde, S. Emura, R. Kumashiro, and N. P. Lalla. Formation of $Ce_{1-x}Pd_xO_{2-\delta}$ solid solution in combustion-synthesized Pd/CeO_2 catalyst: XRD, XPS, and EXAFS investigation. *Chem. Mater.*, 14:2120–2128, 2002.

[70] M. Brun, A. Berthet, and J. C. Bertolini. XPS, AES and Auger parameter of Pd and PdO. *J. Electron. Spectrosc. Relat. Phenom.*, 104(1-3):55–60, 1999.

[71] P. Singh and M. S. Hegde. Sonochemical synthesis of thermally stable hierarchical $Ce_{1-x}M_xO_{2-\delta}$ (M = Pt or Pd, $0 \leq x \leq 0.10$) nanocrystallites: Redox properties and methanol electro-oxidation activity. *Cryst. Growth Des.*, 10:2995–3004, 2010.

[72] W. T. McGown, C. Kemball, D. A. Whan, and M. S. Scurrell. Hydrogenation of acetylene in excess ethylene on an alumina supported palladium catalyst in a static system. *J. Chem. Soc. Farad. T. 1*, 73:632–647, 1977.

[73] L. M. Misch, A. Birkel, C. A. Figg, B. P. Fors, C. J. Hawker, G. D. Stucky, and R. Seshadri. Rapid microwave-assisted sol-gel preparation of Pd-substituted $LnFeO_3$ (Ln = Y, La): Phase formation and catalytic activity. *Dalton Trans.*, 43:2079–2087, 2014.

[74] J. A. Kurzman, X. Ouyang, W. B. Im, J. Li, J. Hu, S. L. Scott, and R. Seshadri. La_4LiAuO_8 and La_2BaPdO_5: Comparing two highly stable d^8 square-planar oxides. *Inorg. Chem.*, 49:4670–4680, 2010.

[75] J. A. Kurzman, J. Li, T. D. Schladt, C. R. Parra, X. Ouyang, R. Davis, J. T. Miller, S. L. Scott, and R. Seshadri. Pd^{2+}/Pd^0 Redox cycling in hexagonal $YMn_{0.5}Fe_{0.5}O_3$: Implications for catalysis by PGM-substituted complex oxides. *Inorg. Chem.*, 50:8073–8084, 2011.

[76] W. F. Libby, S. Url, and S. Levine. Promising catalyst for auto exhaust. *Science*, 171:499–500, 1971.

[77] D. B. Meadowcroft. Low-cost oxygen electrode material. *Nature*, 226:847–848, 1970.

[78] S. P. Andrews, A. F. Stepan, H. Tanaka, S. V. Ley, and M. D. Smith. Heterogeneous or homogeneous? A case study involving palladium-containing perovskites in the Suzuki reaction. *Adv. Synth. Catal.*, 347:647–654, 2005.

[79] E. Negishi, Q. Hu, Z. Huang, and M. Qian. Palladium-catalyzed alkenylation by the Negishi coupling. *Aldrichim. Acta*, 38:1–48, 2005.

[80] M. Kosugi and K. Fugami. A historical note of the Stille reaction. *J. Organomet. Chem.*, 653:50–53, 2002.

[81] R. Chinchilla and C. Nájera. Recent advances in Sonogashira reactions. *Chem. Soc. Rev.*, 40(10):5084–5121, 2011.

[82] D. S. Surry and S. L. Buchwald. Diamine ligands in copper–catalyzed reactions. *Chem. Sci.*, 1:13–31, 2010.

[83] I. P. Beletskaya and A. V. Cheprakov. The Heck reaction as a sharpening stone of palladium catalysis. *Chem. Rev.*, 100(8):3009–3066, 2000.

[84] T. Hiyama and E. Shirakawa. *Top. Curr. Chem.*, 219:61–85, 2002.

[85] I. Hamada, A. Uozumi, Y. Morikawa, A. Yanase, and H. Katayama-Yoshida. A density functional theory study of self-regenerating catalysts $LaFe_{1-x}M_xO_{3-y}$ (M = Pd, Rh, Pt). *J. Am. Chem. Soc.*, 133:18506–18509, 2011.

[86] S. Yanagisawa, A. Uozumi, I. Hamada, and Y. Morikawa. Search for a self-regenerating perovskite catalyst using *ab initio* thermodynamics calculations. *J. Phys. Chem. C*, 117:1278–1286, 2013.

[87] M. D Smith, A. F. Stepan, C. Ramarao, P. E. Brennan, and S. V. Ley. Palladium-containing perovskites: Recoverable and reuseable catalysts for Suzuki couplings. *Chem. Comm.*, (21):2652, 2003.

[88] R. Roy, S. Komarneni, and L. J. Yang. Controlled microwave heating and melting of gels. *J. Am. Ceram. Soc.*, 68:392–395, 1985.

[89] J. D. Katz. Microwave Sintering of Ceramics. *Annu. Rev. Mater. Sci.*, 22:153–170, 1992.

[90] D.R. Baghurst, A.M. Chippindale, and D. Michael P. Mingos. Microwave syntheses for superconducting ceramics. *Nature*, 332:311, 1988.

[91] K. Biswas, S. Muir, and M.a. Subramanian. Rapid microwave synthesis of indium filled skutterudites: An energy efficient route to high performance thermoelectric materials. *Mater. Res. Bull.*, 46:2288–2290, 2011.

[92] N. C. George, A. Birkel, J. Brgoch, B.-C. Hong, A. A. Mikhailovsky, K. Page, A. Llobet, and R. Seshadri. Average and local structural origins of the optical properties of the nitride phosphor $La_{3-x}Ce_xSi_6N_{11}$. *Inorg. Chem.*, 52, 2013.

[93] Z. Y. Zhong, K. D. Chen, Y. Ji, and Q. J. Yan. Methane combustion over B-site partially substituted perovskite-type $LaFeO_3$ prepared by sol-gel method. *Appl. Catal. A-Gen.*, 156:29–41, 1997.

[94] P. Ciambelli, S. Cimino, L. Lisi, M. Faticanti, G. Minelli, I. Pettiti, and P. Porta. La, Ca and Fe oxide perovskites: preparation, characterization and catalytic properties for methane combustion. *Appl. Catal., B*, 33:193–203, 2001.

[95] X. Qi, J. Zhou, Z. Yue, Z. Gui, and L. Li. Auto-combustion synthesis of nanocrystalline $LaFeO_3$. *Mater. Chem. Phys.*, 78:25–29, 2002.

[96] X. Zhang, Y. Li, H. Li, and W. Shen. Preparation of $LaFe_{0.95}Pd_{0.05}O_3$ perovskites and their catalytic performances in methane combustion. *J. Nat. Gas Chem.*, 21:113–118, 2012.

[97] J. Zhang and H. Li. *Perovskite*. Crystallography, chemistry and catalytic performance. Nova Science Pub Incorporated, 2013.

[98] P. D. Ramesh, D. Brandon, and L. Schächter. Use of partially oxidized SiC particle bed for microwave sintering of low loss ceramics. *Mater. Sci. Eng., A*, 266:211–220, 1999.

[99] H. M. Rietveld. A profile refinement method for nuclear and magnetic structures. *J. Appl. Cryst.*, 2:65–71, 1969.

[100] A. A. Coelho. Topas Academic V4.1. Software, Coelho Software, Brisbane (Australia), 2007.

[101] T. E. Barder, S. D. Walker, J. R. Martinelli, and S. L. Buchwald. Catalysts for SuzukiMiyaura coupling processes: Scope and studies of the effect of ligand structure. *J. Am. Chem. Soc.*, 127:4685–4696, 2005.

[102] L. M. Misch, J. Brgoch, A. Birkel, T. E. Mates, G. D. Stucky, and R. Seshadri. Rapid microwave preparation and *ab initio* studies of the stability of the complex noble metal oxides La_2BaPdO_5 and La_2BaPtO_5. *Inorg. Chem.*, 53:2628–2634, 2014.

[103] J. A. Kurzman, M.-S. Miao, and R. Seshadri. Hybrid functional electronic structure of $pbpdo_2$, a small-gap semiconductor. *J. Phys.: Condens. Matter*, 23:465501, 2011.

[104] N. N. Greenwood and A. Earnshaw. *Chemistry of the Elements, 2nd ed.* Butterworth–Heinemann, 1997.

[105] M. Peuckert. XPS Study on Surface and Bulk Palladium Oxide, Its Thermal-Stability, and a Comparison with Other Noble-Metal Oxides. *J. Phys. Chem.*, 89:2481–2486, 1985.

[106] S. J. III Mugavero, W. R. Gemmill, I. P. Roof, and H. C. Zur Loye. Materials discovery by crystal growth: Lanthanide metal containing oxides of the

platinum group metals (Ru, Os, Ir, Rh, Pd, Pt) from molten alkali metal hydroxides. *J. Solid State Chem.*, 182:1950–1963, 2009.

[107] D. E. Bugaris and H. C. Zur Loye. Materials Discovery by Flux Crystal Growth: Quaternary and Higher Order Oxides. *Angew. Chem. Int. Ed.*, 51:3780–3811, 2012.

[108] Y. Laligant, A. Le Bail, and G. Férey. Complex palladium oxides. V. Crystal structure of $LiBiPd_2O_4$: An example of three different fourfold coordinations of cations. *J. Solid State Chem.*, 81:58–64, 1989.

[109] H.-K. Müller-Buschbaum and D Schlüter. Zur Kenntnis von $BaPtLa_2O_5$ und $BaNiY_2O_5$. *J. Less. Common Met.*, 166:L7–L0, 1990.

[110] C. G. van de Walle and R. M. Martin. Theoretical Calculations of Heterojunction Discontinuities in the Si/Ge System. *Phys. Rev. B*, 34:5621–5634, 1986.

[111] A. Le Bail, H. Duroy, and J. L. Fourquet. *Ab initio* structure determination of $LiSbW0_8$ by X-Ray powder diffraction. *Mater. Res. Bull.*, 23:447–452, 1988.

[112] G. Kresse and J. Furthmuller. *Ab initio* molecular dynamics For liquid-metals. *Phys. Rev. B*, 47:558–561, 1993.

[113] G. Kresse and J. Furthmuller. Efficient iterative schemes for *ab initio* total-energy calculations using a plane-wave basis set. *Phys. Rev. B*, 54:11169–11186, 1996.

[114] P.E. Blöchl. Projector augmented-wave method. *Phys. Rev. B*, 50:17953–17979, 1994.

[115] G. Kresse and D. Joubert. From ultrasoft pseudopotentials to the projector augmented-wave method. *Phys. Rev. B*, 59:1758–1775, 1999.

[116] J. P. Perdew, K. Burke, and M. Ernzerhof. Generalized gradient approximation made simple. *Phys. Rev. Lett.*, 77:3865–3868, 1996.

[117] H. J. Monkhorst and J. D. Pack. Monkhorst-Pack k-point method. *Phys. Rev. B*, 13:5188–5192, 1976.

[118] J. Uddin, J. E. Peralta, and G. E. Scuseria. Density functional theory study of bulk platinum monoxide. *Phys. Rev. B*, 71:155112, 2005.

[119] J. P. Attfield and G. Férey. Structural correlations within the lanthanum palladium oxide family. *J.Solid State Chem.*, 80:286–298, 1989.

[120] J. P. Attfield. *Ab initio* structure determinations of two lanthanum palladium oxides by modelling and powder diffraction methods. *Acta. Cryst. B44, 563-568*, pages 1–6, 1988.

[121] S. Seong, K. A. Yee, and T. A. Albright. Interlayer communication in some two-dimensional materials. *J. Am. Chem. Soc.*, 115:1981–1987, 1993.

[122] M. Andersson, K. Jansson, and M. Nygren. Catalytic behaviour of La_4PdO_7 based catalysts when exposed to car exhaust conditions. *Catal. Letters*, 39:253–259, 1996.